

INVESTIGATION OF BULK INDIUM ANTIMONIDE AS A HETERODYNE  
DETECTOR FOR THE SUBMILLIMETER WAVELENGTH REGION

Thesis by  
Elliott R. Brown

In Partial Fulfillment of the Requirements  
for the Degree of  
Doctor of Philosophy

California Institute of Technology  
Pasadena, California

1985  
(Submitted May 6, 1985)

to Elayne

### ACKNOWLEDGEMENTS

I wish to thank my adviser, Tom Phillips, for supporting my graduate studies at Caltech for five long years. I have no end of respect for his accomplishments and his approach to research. My only regret is that I got so little of his time. I am greatly indebted to Dan Watson, who provided endless encouragement and technical advice for my last two years at Caltech. Down the home stretch of my studies, he designed and taught me how to use a far-infrared molecular laser that enabled the 812 GHz heterodyne measurements. Besides all of Dan's technical abilities, he is certainly one of the most amiable and cooperative scientists I have ever met. I would also like to thank my office mate for five years, Mike Wengler. Mike was my computer guru and made a key contribution to my thesis work by writing the software necessary for the FTS. I also wish to express gratitude to Colin Masson for his advice on electronic problems. He steered me clear of potential pitfalls in the development of the FTS and provided several stimulating conversations during the development of the ultra-low noise preamp for the Putley detector. I also want to thank Dave Woody. Dave was my laboratory guru during my first two years of graduate research. He also introduced me to bolometer theory and to Mather's theory of non-equilibrium noise. I want to thank Jocelyn Keene for the use of her wonderful capacitive mesh filters in several of my experiments. She was also instrumental in the successful demonstration of the Putley mode mixer. A word of appreciation is due to Erich Grossman who was always willing to lend a helping hand. I express gratitude to Paige Hooper for endless moral support, Bruce Veidt for warm friendship, Glen Abrahams for technical assistance, and Pat Neill for her management efforts. Also, it was my privilege to have the expert advice of Peter Bratt of SBRC at the beginning of my studies and Keith Matthews of the Caltech Infrared Group at the end.

**ABSTRACT**

Bulk n-InSb is investigated as a heterodyne detector for the submillimeter wavelength region. Two modes of operation are investigated: (1) the Rollin or hot electron bolometer mode (zero magnetic field), and (2) the Putley mode (quantizing magnetic field). The highlight of the thesis work is the pioneering demonstration of the Putley mode mixer at several frequencies. For example, a double-sideband system noise temperature of about 510K was obtained using a 812 GHz methanol laser for the local oscillator. This performance is at least a factor of 10 more sensitive than any other performance reported to date at the same frequency. In addition, the Putley mode mixer achieved system noise temperatures of 250K at 492 GHz and 350K at 625 GHz. The 492 GHz performance is about 50% better and the 625 GHz is about 100% better than previous best performances established by the Rollin-mode mixer. To achieve these results, it was necessary to design a totally new ultra-low noise, room-temperature preamp to handle the higher source impedance imposed by the Putley mode operation. This preamp has considerably less input capacitance than comparably noisy, ambient designs.

In addition to advancing receiver technology, this thesis also presents several novel results regarding the physics of n-InSb at low temperatures. A Fourier transform spectrometer was constructed and used to measure the submillimeter wave absorption coefficient of relatively pure material at liquid helium temperatures and in zero magnetic field. Below 4.2K, the absorption coefficient was found to decrease with frequency much faster than predicted by Drudian theory. Much better agreement with experiment was obtained using a quantum theory based on inverse-Bremmstrahlung in a solid. Also the noise of the Rollin-mode detector at 4.2K was accurately measured and compared with theory. The power spectrum is found to be well fit by a recent theory of non-

equilibrium noise due to Mather. Surprisingly, when biased for optimum detector performance, high-purity InSb cooled to liquid helium temperatures generates less noise than that predicted by simple non-equilibrium Johnson noise theory alone. This explains in part the excellent performance of the Rollin-mode detector in the millimeter wavelength region.

Again using the Fourier transform spectrometer, spectra are obtained of the responsivity and direct detection NEP as a function of magnetic field in the range 20-110  $\text{cm}^{-1}$ . The results show a discernable peak in the detector response at the conduction electron cyclotron resonance frequency for magnetic fields as low as 3 KG at bath temperatures of 2.0K. The spectra also display the well-known peak due to the cyclotron resonance of electrons bound to impurity states. The magnitude of responsivity at both peaks is roughly constant with magnetic field and is comparable to the low frequency Rollin-mode response. The NEP at the peaks is found to be much better than previous values at the same frequency and comparable to the best long wavelength results previously reported. For example, a value  $\text{NEP}=4.5 \times 10^{-15} \text{W/Hz}^{1/2}$  is measured at 4.2K, 6 KG and 40  $\text{cm}^{-1}$ . Study of the responsivity under conditions of impact ionization showed a dramatic disappearance of the impurity electron resonance while the conduction electron resonance remained constant. This observation offers the first concrete evidence that the mobility of an electron in the  $N=0$  and  $N=1$  Landau levels is different. Finally, these direct detection experiments indicate that the excellent heterodyne performance achieved at 812 GHz should be attainable up to frequencies of at least 1200 GHz.

**Parts of this thesis have been or will be published under the following titles:**

"Nonequilibrium Noise of InSb Hot Electron Bolometers," Elliott R. Brown, *J. Appl. Phys.*, **55**, 213 (1984).

"Submillimeter Wave Absorption of n-InSb at Low Temperatures," Elliott R. Brown, *J. Appl. Phys.*, **57**, 2361 (1985).

"Absolute Response and Noise Equivalent Power of Cyclotron Resonance Assisted InSb Detectors at Submillimeter Wavelengths," Elliott R. Brown, M.J. Wengler and T.G. Phillips, in press, *Journal of Applied Physics*.

"Ultra-low Noise, High-Impedance Preamp for Cryogenic Detectors," Elliott R. Brown, *Electronics Letters*, in press.

"Submillimeter Heterodyne Receiver based on the Cyclotron Resonance Enhanced InSb Detector," Elliott R. Brown, Jocelyn Keene, T.G. Phillips and D.M. Watson, in preparation.

"On the Photoconductive Mechanism of the InSb Cyclotron Resonance Detector," Elliott R. Brown, in preparation.

## Table of Contents

Section	Subject	Page
Acknowledgements		iii
Abstract		iv
<b>Chapter 1</b>	<b>Introduction</b>	<b>1</b>
1.0	Thesis Motivation and Organization	1
1.1	Historical Perspective	3
1.1.1	Rollin Mode	3
1.1.2	Putley Mode	5
1.2	Small Signal Detection Parameters	6
1.3	Heterodyne Detection with Square-Law Detectors	8
1.4	The State of the Art in Submillimeter Heterodyning	13
<b>Chapter 2</b>	<b>InSb Material Studies</b>	<b>16</b>
2.0	Introduction	16
2.1	Material Handling and Preparation	16
2.2	InSb Band Structure	17
2.3	Impurity Studies	19
2.4	DC Conductivity	23
2.4.1	DC Conductivity Theory	24
2.4.2	DC Conductivity Experiment	25
2.4.3	DC Conductivity Discussion	30
2.5	Static Thermal Conductance	33
2.6	I-V Curves: Demonstration of Bolometer Theory	37
2.7	Absorption Coefficient in the Submillimeter Region	43

2.7.1	Theory of Absorption and Transmission Coefficients	43
2.7.2	Absorption Experiment	46
2.7.3	Absorption Results	49
2.7.4	Discussion	52
<b>Chapter 3</b>	<b>Rollin Mode Detection</b>	<b>57</b>
3.0	Introduction	57
3.1	Experimental Absolute Response	58
3.2	Noise of the Hot Electron Bolometer	62
3.2.1	Bolometer Noise Theory	63
3.2.2	Noise Experiment	65
3.3	Rollin Mode Bandwidth	76
3.3.1	Bolometer Response Time	76
3.3.2	Experimental Bandwidth	78
3.4	Heterodyne Performance	79
3.5	Conclusion	82
<b>Chapter 4</b>	<b>Putley Mode Detection</b>	<b>86</b>
4.0	Introduction	86
4.1	Absolute Response of Putley Mode Detectors	88
4.2	Noise and Direct Detection NEP	100
4.2.1	Experimental Noise	100
4.2.2	Direct Detection NEP	101
4.3	Direct Detection Discussion	103
4.4	Cyclotron Resonance Photoresponse Mechanisms	105
4.5	Response Time of Putley Mode Detector	107
4.6	Heterodyne Detection	109
4.6.1	Mixer Mounting Structure	111



4.6.2	Voigt Configuration: Laser Heterodyne Results	111
4.6.3	Faraday Configuration Receiver	118
4.6.4	The Future of the Putley Mode Mixer	120
Appendix A	Impurity Concentrations from Hall Data	122
Appendix B	Dynamic Resistance Measurement Technique	128
Appendix C	Fourier Transform Spectrometer	130
Appendix D	Ultra-low Noise Preamp for the Putley Detector	135
References		140

## 1. Introduction

### 1.0 Thesis Motivation and Organization

The submillimeter wavelength region ( $\lambda \sim 200-1000 \mu\text{m}$ ) remains one of the last technological frontiers of the electromagnetic spectrum. It has long been plagued by a serious shortage of good detectors and radiation sources. During the past decade or so, the demand for high quality detectors has increased greatly with accelerating interests in submillimeter science. In particular, the field of interstellar astronomy has blossomed and entails as one of its most important tasks the characterization of molecular and atomic lines. This demands very high resolution spectroscopy that is practical only with heterodyne receivers. The results presented in this thesis stem from research aimed at developing a submillimeter heterodyne receiver using bulk InSb as the detecting element. Two modes of detection are investigated: the hot electron bolometer or Rollin mode, and the cyclotron resonance or Putley mode.

Liquid helium cooled n-type InSb is one of the best detector materials for the submillimeter part of the spectrum. In zero or weak magnetic fields (Rollin mode), relatively pure n-type material displays pronounced hot electron effects. This fact combined with the electronic submillimeter absorption makes InSb a very sensitive bolometer. It has been used both as a direct detector for molecular spectroscopy [Fleming 1979] and plasma diagnostics [Luhmann 1982] and as a heterodyne detector for submillimeter astronomy [Phillips and Woody 1982]. The direct detectors are routinely used up to frequencies of 1 THz while the heterodyne application has recently been extended above 600 GHz with the identification of the  $J=1 \rightarrow 0$  HCl line in the Orion molecular cloud [Blake et al. 1985]. Part of this thesis is concerned with extending the Rollin mode heterodyne performance to even higher frequencies.

When I started this project, it was known that the performance of the existing Rollin mode heterodyne detector was decaying rapidly with frequency in the ~230-500 GHz region. This problem was attributed to the rolloff of the absorption coefficient of InSb in the same frequency range. However, the precise behavior of the absorption coefficient and the correlation between it and the other detector properties were not understood. Therefore, my first task was to understand the hot electron bolometer in terms of material properties. From this understanding, the feasibility of the Rollin mode detector in the >600 GHz range was determined. The conclusions presented in Chapter 3 show that, independent of the InSb materials tested, there is a rapid rolloff of performance with frequency. However, many interesting facts about InSb were learned along the way. For example, the absorption coefficient was found to be distinctly non-Druidian, the DC conductivity was found to have a temperature dependence which was not explicable by simple metallic or semiconductor theories, and the noise was found to be less than predicted by equilibrium Johnson noise theory alone. These results, and others, are discussed in Chapters 2 and 3.

About midway through my graduate studies, I began studying the performance of the InSb detector in a quantizing magnetic field (Putley mode). Direct detection experiments were performed to measure the absolute responsivity and NEP as a function of detector geometry, material and temperature. These results are given in Chapter 4. Based on the results of these experiments, a Putley mode heterodyne receiver was designed. This receiver incorporates a permanent magnet to generate a field of the correct magnitude for cyclotron resonance at the submillimeter wavelength of interest. The InSb mixer is mounted in overmoded waveguide and radiation is coupled in with a feedhorn. The design is described in Chapter 4, along with experimental heterodyne results and interpretations. This is thought to be the pioneering study of

heterodyne detection with cyclotron resonance assisted detectors.

## **1.1 Historical Perspective: Bulk InSb as a Submillimeter Detector**

### **1.1.1 Rollin Mode**

In the late 1950's it was thought that the purest available InSb would display extrinsic photoconductivity. During the search for this effect, photoresponse was observed that did not have a long wavelength cutoff as all simple photoconductors do [Putley 1960]. Rollin was the first person to show that the observed photoresponse could be associated with free carrier absorption alone [Rollin 1961]. He also correctly stated that the relatively large magnitude of the effect compared to that in other semiconductors was due to the very small InSb electron-phonon interaction. Shortly thereafter, Kogan [1963] demonstrated that the effect could be explained with bolometric analysis.

Following the initial pioneering work, there were several developmental efforts to build receivers based on the hot electron bolometer. The most notable was that of Kinch and Rollin [1963]. Using a helium cooled step-up transformer between the detector and preamp, they achieved a direct NEP of  $\sim 3 \times 10^{-13} \text{ W/Hz}^{1/2}$  in the millimeter wavelength region. This was better than most other far infrared detectors at the time. The responsivity was found to be less than that of other liquid helium cooled, far-infrared bolometers [e.g., Low 1961]. However, the noise was also found to be relatively low, thereby explaining the good NEP. The real advantage of the InSb detector was the relatively short time constant,  $\tau \sim 2 \times 10^{-7}$  sec. This enabled operation at frequencies well above the  $1/f$  noise region.

The possibility of heterodyne detection with the InSb hot electron bolometer was mentioned very early by Rollin [1961] and others. However, the first

demonstration did not come until 1965 with the 8 mm wavelength mixing experiment of Arams et al. [1966]. Although they worked out the first theoretical analysis and found agreement with experiment, the detector performance was rather poor. The heterodyne application was later extended to the 4 mm region by Kinch [1968] and by Whalen and Westgate [1970]. They both obtained much better results than Arams and showed that the performance correlated with the DC I-V characteristics of the mixer as expected from bolometer theory.

The big breakthrough in the the heterodyne application came in 1973 with the now famous 90-140 GHz receiver of Phillips and Jefferts [1973]. They obtained a double-sideband system noise temperature of 250K, a result about a factor of 10 better than any other in the same frequency range at that time. Although it was not obvious from the original paper, the reason for the excellent performance was the optimization of the detector geometry. The bolometer was a very thin post mounted across a waveguide. In this configuration, both the bolometer responsivity and the radiation coupling efficiency were excellent. In addition, the bolometer impedance was high enough that its intrinsic Johnson noise could dominate the noise of a carefully designed FET preamplifier. Consequently, there was no need for the cooled transformer of Kinch and Rollin and the full 1 MHz bandwidth was utilized. This same mixer configuration was later applied in a receiver operating up to about 500 GHz. This receiver made numerous pioneering observations of interstellar lines, including those of CO at 345 GHz, neutral atomic carbon at 492 GHz, and NH<sub>3</sub> at 576 GHz. Most recently, the performance was extended to 626 GHz with the identification of the J=1→0 line of HCl. Despite these great advances, the performance of the receiver decays with increasing frequency. Furthermore, the ~1 MHz bandwidth continues to be a great weakness. As will be shown in Chapter 4, these shortcomings are alleviated by operating the InSb in the Putley mode.

### 1.1.2 Putley Mode

The photo-response of InSb in quantizing magnetic fields was first studied by Putley using a grating spectrometer [Putley 1961]. He presented spectra that peaked at wavenumbers somewhat shorter than  $10 \text{ cm}^{-1}$  but showed no sign of cyclotron resonance up to  $50 \text{ cm}^{-1}$  and magnetic fields up to 8 KG. The fact that the magnetic field changed the magnitude but not the essential shape of the response spectra led Putley to conclude that the free electron absorption cross section was larger than the cyclotron resonance value and that the role of the magnetic field was simply to enhance the bolometric responsivity by increasing the detector resistance.

Shortly thereafter, Brown and Kimmitt presented the first positive identification of cyclotron resonant response [1963]. Also using a grating spectrometer, they identified a peak in the response spectra family at about 150 microns. The responsivity and detectivity at the peak were about 60 V/W and  $3 \times 10^{11} \text{ Hz}^{\frac{1}{2}}/\text{W}$ , respectively. In a later publication, they showed for the first time the existence of fine structure in the resonant response spectra for fields above 40 KG [Brown and Kimmitt 1965]. This structure was not evident at 18 KG.

The situation was later clarified with higher resolution studies of the response and absorption processes. For example, using a Fourier transform spectrometer, Kaplan [1967] showed that the cyclotron resonance response at 17 KG and 4.2K consisted of two separate lines, one associated with conduction electron cyclotron resonance (CCR) and the other with the impurity state cyclotron resonance (ICR). These transitions are shown schematically in Fig. 2.1. He also verified the polarization rules for these transitions: both ICR and CCR absorb +1 helicity (counterclockwise) circular polarized photons propagating parallel to  $\mathbf{B}_0$  (Faraday configuration) and they absorb linearly polarized photons ( $\mathbf{E}_0 \perp \mathbf{B}_0$ ) propagating perpendicular to  $\mathbf{B}_0$  (Voigt configuration). He did not

observe the direct photo-ionization of the ground state bound electron to the  $N=0$  Landau level, a transition that was earlier predicted to be very strong [Wallis and Bowlden 1958]. Kaplan later measured the absorption coefficient and found the theory to fit his results qualitatively [Kaplan 1969].

Better absorption measurements were carried out with far-infrared lasers. One notable study was that of Murotani and Nisida [1972] at  $29.7 \text{ cm}^{-1}$  (337 micron HCN line). They proved clearly that the absorption coefficients for both CCR and ICR transitions were very large and dependent on relative population of electrons in the conduction band and donor states. For example, material with a zero field carrier concentration of  $n = 2.5 \times 10^{13}/\text{cc}$  had an absorption coefficient of about  $180 \text{ cm}^{-1}$  at the ICR peak under the conditions of low FIR power and no DC electrical bias. This corresponds to an ICR cross section of  $\approx 7 \times 10^{-12} \text{ cm}^2$ . A later experiment conducted by Gornik at  $110 \text{ cm}^{-1}$  (90.6 micron  $\text{NH}_3$  line) showed that with the application of sufficient laser power the CCR absorption becomes practically equal to the low power ICR absorption [Gornik et al. 1978]. This implies that the cross sections for the CCR and ICR processes are nearly equal since the high laser power transfers a majority of the frozen out electrons into the  $N=0$  Landau level via the ICR transition and phonon emission.

## 1.2 Small Signal Detection Parameters

Independent of the mode of operation, bulk InSb responds to submillimeter radiation as any homogeneous detector. A homogeneous detector consists of a single piece of material whose low frequency conductivity (or some other electrical parameter) is a function of absorbed radiation of much higher frequency. The radiation is detected by measuring the change of voltage or current across electrical contacts on the sample. Two examples are bolometers and photoconductors. In contrast to heterogeneous detectors such as thermocouples or

photodiodes, homogeneous detectors must be electrically biased to work properly.

The InSb Rollin mode detector behaves in all respects like a simple bolometer. As such, a unit of absorbed high frequency power causes the same change of conductivity as a unit of absorbed low frequency power. The Putley mode detector in relatively high magnetic fields behaves like a simple photoconductor. The high frequency radiation then causes electronic transitions not possible via the low frequency electric field. A necessary condition for photoconductivity to occur is that the detector be operating in the photon absorption limit,  $h\nu \gg kT$ , where  $h$  is Planck's constant,  $\nu$  is the photon frequency,  $k$  is Boltzmann's constant and  $T$  is the temperature of the absorbing element. In both the Rollin and Putley modes, an important measure of detector performance is the ideal small signal responsivity,  $r$ , defined as the measured voltage or current per unit power *absorbed*. This is not to be confused with the absolute responsivity which is the measured voltage or current per unit power *incident* on the detector. Both parameters will appear frequently in this thesis. In general, both are a function of the time rate of change of the high frequency power. This leads to another important detector parameter, the response time,  $\tau_r$ . This is defined by  $\tau_r = 1/(2\pi B)$  where  $B$ , the bandwidth, is the frequency at which the response to sinusoidally chopped high frequency radiation is down by  $1/\sqrt{2}$  of its maximum value. A common feature of both bolometers and photoconductors is that if the input radiation has frequency much greater than  $1/\tau_r$ , then they will detect in a perfect square-law fashion. That is, the low frequency current or voltage measured across the detector will be proportional to the incident power or high frequency electric field squared.



### 1.3 Heterodyne Detection with Square-Law Detectors

Practical heterodyne detection is the process of superimposing a weak electromagnetic radiation (signal) with a much more intense coherent field (local oscillator or LO) and measuring the beat signal with some non-ohmic detector (mixer). If the detector displays square-law behavior, then the beat signal will always have a component at the difference frequency between the signal and the LO. In principle, this component can lie anywhere in the intermediate frequency (IF) range, between DC and  $\nu_{lo}$ . In practice, the mixer is most sensitive to beat signals that occur at frequencies less than the IF bandwidth,  $B_{if}$ . This bandwidth is determined either by the detector bandwidth itself or by later electronic filters. Another general feature of heterodyne detection is that an IF signal of frequency  $\nu_{if}$  is generated by radiation having a frequency either  $\nu_{lo} + \nu_{if}$  (upper sideband) or  $\nu_{lo} - \nu_{if}$  (lower sideband). Unless filtered or encoded in some way, these two components are indistinguishable. The simultaneous detection of both is called double-sideband (DSB) conversion.

There are several properties of the heterodyne process that give it distinct advantages over direct detection. Since the IF bandwidth can be controlled electronically, the resolution of the heterodyne receiver can, in principle, be made arbitrarily small. In practice, the resolution is made only as small as the experiment requires since, according to Eqn. 1.1, the signal-to-noise ratio always decreases with  $B_{if}$ . Many experiments in physics (e.g., the characterization of interstellar atomic and molecular lines in the far-infrared) require spectral resolution not easily attainable with direct detection receivers. For these experiments, the heterodyne receiver is usually the instrument of choice. A thorough and useful comparison of the heterodyne and direct detection modes has been given recently by Phillips and Watson [1984].

The canonical submillimeter receiver based on a square-law mixer is shown schematically in Fig. 1.1. The signal processing theory for this receiver configuration is discussed at length in Kraus [1966].

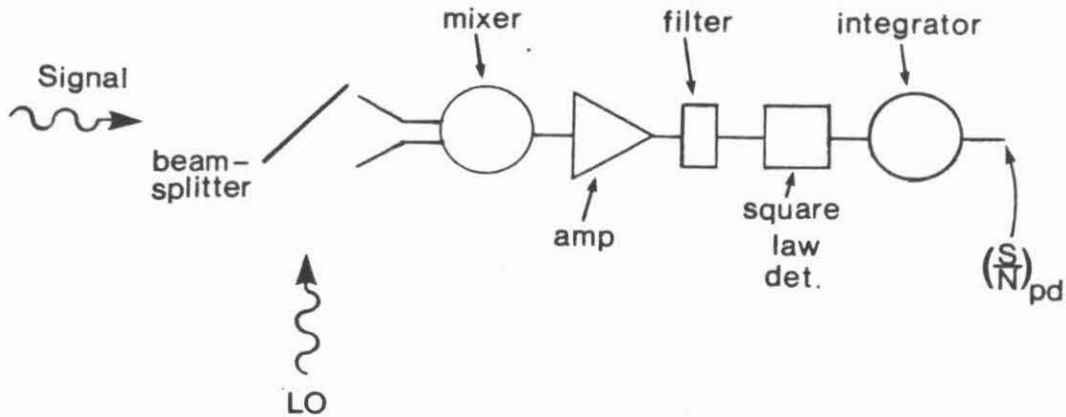


Fig. 1.1: Canonical submillimeter heterodyne receiver

The most important theoretical result is the following famous expression for the post-detection signal-to-noise ratio,

$$\left(\frac{S}{N}\right)_{pd} = C \left(\frac{S}{N}\right)_{if} \sqrt{B_{if} \tau_i}. \quad (1.1)$$

The parameter  $B_{if}$  is the IF bandwidth,  $\tau_i$  is the integration time and  $C$  is a constant of order unity that depends on the exact integration technique and signal chopping method. The quantity  $(S/N)_{pd}$  is a good indicator of the

performance of any heterodyne receiver.

Because integration time is somewhat arbitrary and the IF bandwidth varies with the application at hand, the quality of heterodyne receivers is usually measured by the IF signal-to-noise ratio. Assuming that the mixer is a homogeneous detector operating into a very high impedance preamplifier and that the total incident background power is much less than the amount of local oscillator power absorbed by the mixer ( $P_{lo}$ ), one can write

$$\left(\frac{S}{N}\right)_{if} = \frac{2\eta r^2 P_{lo} P_s}{\overline{V_d^2} + \overline{V_a^2} + \overline{V_{ph}^2}} \quad (1.2)$$

The quantity  $\eta$  is the power coupling efficiency (fraction of signal power incident on the receiver in the LO mode that is absorbed in the mixer), and  $\overline{V_d^2}$  and  $\overline{V_a^2}$  are the mean-square noise voltages due to detector mechanisms and the preamp, respectively. Note that the ideal responsivity,  $r$ , of a detector operating as a mixer can be much less than its responsivity in direct detection due to the loading effect of the absorbed LO power. As will be shown in Sec. 3.4, this is a very important effect for heterodyne bolometers. The quantity  $P_s$  is the incident signal power in the mode of the local oscillator. For a thermal source of temperature  $T_s$ ,

$$P_s = \frac{2h\nu B_{if}}{\exp(h\nu/kT_s) - 1} \quad (1.3)$$

where the factor of 2 is for double-sideband conversion and any opacity in the medium between the source and the receiver has been ignored.

The quantity  $\overline{V_{ph}^2}$  is noise due to fluctuations in the total incident radiation (photon noise). If the LO radiation is strictly coherent (e.g., from a laser or klystron), then the only significant source of noise is the zero-point fluctuation of the LO transverse mode. This fluctuation is a consequence of the quantum

mechanical uncertainty in the measurement of two non-commuting observables: the phase and amplitude of the electromagnetic field [Serber and Townes 1960]. The effect of the zero-point fluctuation is described by a power spectral density  $S(\nu)=h\nu/2$  [Marcuse 1980]. This power is down-converted to the IF exactly like signal radiation. If it is assumed that  $B_{if} \ll \nu_{lo}$ , the resulting double-sideband IF noise voltage is [Kingston 1978],

$$\overline{V_{pn}^2} = 2r^2 h \nu_{lo} B_{if} P_{lo}. \quad (1.4)$$

In the event that the zero-point noise dominates the denominator of Eqn. 1.2, one achieves the famous quantum-limited expression,

$$\left(\frac{S}{N}\right)_{if} = \frac{\eta P_s}{h \nu B_{if}} \quad (1.5)$$

Notice that the zero-point noise is independent of the source the receiver is detecting. This is why Eqn. 1.4 represents receiver noise and not signal. It is often called "LO induced shot noise" in the engineering literature because the same expression can be derived for a photoelectric detector by analyzing the signal current as discrete pulses obeying Poisson statistics [Kingston 1978]. Obviously, such a treatment would not apply to bolometers.

The noise equivalent power (NEP) is defined as the amount of signal power required to achieve  $(S/N)_{if}=1$ ,

$$NEP = \frac{\overline{V_d^2} + \overline{V_a^2} + 2r^2 h \nu P_{lo} B_{if}}{2r^2 \eta P_{lo}} \quad (1.6)$$

When the mixer is being characterized by thermal sources in the Rayleigh-Jeans limit, it is more convenient to characterize its performance by a parameter called the system noise temperature,  $T_{sys}$ . For double-sideband detection, this is related to the NEP by,

$$NEP = 2k T_{sys} B_{if} \quad (1.7)$$

From Eqn. 1.5 the quantum limited NEP is

$$NEP = \frac{h\nu B_{if}}{\eta} \quad (1.8)$$

and the quantum limited  $T_{sys}$  is

$$T_{QL} = \frac{h\nu}{2\eta k} \quad (1.9)$$

where double-sideband conversion is again assumed.

In practice, submillimeter heterodyne receiver performances are almost always measured using two Eccosorb foam loads, one cooled with liquid nitrogen (assumed 80K) and the other at ambient (assumed 295K). The ratio of the post detection noise powers with the two different loads is called, by convention, the Y factor. The relationship between the Y-factor and  $T_{sys}$  is

$$T_{sys} = \frac{295 - 80Y}{Y - 1} \quad (1.10)$$

This expression gets progressively more inaccurate as the frequency is increased. At near-infrared and shorter wavelengths, it should be replaced by,

$$T_{sys} = \frac{\frac{1}{2}P_s(295) - \frac{1}{2}P_s(80) \cdot Y}{(Y - 1)k B_{if}} \quad (1.11)$$

where  $P_s$  is given by Eqn. 1.3.

#### 1.4 The State of the Art in Submillimeter Heterodyne Detection

Shown in Fig. 1.2 are some system noise temperatures that represent the best reported performances to date. The numbers for the Putley mode detector are double-sideband whereas the Schottky and SIS numbers are single-sideband. These are the relevant performances for detecting a narrow spectral line having width of order 50 MHz. The quantum limited curve is calculated from Eqn. 1.9 assuming  $\eta=1$  and is applicable to the Putley mode detector only; the other mixers will have a quantum limited  $T_{sys}$  of twice this value. Notice that the performance obtained in this thesis work at 812 GHz for the Putley mode detector is at least a factor of 10 better than the only other receiver currently operating at that frequency: a Schottky diode based system. Judging from the direct detection measurements discussed in Chapter 4, it is probable that this excellent performance of the Putley mode receiver can be extended up to at least 1500 GHz.

Besides the advantage in sensitivity, the Putley mode is also superior to the Schottky in that it requires only about a microwatt of local oscillator power to achieve optimum performance. In contrast, any Schottky diode mixer requires a fraction of a milliwatt. Thus the Putley mode receiver can use any of several submillimeter local oscillator schemes currently in use. Two examples are the frequency multiplied klystrons or carcinotrons and far-infrared molecular laser sideband generation systems. Both of these schemes can generate continuously tunable radiation of several microwatts or more. The Schottky based receiver can observe only within its IF bandwidth of a strong molecular laser line.

The only advantage of the Schottky based system is that it has a much larger IF bandwidth than the Putley mode receiver. In practice, the bandwidth of the Schottky diode is limited only by the IF preamp. As we will see later, the Putley mode detector has an intrinsic time constant that limits its bandwidth to

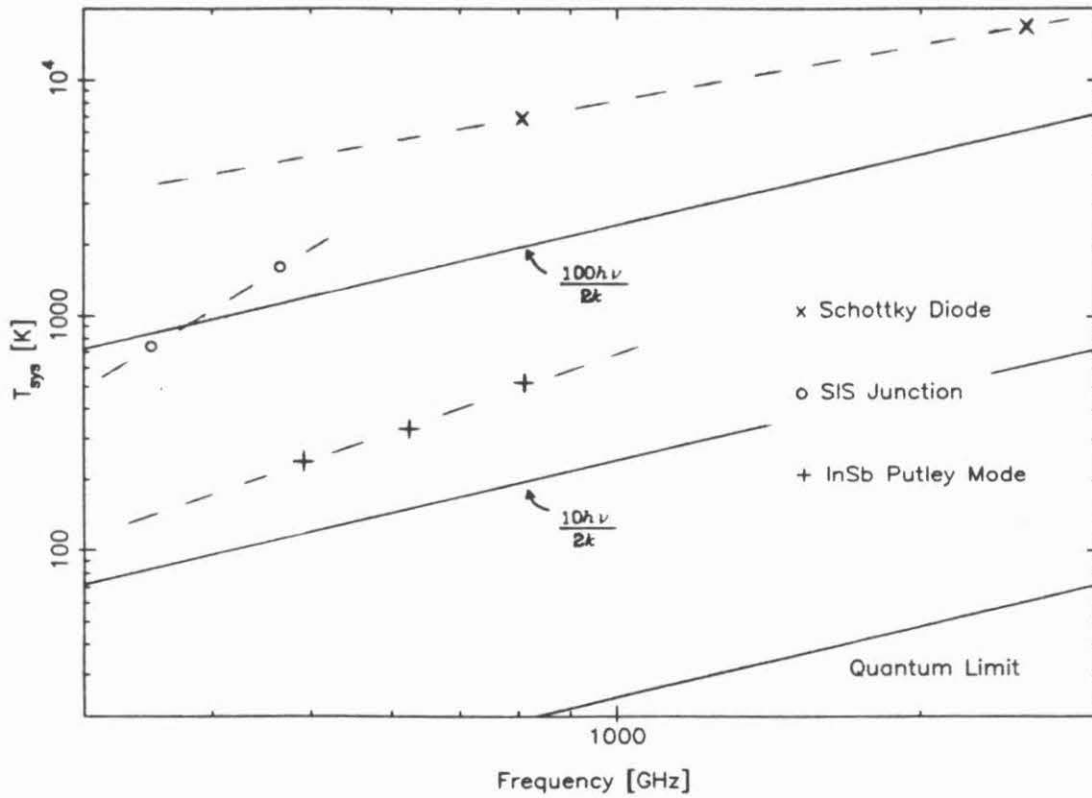


Fig. 1.2: The best heterodyne receiver performances reported to date. The Putley mode performance (this work) is for double-sideband conversion as is the quantum limited curve. The SIS points are due to Wengler et al. [1985] and the Schottky points are those of Roeser et al. [1984]. Both are single-sideband performances.

about 2 MHz. Fortunately, this bandwidth increases somewhat with magnetic field. When observing atomic and molecular lines that are broader than this bandwidth, the local oscillator frequency must be stepped. Further discussion of the Putley mode receiver is found in Chapter 4.



## 2. InSb Material Studies

### 2.0 Introduction

InSb is one of the most interesting and well-studied of all the common semiconductors. It received a great deal of attention in the 1950's due to its exceptionally low effective mass and relatively small band gap. It revolutionized near-infrared detection and rapidly became the standard millimeter wave direct detector. Recently, interest has revived in InSb as a model system for metal-insulator transitions in random media. In this chapter, I will discuss those materials properties of InSb that influence its performance as a submillimeter detector. I will also present some experimental results that were obtained over the course of the thesis work. In Sec. 2.4, DC conductivity data are shown in the range 1.5-10K. By comparing these data with established theories, it is shown that the InSb studied is intermediate between being simple metallic and simple insulating. In Sec. 2.7, I present absorption coefficient data that is not well described by Drudian theory (Brown 1985a). These data help explain the performance of InSb Rollin mode detector. Another interesting result, presented in Sec. 2.6, is the dramatic difference in the I-V characteristics of materials differing in electron concentration by only a factor of two. The material with the lower concentration displays pronounced negative differential resistance.

### 2.1 Material Handling and Preparation

The materials studied in this thesis were all n-InSb purchased as wafers from Cominco Inc. of Spokane Washington. They were grown perpendicular to the (211) plane and contain almost the lowest values of total impurity concentration achievable,  $n_{tot} \approx 2 \times 10^{14}/cc$ . The materials have about 25 to 50% variation in the impurity concentration across the wafer [Cominco 1981].

Because InSb is a relatively soft crystal and easily damaged, preparation of samples and various detectors was always done with the utmost care. To make slab samples or thin detectors, the wafers were first lapped down to about 15-20 mil thickness using a hand jig on silk. The usual lapping compounds were #220 grit SiC followed by #400 SiC. After lapping, the wafer was cut to the desired size using a diamond impregnated wire saw. The inevitable damage done by lapping and cutting was then removed by chemical etching. The etchant used was a CP-4 variant: 46% fuming nitric acid, 46% glacial acetic acid and 8% hydrofluoric acid. This etching leaves a very smooth and glossy surface. Sulfur-doped indium contacts are then pressed onto the freshly etched InSb. The contacted sample is soldered in a reducing atmosphere of hydrogen gas at a temperature slightly above 157C (the melting point of In). If the temperature became much higher than this, the InSb resistivity was usually increased in the soldering process. With proper execution this process produced strong, low resistance, ohmic contacts that were absolutely necessary for most of the studies made in this thesis.

## 2.2 InSb Band Structure

Many of the important far-infrared detector properties of InSb are related directly to its remarkable band structure. In this section, I will briefly review the theory of the band structure under the conditions of zero and quantizing magnetic fields. I will limit the discussion to the conduction band.

Single crystal InSb is a III-V compound semiconductor with the zincblende structure. From early cyclotron resonance measurements, the conduction band was found to have its minimum at  $k=0$ . The effective mass at this minimum was found to be surprisingly low,  $m^* \sim .013m_0$  at room temperature [Dresselhaus 1955]. Infrared absorption measurements revealed that the bandgap was also

relatively small:  $E_g \approx 0.16$  eV at 300K and  $E_g \approx 0.23$  eV at 4.2K [Roberts and Quarrington 1955]. These gaps are about a factor of 4 less than those of germanium.

The first accurate explanation of the InSb band structure was given by Kane [1957]. He showed that the small effective mass at the bottom of the conduction band could be attributed to significant mixing between the s-like (conduction band) and p-like (valence band) cellular functions via the  $\mathbf{k} \cdot \mathbf{p}$  interaction. He solved for the band energies by diagonalizing the crystal Hamiltonian in the eight dimensional space spanned by the 2 s-like and 6 p-like states. The following expression was found for the conduction band energy,

$$E_c = \frac{-E_g}{2} + \left[ \frac{E_g^2}{4} + E_g E_0 \right]^{1/2} \quad (2.1)$$

where  $E_g$  is the band gap energy,  $E_0 = \frac{\hbar^2 k^2}{2m_o^*}$ , and  $m_o^*$  is the effective mass at the bottom of the conduction band.

When a quantizing magnetic field is applied, the Bloch states are no longer a good basis set. However, working with the same eight dimensional space as Kane, Bowers and Yafet [1959] showed that it was possible to diagonalize the magnetic Hamiltonian including the important diamagnetic (Landau splitting), paramagnetic (spin splitting) and atomic spin-orbit interactions. They derived an expression very similar to Eqn. 2.1 with  $E_0$  replaced by  $L_0$ ,

$$L_0 = \frac{\hbar^2 k_z^2}{2m_o^*} + (N + \frac{1}{2})\hbar\omega_c \pm \frac{1}{2} \mu_B g^* H. \quad (2.2)$$

$$\omega_c = \frac{eB}{m_o^* c} \quad (2.3)$$

In deriving these expressions, it has been assumed that  $\mathbf{B}$  is uniform and directed along the z axis. The effective g-factor is given by,

$$g^* = -\frac{m_l}{m_o^*} \frac{\Delta}{\Delta + 3E_g/2} \quad (2.4)$$

where  $\Delta$  is the spin-orbit splitting ( $\Delta = .81$  eV in InSb [Herman et al. 1963]). The magnetic version of Eqn. 2.1 is plotted in Fig. 2.1 for a field of 50 KG. The parameter  $k$  is the momentum wavevector component parallel to the field. The  $k$  axis is scaled in units of the Fermi amplitude,  $k_F$ , for a carrier concentration of  $5 \times 10^{13}$ /cc. The Landau sub-bands are denoted by  $N=0$  and  $N=1$  with the spin quantum number,  $S_B$ , either  $+1/2$  (spin parallel to  $\mathbf{B}$ ) or  $-1/2$  (spin anti-parallel to  $\mathbf{B}$ ).

### 2.3 Impurity Studies

The influence of shallow donors in most semiconductors is described well by effective mass theory [Madelung 1978]. The result is that each donor generates bound electron states that are homologous with the bound states of the free hydrogen atom. The energy of the  $i^{\text{th}}$  donor level,  $E_i$ , and the effective Bohr radius of the ground level,  $a^*$  are given by,

$$E_i = \frac{-13.6}{i^2} \frac{m_o^*}{m \epsilon_o^2} [eV] \quad (2.5)$$

$$a^* = 5.29 \times 10^{-9} \frac{m}{m_o^*} \epsilon_o. \quad (2.6)$$

Each of these levels is  $2N_d$ -fold degenerate where  $N_d$  is the total number of donors present and the factor of 2 is for spin. Using the accepted values  $m_o^* = .0139$  and  $\epsilon_o = 17.8$  [Johnson and Dickey 1970, Hass and Henvis 1962], we find the following values for InSb:  $E_1 = 0.60$  meV and  $a^* = 68$  nM.

The hydrogenic model is invalid when there is overlap of the electronic wavefunctions for adjacent donor sites. With a relatively small amount of overlap, the degeneracy of the hydrogenic model is broken as the impurity states

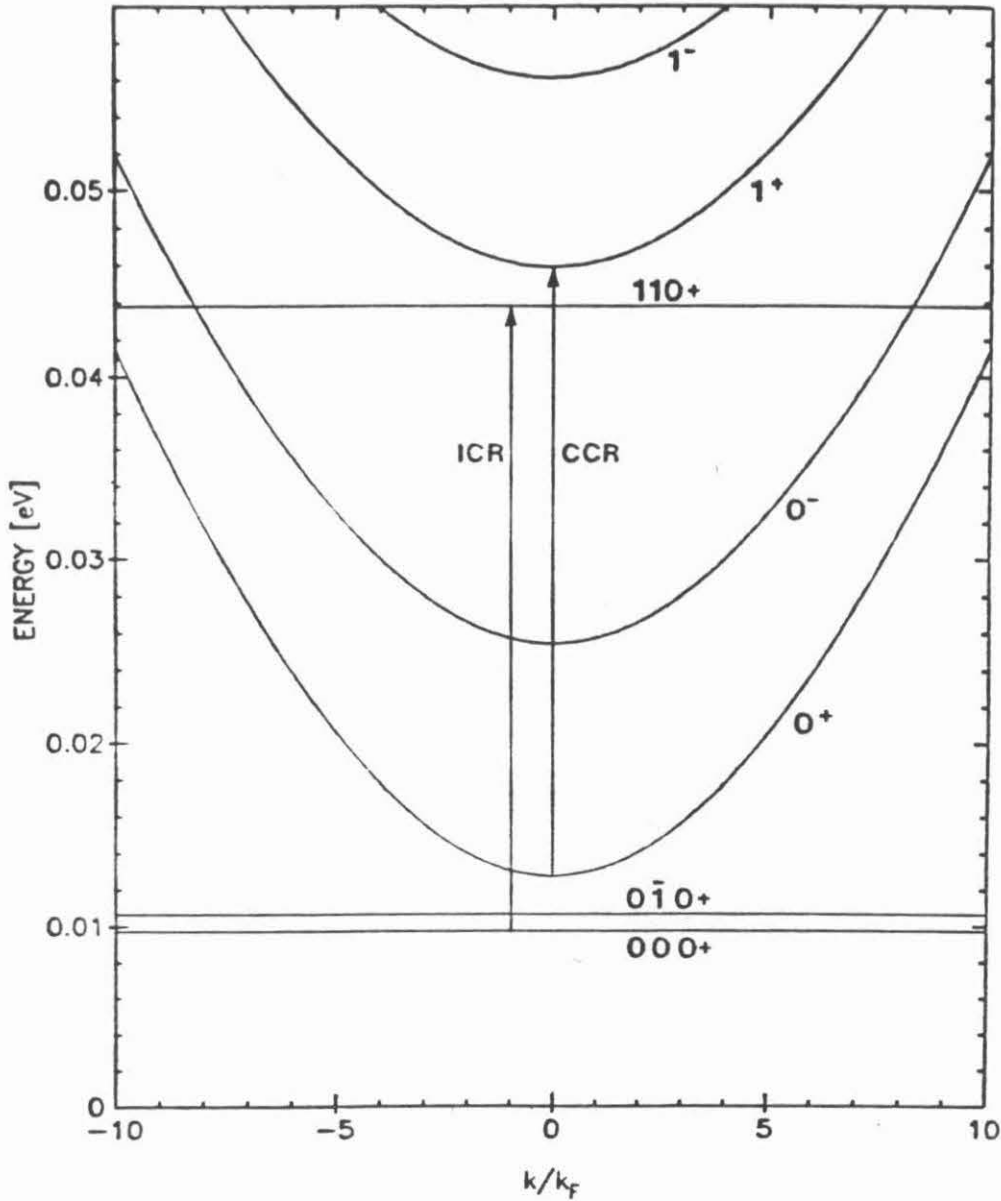


Fig 2.1: Lowest two Landau sub-bands, important bound states and dominant cyclotron resonance transitions for electrons in a quantizing magnetic field,  $B=50$  KG. The Landau sub-bands are denoted by  $N=0$  and  $N=1$  with the spin quantum number,  $S_B$ , either + (spin parallel to  $\mathbf{B}$ ) or - (spin anti-parallel to  $\mathbf{B}$ ). The impurity states are denoted by the four quantum numbers  $(N, M, \lambda, S_B)$  after Yafet et al. [1956]. The impurity state energies were calculated by Wallis [1958].

split into a narrow range of energies (henceforth called the impurity band) just below the the bottom of the conduction band. Experience with Si and Ge has shown that the impurity band begins to form when  $d_i \lesssim 5a^*$  where  $d_i$  is the average distance between donors [Putley 1960]. Assuming that  $d_i = n_d^{-1/3}$ , the hydrogenic model is valid in InSb only when  $n_d \lesssim 2.5 \times 10^{19} \text{ cm}^{-3}$ , where  $n_d$  is the donor density. For a much larger amount of overlap,  $d_i \lesssim a^*$ , it is thought that the donor band merges completely with the conduction band. For InSb this occurs when  $n_d \gtrsim 3.2 \times 10^{15} \text{ cm}^{-3}$ . In this range, the electron density of states,  $D(E)$ , increases monotonically starting at zero slightly below the pure crystal conduction band edge. The effect of the donors is simply to cause a smooth "tail" but no local minima in  $D(E)$ . As shown below, all of the InSb material studied in this thesis has impurity densities in the range,  $n_d \sim 1.0 - 3.0 \times 10^{14} / \text{cc}$ . According to the criteria just stated, this is intermediate doping. In this case the impurity band probably overlaps the conduction band but the form of the density of states is complicated [Madelung 1978].

The influence of an externally applied magnetic field on the impurity levels in semiconductors is measured by the ratio,  $\gamma = \frac{1}{2} \hbar \omega_c / E_1$ , where  $\omega_c = eB / (m^* c)$  is the cyclotron frequency. For isolated impurities and  $\gamma \ll 1$ , the magnetic field can be treated as a weak perturbation that causes simple Zeeman-like splitting of the energy levels. This description applies to relatively pure Si, Ge and some III-V materials for fields up to several kilogauss. In materials having intermediate doping concentration, the first-order effect of the magnetic field is to shrink the overlapping wavefunctions, particularly in the plane normal to the field. As B is increased, the impurity band shrinks and isolated impurity levels are created. The magnitude of field required to generate this "magnetic freeze-out" can be conservatively estimated by equating half the distance between donors to the cyclotron radius of the ground Landau sub-level,  $R_B = (\hbar c / eB)^{1/2}$ .

For InSb with  $n_d = 2 \times 10^{14} / \text{cc}$ , the freeze-out should occur at  $B \sim 6$  KG. Even for this relatively small field,  $\gamma \sim 6$ . Therefore, a simple Zeeman perturbation treatment of the impurity levels is inapplicable.

The theory of the donor levels when  $\gamma \gg 1$  is necessarily based on approximation techniques because the full Hamiltonian is not separable. The approach has been to introduce an orthogonal set of trial donor wavefunctions and to solve for the energy levels by the Rayleigh-Ritz variational technique. The variational solution for the ground state was first worked out by Yafet et al. [1956]. Shortly thereafter, solutions for several excited states were found by Wallis and Bowlden [1958]. Their results for the most important states in  $B = 50$  KG are shown schematically in Fig. 2.1. Following Yafet the impurity states are denoted by the set of quantum numbers,  $(N, M, \lambda, S_B)$ , where  $N$  is the associated Landau level,  $M$  is the  $z$  component of the angular momentum,  $\lambda$  is the quantum number for the energy in the one-dimensional Coulomb potential along the  $z$  axis, and  $S_B$  is the spin quantum number. Experimental verification of the impurity state structure shown in Fig. 2.1 has been provided by Kaplan [1969] and by Kuchar et al. [1977].

One of the most important applications of the quantizing B-field band structure is in determining the impurity concentration of intermediately doped InSb. The procedure, first exercised by Putley [1960], is a statistical analysis of Hall data. The exact procedure followed here differs slightly from Putley's and is discussed at length in Appendix 1. The Hall experiment and the associated data are also presented there. The resulting impurity concentrations are summarized in Table 2.1 and will be used repeatedly throughout the course of this thesis. It should be mentioned here that all of the materials tested showed no obvious sign of carrier freeze-out down to the lowest temperatures attained in the Hall measurements,  $\sim 3$ K. This was evident by the fact that the Hall coefficient was practically constant with temperature. Putley [1966] also observed this lack of

freeze-out on very similar material down to much lower temperatures,  $\sim 1.3\text{K}$ . In fact, no one has ever reported a freeze-out in n-InSb based on a strong temperature variation of the Hall coefficient.

Material	4002	4177	4190
Carrier concentration, $n = n_d - n_a$ ( $\times 10^{13} / \text{cm}^3$ )	3.4	7.7	2.6
Total impurity concentration, $n_d + n_a$ ( $\times 10^{14} / \text{cm}^3$ )	4.1	3.8	2.2
Compensation ratio, $n_a / n_d$	0.85	0.52	0.78
Donor concentration, $n_d$ ( $\times 10^{14} / \text{cm}^3$ )	2.2	2.3	1.2

#### 2.4 DC Conductivity

Despite the enormous number of experiments and theoretical studies conducted on InSb in the past 30 or so years, there is still no good understanding of the DC conductivity at liquid helium temperatures. In this section I will present my experimental data and compare it to some well-known theories. This data will be very important later in Chapter 3 when I discuss the performance of the



InSb Rollin-mode detector.

### 2.4.1 DC Conductivity Theory

Experimental evidence has shown that the DC conductivity,  $\sigma$ , in all solids can be characterized by two different forms of temperature dependence. *Metallic* behavior is characterized by finite conductivity at  $T=0$  and a slowly varying conductivity vs. temperature for  $T \geq 0$ . Usually the conductivity will obey some power law that depends on the dominant scattering mechanisms. *Insulating* behavior is characterized by a vanishing DC conductivity at  $T=0$  and exponential dependence for higher temperatures. The vanishing of  $\sigma$  at  $T=0$  reflects the fact that the Fermi energy in an insulator must lie either in a gap in the single particle states or else it lies at a point in the energy spectrum where the states are strictly localized. The exponential behavior for  $T > 0$  follows from the fact the conductivity is activated,  $\sigma \propto \exp(-\Delta E/kT)$ , where  $\Delta E$  depends on the exact mechanism of conduction [Madelung 1978]. For example, if the current is dominated by electrons thermally excited to extended states,  $\Delta E$  is simply the separation between the Fermi energy and the energy of the lowest conducting state.

For crystalline metals, there exist well-established theories of DC conductivity that lead to simple formulation once the scattering mechanism is characterized. In high quality n-InSb at the temperatures of concern here ( $\leq 20K$ ), the dominant scattering mechanism that limits the conductivity should be that due to ionized impurities. The interaction with the lattice can be handled by properly using the electron effective mass and the background dielectric constant,  $\epsilon_0$ . The ionized impurity scattering potential is usually assumed to have a screened Coulomb form. Assuming  $T \ll T_F$ , the Boltzmann equation then predicts a temperature independent DC conductivity [Madelung

1978]. This is commonly called the residual resistivity when applied to metals. The single electron expression for the residual conductivity is [Putley 1960],

$$\sigma_r = \frac{2^{1/2} \epsilon_0^2 n (k T_F)^{3/2}}{\pi e^2 N_i f(z)} \quad (2.7)$$

where,

$$f(z) = \ln(1+z) - \frac{z}{1+z} \quad (2.8)$$

and

$$z = \frac{16\pi m^* \epsilon_0 (k T_F)^2}{3h^2 n e^2} \quad (2.9)$$

Assuming that  $T \gg T_F$  so that classical statistics apply, the Boltzmann equation leads to the famous Brooks-Herring formula [Brooks 1955],

$$\sigma = \frac{4n \epsilon_0^2 (2kT)^{3/2}}{\pi^{3/2} N_i e^2 (m_o^{star})^{3/2}} \left[ \ln \left( \frac{6m_o^* \epsilon_0 (kT)^2}{\pi e^2 \hbar^2 n} \right) - 1 \right]^{-1} \quad (2.10)$$

where  $N_i$  is the total ionized impurity concentration. This expression is known to predict accurately the conductivity in pure n-InSb at temperatures of about 20K and slightly higher [Kinch 1966].

#### 2.4.2 DC Conductivity Experiment

The DC conductivity was obtained for two samples made of the 4002 and 4177 materials, respectively. The experimental procedure consisted of several simple but carefully executed steps. First the samples were mounted in oxygen-free copper flanges which were secured to the cold plate of a liquid helium cryostat. The samples were thermally isolated by completely surrounding them with a radiation shield and by cementing the electrical leads to the

cold plate. The dynamic resistance ( $Z$ ) of the the samples was then measured under conditions of zero bias and varying temperature. From the dynamic resistance and the known dimensions of the samples, the DC conductivity was then calculated. Bath temperatures below 4.2K were achieved by reducing the pressure above the liquid helium with a rotary pump. The value of  $T_b$  was determined using a standard pressure vs. temperature table [White 1979]. Temperatures above 4.2K were achieved "on-the-fly" as the cryostat warmed up after complete boil-off of the LHe. The value of  $T_b$  in this range was determined using a calibrated Si diode (manufactured by Lake Shore Cryotronics). The resulting uncertainty in temperature is less than 0.1K in both ranges. The electronic technique used to measure  $Z$  is described in Appendix 2.

To make sure that the samples were not pathological, I performed several separate tests. For example, I measured the conductivity of both samples at 77K and found it to be within the manufacturer's specification range. This precluded the possibility that the samples were damaged during soldering or handling. It is well known that mobility of InSb of this purity is easily reduced drastically by stress during careless handling or overheating during soldering [Peter Bratt, private communication]. The 77K conductivity test was corroborated by the following etch pit test. After the samples were lapped and initially etched to remove the damage but before the contacts were put on, the samples were put in highly de-ionized water and etchant is added drop by drop. During this process, the samples showed no surface pits. Experience has shown that any etch pits seen during this test indicate a high concentration of defects [Peter Bratt, private communication].

Shown in Fig. 2.2 are the experimental results from 1.5 to  $\sim 10$ K. There are several important features here. First, notice that the 4177 sample has the larger conductivity over the whole range. This is consistent with the Hall data

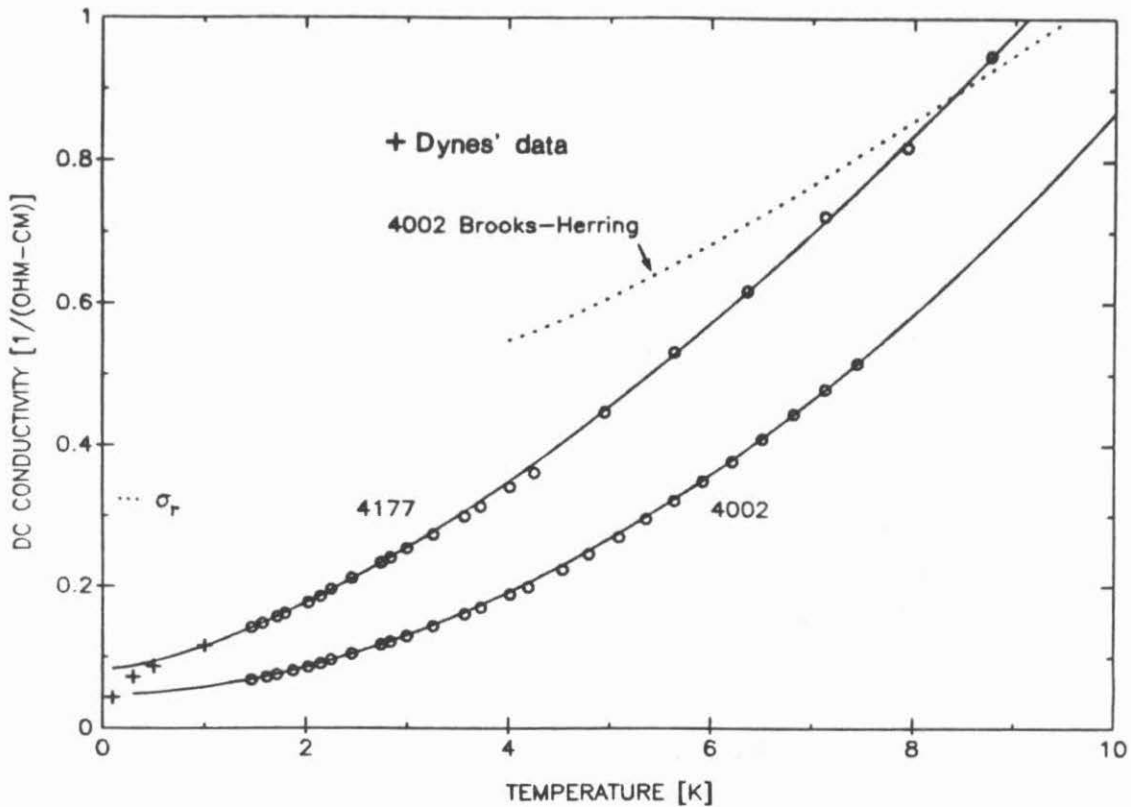


Figure 2.2: DC conductivity of two InSb samples at low temperatures. Data points are shown by circles. The continuous lines are the least-squares fits and terms are defined in the text.

which indicated that the carrier concentration of the 4177 sample is greater by a factor of 2.3. The conductivity of both samples increases monotonically and the rate of increase is very similar. However, both samples appear to approach non-zero conductivity in the limit of 0 K. This behavior led me to fit the data with a functional form,  $\sigma(T) = \sigma_0 [1 + (T/T_t)^x]$ . The values of  $\sigma_0$  and  $T_t$  were determined from a least-squares fit. The value of  $x$  was that which gave the minimum standard deviation of  $\sigma(T)$  over the whole range (only two significant figures in  $x$  were used). The results of the fit along with other important properties of the samples are summarized in Table 2.2. Also shown in Fig. 2.2 are the

conductivity data points obtained in the sub-1.0K region by Dynes et al. [1983]. Their material is similar to my 4177 material and their results are apparently the first published data on the sub-0.3K conductivity in such pure InSb. Notice that their data points are apparently concave downward in the sub-1.0K region.

<b>Table 2.2</b>			
<b>DC transport characteristics of three InSb materials</b>			
Material	4002	4177	4190
Conductivity mobility, (cm <sup>2</sup> /V-s) @ 77K	5.9x10 <sup>5</sup>	4.8x10 <sup>5</sup>	6.1x10 <sup>5</sup>
DC conductivity @ 4.2K, (1/Ω-cm)	0.20	0.36	0.18
$\sigma_0$ (1/Ω-cm)	0.0475	0.0821	*
$T_f$	2.24K	1.83K	*

\* not determined

Displayed in Fig. 2.2 is the prediction of the simple theories discussed above. Notice that the residual conductivity for both the 4002 and 4177 materials is considerably larger than the 0K extrapolated limit of the data. Also shown in Fig. 2.2 is the prediction of the Brooks-Herring formula for the 4002 material. Notice that it significantly overestimates the conductivity over the entire range shown. The prediction is not carried below about 4K because the Brooks-Herring theory does not apply under degenerate conditions, which occur when

$T \lesssim T_F = 3.2\text{K}$  in the 4002 material. The Brooks-Herring formula did yield good agreement with the 4002 data at about 18K as was observed previously by Kinch [1966]. In the past, the failure of the B-H formula below about 10K has been ascribed to the fact that it is derived using the Born approximation of scattering. Recall that the Born approximation assumes that the electronic de-Broglie wavelength is much shorter than the range of the scattering potential. For a screened Coulomb potential and degenerate statistics, the Born approximation is valid when  $(2k_F \lambda_s)^2 \gg 1$  where  $\lambda_s$  is the screening length [Meyer and Bartoli 1981]. Using the standard Thomas-Fermi form of  $\lambda_s$ , we find that the left side of this inequality is 2.1 for the 4002 material. Thus the Born approximation is suspect. Surprisingly, an early analysis using the more accurate partial wave scattering technique predicted larger conductivities than those of the B-H theory under identical conditions [Blatt 1957]. The more elaborate studies of Meyer and Bartoli [1981] lead to the same conclusion. Unfortunately, their solutions are not analytic and are not presented for InSb in the sub-4.2K region.

Judging from the combined sub-1.0K and 1.0-10K data shown in Fig. 2.2, the DC conductivity of the 4177 sample is not thermally activated. This is shown by the following argument. By twice differentiating the activated conductivity function, we see

$$d^2\sigma/dT^2 = \sigma \frac{\Delta E}{kT^3} \left[ \frac{\Delta E}{kT} - 2 \right]. \quad (2.11)$$

Thus at a temperature  $T = \Delta E / 2k$  there is an inflection point below which  $\sigma(T)$  is concave upward and above which it is concave downward. For n-InSb we expect  $\Delta E$ , if it exists, to be some fraction of the hydrogenic ground state binding energy which is  $\approx 0.6$  meV. The inflection point should then be at about 3.5K or less. Clearly, there is an inflection point in the combined 4177 data but the

second derivative at that point has the wrong sign for activated conductivity. In other words, the experimental data are concave downward below about 1.0K and concave upward above this temperature. Furthermore, it appears that the very low data can be fit with a form  $\sigma = \sigma_0(1 + AT^{\frac{1}{2}})$  where  $\sigma_0$  and A are constants [Dynes, private communication]. This behavior is in accordance with a recent theory of impurity conduction in metals [Altshuler and Aronov 1979].

### 2.4.3 DC Conductivity Discussion

We have just demonstrated that the DC conductivity at temperatures less than  $T_F$  lies well below the prediction of simple residual conductivity theory. On the other hand, the temperature variation of the conductivity is not consistent with activated behavior. This leads to the conclusion that the present InSb is intermediate between being simple crystalline metallic and insulating. There are several possible reasons why the behavior is not simple metallic, all of which are beyond the scope of this thesis. However, I would like to comment briefly on these ideas to bring the discussion into a modern context. The first reason why the simple crystalline theories may fail is due to strong scattering. As emphasized by Peierls [1955], any semi-classical theory based on the Boltzmann equation or any quantum mechanical theory based on a perturbation approximation will fail when the scattering is very strong. The strength of the scattering in a metal is measured by the product  $k_F l$  where  $k_F$  is the Fermi wavevector and  $l$  is the mean free path. This is equivalent to the product  $2E_F \tau / \hbar$ , assuming that  $l = v_F \tau$  where  $\tau$  is the momentum relaxation time. Strong scattering is prevalent when this product is  $\lesssim 1$ . Using the carrier concentrations given in Table 2.1 and the experimental DC conductivity to obtain  $\tau$  via  $\sigma = ne^2 \tau / m^*$ , we find that  $2E_F \tau / \hbar \approx 0.4$  for the 4177 material and  $\approx 0.2$  for the 4002 material, both taken at 4.2K. This implies that scattering is indeed very strong. The physical

reason behind this can be seen by comparing the screening length to half the inter-impurity length. Inspection of Table 2.3 shows that these quantities are actually quite comparable. Thus, the electrons are never out of range of an impurity potential and are probably always being scattered.

A second possible reason why the simple metallic theory may fail is due to electron correlation effects. In calculating the cross section leading to Eqn. 2.7 and 2.10, the scattering is assumed to take place with a screened Coulomb potential. Beyond the screening length, the other electrons are implicitly assumed to be blind. In reality, the electrons are correlated over a very large distance and in the process of screening an ionized impurity can undergo collective excitations, which in one treatment are called plasmons [Pines 1963]. The plasmons have a harmonic oscillator spectrum with a ground state energy  $\frac{1}{2} \hbar \omega_p$  where  $\omega_p$  is the plasma frequency. Roughly speaking, we expect plasmon excitations to be possible when  $\hbar \omega_p \gtrsim kT$  where  $T$  is the bath temperature. This situation doesn't usually arise in common metals because the plasma frequency is so large. However, inspection of Table 2.3 reveals that  $\hbar \omega_p / kT$  is already about 1.2 for the 4002 material at 4.2K. There has been some success recently in theoretically including correlation effects into the impurity scattering problem. The most notable work is that of Altshuler and Aronov [1979]. Their predictions have been experimentally confirmed by Morita et al. [1982]. Unfortunately, the theory applies only to samples in which  $k_F l \gg 1$ . Thus it doesn't apply rigorously to the present InSb despite the fact that sub-1.0K data of Dynes shown in Fig. 2.2 give the predicted form.

To see physically why the conductivity is not activated, or equivalently, why the electrons do not bind to donors, we compare the value of the Bohr radius (68 nm) to half the inter-impurity length. Inspection of Table 2.3 shows that these quantities are nearly equivalent and nearly equal to the screening length.



Thus, besides being partially screened, the potentials from neighboring impurity atoms overlap somewhat. The time that an electron remains within the influence of one impurity is apt to be so small that binding cannot occur.

<b>Table 2.3</b>		
<b>Physical parameters of two InSb materials</b>		
Material	4002	4177
Fermi temperature	3.2K	5.5K
Thomas-Fermi screening length, $\lambda = \sqrt{\frac{2\epsilon_0 E_F}{12\pi n e^2}}$	73 nm	64 nm
Inter-impurity length, $N_i^{-1/3}$	135 nm	138 nm
Free electron plasma frequency, $f_p = \sqrt{\frac{n e^2}{\pi m^* \epsilon_0}}$	105 GHz	158 GHz
Residual conductivity, (1 / Ω-cm)	0.32	1.37

These experimental results are consistent with the vast majority of results published to date. As discussed by Walton and Dutt [1977], all of the DC conductivity results available indicate that n-InSb with donor concentrations

$\approx 1 \times 10^{14}$ /cc shows no sign of activated behavior. They further state that the temperature dependence of the conductivity in such material should reflect variations of the electron mobility in the conduction band. Unfortunately, it appears that there is no satisfactory theory of the mobility in material having the purity and compensation of the samples tested here.

## 2.5 Thermal Conductance

In addition to the DC electrical conductivity, an important property of InSb for submillimeter detector applications is the thermal conductance of the electrons to the lattice. In this section I will present my experimental results for the 4002 and 4177 samples. They will prove to be very useful in Chapter 3 when we discuss the performance of the Rollin mode detector.

At liquid helium temperatures, an electron relaxes energetically by interacting with other electrons and acoustical phonons. If the relaxation time with electrons is much less than with phonons, then the electron system as a whole will self-thermalize. Consequently, it can be ascribed a distribution function and a well-defined temperature,  $T_e$ , greater than or equal to the lattice temperature  $T_b$ . The requirements for self-thermalization can be re-stated in terms of the electronic density [Frohlich and Paranjape 1956]. The requirement for InSb is  $n \gtrsim 10^8$ /cc at 4.2K. This is certainly true for all of our materials. Since freeze-out does not occur in any of these materials down to 1.5K and probably lower, an electron gas temperature will always be assumed for samples in zero magnetic field.

When an InSb sample is biased with electric fields,  $E \gtrsim 0.1$ V/cm,  $T_e$  begins to rise significantly above  $T_b$ . There is an average power flow,  $P_e$  between the electrons and the lattice. Assuming that the electrical power absorbed by the bolometer flows directly to the bath without heating up any other material, one

can apply the steady-state power balance condition,

$$P = G_e(T_e - T_b). \quad (2.12)$$

The quantity  $G$  is the static thermal conductance and is, in general, a function of both  $T_e$  and  $T_b$ . A physically more interesting quantity is the thermal conductance per electron,  $G_e = G/N_e$ , where  $N_e$  is the total number of electrons in the sample. A theoretical expressions for  $G_e$  was first derived by Kogan [1963] assuming acoustical phonon interactions. I will not go into the theory in detail but only mention that  $G_e \propto (m^*)^{2.5}$  if the electron-phonon interaction is calculated using the deformation potential. This explains qualitatively why InSb displays such pronounced hot electron effects. The low effective mass,  $m^* = 0.0139 m_0$ , makes the electronic thermal conductance about two orders less than that of Ge or Si at comparable electric fields. Thus the fractional change of  $T_e$  with input power is very large compared to most other materials. This is the reason for the large bolometric responsivity, as discussed further in Chapter 3.

Knowing the functional form for the DC conductivity, the value of  $G_e$  for any material can be obtained very simply from the I-V characteristics of a representative sample. The key idea here is that the conductivity is determined mainly by electron interactions with ionized impurities and perhaps other crystal defects. These interactions depend only on  $T_e$ . Therefore, the conductivity and the resistance depend only on  $T_e$  and one can write

$$G_e(T_e, T_b) = \frac{I^2 R}{N_e (T_e - T_b)}. \quad (2.13)$$

In practice, this expression was evaluated for the 4002 and 4177 samples as follows. At each point of the I-V curves shown in Fig. 2.4a, the resistance was measured and used to calculate the DC conductivity. The electron temperature was then determined by equating the measured conductivity to the functional

form found to fit the data in Sec. 2.4,  $\sigma(T) = \sigma_0 [1 + (T_e / T_i)^2]$ . The total number of electrons was calculated using the concentrations in Table 2.1 and the known dimensions of the sample.

Shown in Fig. 2.3a and 2.3b are the curves of  $G_e$  determined by the above procedure. There are two notable features here. First, the value of  $G_e$  in 4002 is nearly twice that in the 4177 material. Similar behavior was seen long ago by Kinch and was attributed

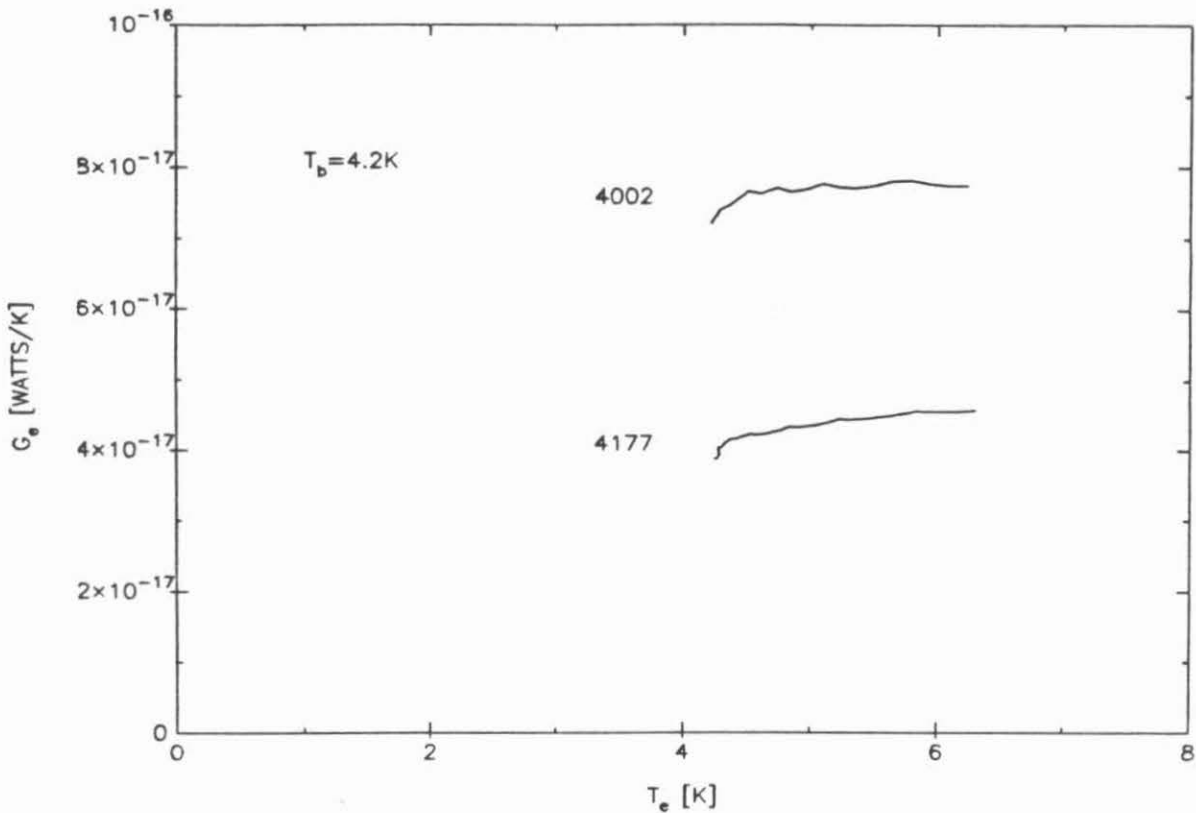


Figure 2.3a: Static thermal conductance per electron vs electron temperature for two InSb samples at 4.2K bath temperature.

to screening effects [Kinch 1966]. He surmised that the electrons screen the electron-phonon interaction so that materials with greater electron

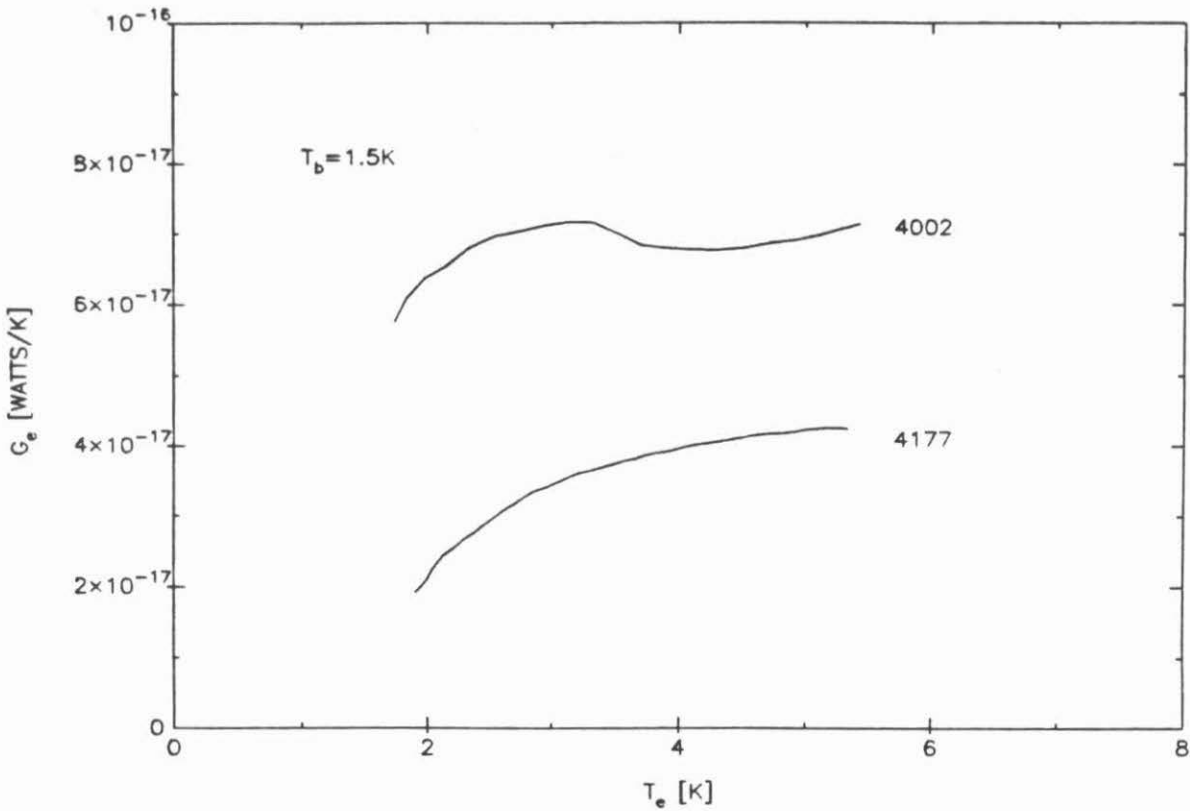


Figure 2.3b: Static thermal conductance per electron vs electron temperature for two InSb samples at 1.5K bath temperature.

concentration (e.g., the 4177 material in the present study) would have smaller  $G_e$ . This issue has been taken up more recently by Kahlert and Bauer [1973]. The second interesting feature of Fig. 2.3 is that  $G_e$  for both materials is nearly constant in the range  $T_e = 2.0$  to  $6.0$ K. This will be a very useful fact when we come to analyzing the bolometer responsivity in the next section and in Chapter 3.

## 2.6 I-V Characteristics: Demonstration of Bolometer Theory

In this section, we display the I-V characteristics of samples made of different materials and cooled to various temperatures in the liquid helium range. This section will serve to demonstrate the dramatic effect that seemingly slight differences in material parameters have on the I-V curves. In addition, this section will serve to introduce, demonstrate and elaborate on bolometer theory. As we will see, this theory is very useful in explaining the performance of the Rollin mode detector in Chapter 3.

Shown in Fig. 2.4a are the I-V curves of a 4002 and 4177 material sample at bath temperatures of 4.2 and 1.5K. These curves provide an interesting contrast of different materials since the geometries of the two slabs (given in Table 2.4) are nearly identical. Notice the dramatic difference in the non-ohmic behavior of the curves. The dynamic resistance of the 4002 sample varies rapidly with bias current and actually goes negative in a small region at 1.5K.

As shown first by Jones [1953], the magnitude of the ideal responsivity of any bolometer can be predicted directly from the I-V curve. If we assume constant current bias conditions, the expression for the magnitude of the ideal responsivity is,\*

$$r = \frac{R-Z}{2RI} \quad (2.14)$$

This expression was evaluated for the I-V curves shown in Fig. 2.4a and the results are shown in Fig. 2.4b. Notice that a maximum in the responsivity occurs for both samples at both temperatures. The value of the maximum increases significantly as the temperature decreases, a well-known experimental

\* Constant current bias is always applied to the InSb bolometers here because, like all "negative" (i.e.,  $dR/dP < 0$ ) bolometers, it then operates with maximum responsivity, maximum stability and minimum time constant relative to all possible bias conditions [Zwerdling et al. 1968].

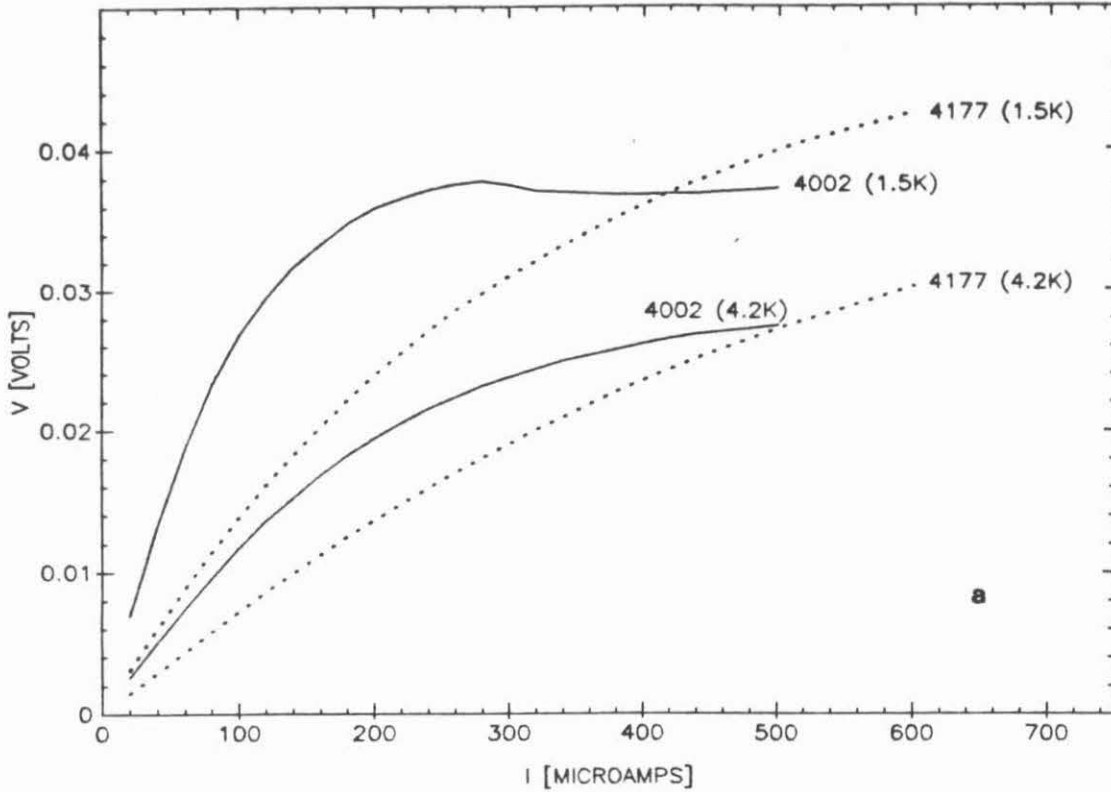


Fig. 2.4a: Experimental I-V curves for two InSb samples at 1.5K and 4.2K

fact. Also notice that the maximum occurs at a bias current well below that at which the dynamic impedance goes to zero. Zero or negative dynamic impedance is seen in many good bolometers and does not necessarily indicate any critical behavior or threat of instability.

A useful exercise is to introduce another expression for the ideal bolometric responsivity that is related to the sample physical properties. As shown by Zwerdling et al. [1968], the expression in Eqn. 2.14 can be re-stated as

$$r = \frac{-I dR / dP}{1 - I^2 dR / dP} = \frac{-I (dR / dT_e) (dT_e / dP)}{1 - I^2 (dR / dT_e) (dT_e / dP)} \quad (2.15)$$

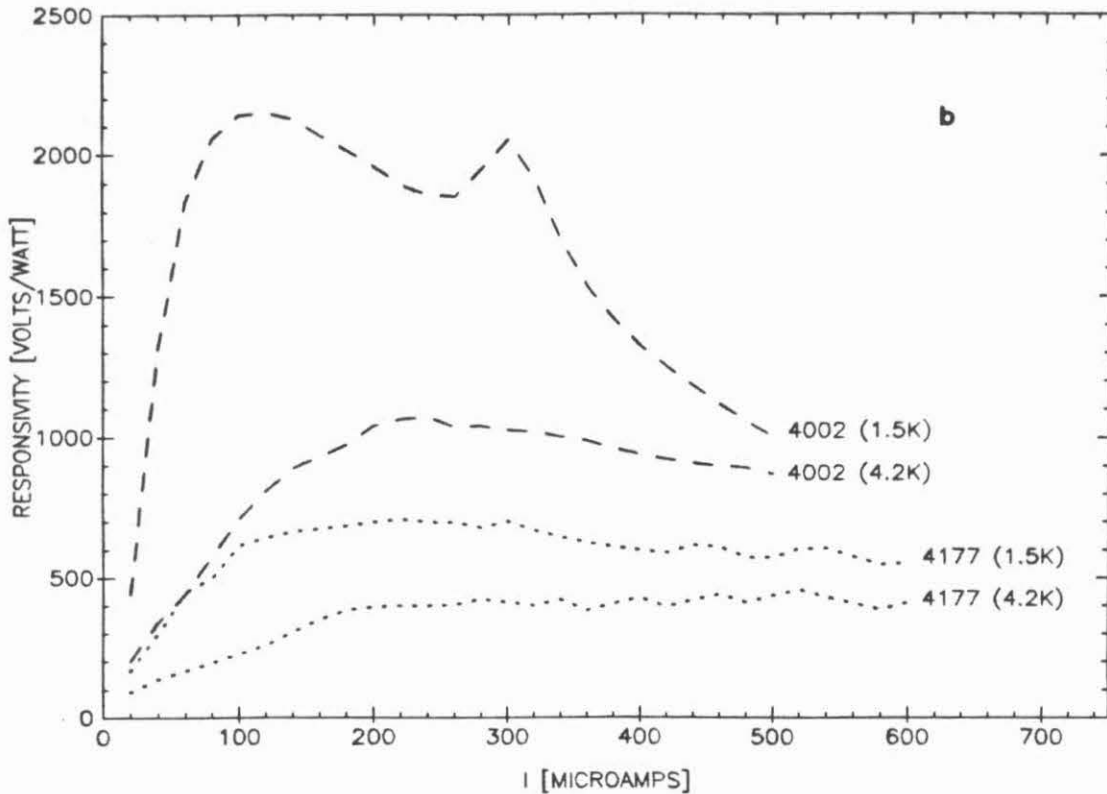


Fig. 2.4b: Ideal responsivity for two InSb samples at 1.5K and 4.2K.

Now recall that in Sec. 2.5, the experimental thermal conductance was found to be a slowly varying function of electron temperature. If we assume for the moment that it is temperature independent, then from Eqn. 2.12  $dP/dT_e = G$ . Furthermore, the derivative  $dR/dT_e$  can be evaluated using the empirical conductivity relation,  $\sigma = \sigma_0 [1 + (T_e/T_i)^2]$ . Thus we can evaluate Eqn. 2.15 as a function of bias current for any electron temperature. The results for the 4002 sample are shown in Fig. 2.5b. Notice that the theoretical curve doesn't show two peaks as does the curve based on the Eqn. 2.14. By inspection of Fig. 2.4a, we see that the peak at higher bias current reflects the negative dynamic



resistance region of the I-V curve. This negative resistance was only seen in the 4002 material below  $\sim 2\text{K}$  and did not appear in any of the other materials at any temperature tested.

The real advantage of using Eqn. 2.15 instead of Eqn. 2.12 is that it allows prediction of the ideal responsivity at temperatures where an I-V is not yet available. For example, if we make the same assumptions as above, the theoretical responsivity at  $0.3\text{K}$  can be calculated and is shown in Fig. 2.5. Notice that

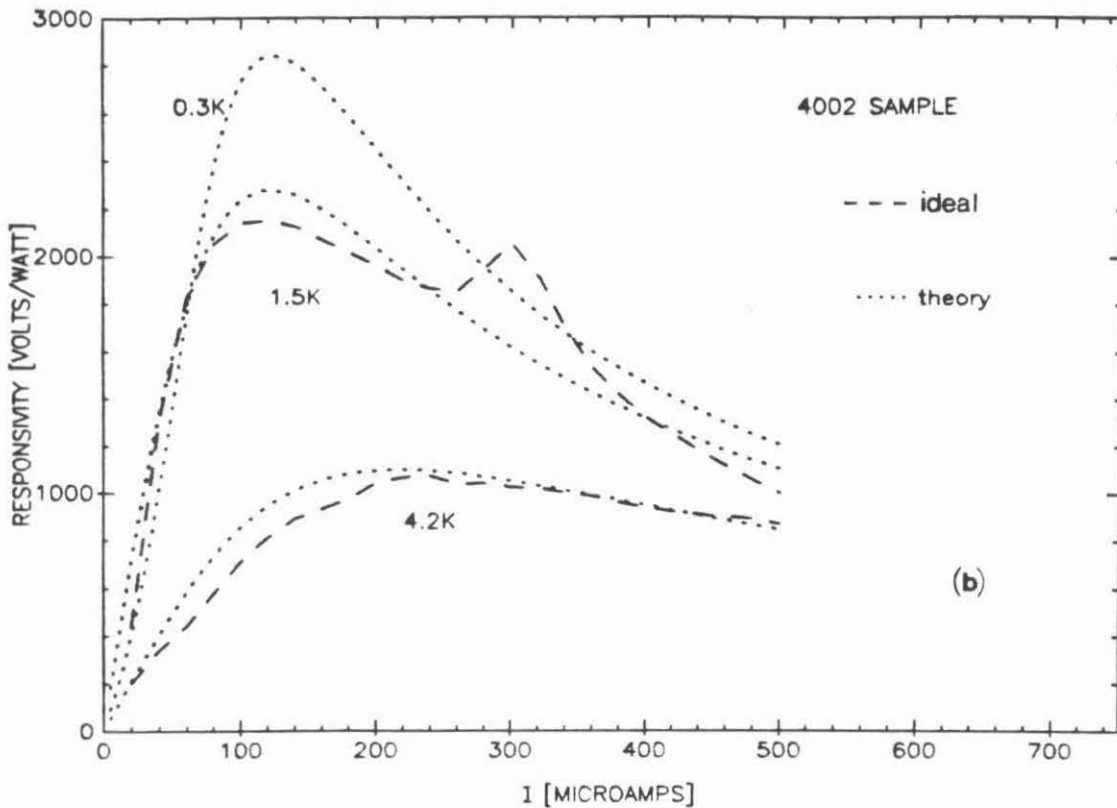


Fig. 2.5: Ideal and theoretical responsivity for the 4002 sample.

the predicted maximum at  $0.3\text{K}$  is only about 25% larger than the maximum at  $1.5\text{K}$ . This implies that it is probably not worth cooling the bolometer down to

0.3K since such a temperature can only be reached (e.g., using  $^3\text{He}$  systems) with much more effort than that expended to get to 1.5K.

Another important application of Eqn. 2.15 is in deriving what I call the geometrical theorem of bulk bolometers. The first step of the derivation is to re-write the quantity  $I^2 dR/dP$  as,

$$H = I^2 \frac{dR}{dP} = -\frac{p}{\sigma} \frac{d\sigma}{dp} \quad (2.16)$$

where  $p$  is the bias power absorbed per unit volume and  $\sigma$  is the DC conductivity. By inspection, we see that this quantity is intensive (i.e., doesn't scale with the volume). Next, assuming that the bias electric field is uniform, we can re-write Eqn. 2.15 as

$$r = -\left[ \frac{H}{1-H} \left( \frac{1}{\sigma p} \right)^{1/2} \right] \frac{1}{A} = \frac{\Theta}{A} \quad (2.17)$$

where  $A$  is the bias current cross section and  $\Theta$  is a new quantity I call the responsivity constant. Clearly  $\Theta$  is intensive and considered as a function of  $p$ , depends only on the given material and bath temperature. Therefore, if  $\Theta(p, T_b)$  has a maximum at some particular  $p$ , then *the open circuit responsivity of a detector made of that material will have a maximum that depends geometrically only on the current cross section.*

We saw in Fig. 2.4b and Fig. 2.5 that two different samples displayed maxima in the ideal responsivity at some bias current,  $I_{\max}$ . This result is typical: every InSb sample I tested showed a maximum in the ideal responsivity when operated at 4.2K or less. Therefore, the geometrical theorem is applicable. To demonstrate it, I show in Table 2.4 the responsivity parameters of three 4002 samples of vastly different geometry. The parameters  $I_{\max}$  and  $S_{\max}$  were measured directly from the I-V curves using Eqn. 2.14 and the current cross section was

measured using a micrometer or a microscope reticle. Notice that the values of  $\Theta$  are close, as they should be. The small difference is due, in part, to the fact that the 4002 wafer was not homogeneous. However, the three detectors were taken from close enough points in the wafer to preclude large differences in material parameters.

<b>Table 2.4</b>				
<b>Responsivity parameters of some 4002 samples at 4.2K</b>				
(symbols are defined in the text)				
Sample geometry	A [cm x cm]	$I_{max}$ [ $\mu$ A]	$S_{max}$ [KV/W]	$\Theta$ [V-cm <sup>2</sup> /W]
slab	.24x.035	210	1.1	9.2
bar detector	.035x.035	22	8.1	9.9
needle detector	.020x.020	9	21.5	8.9

Some interesting implications of the geometrical theorem are as follows. The maximum responsivity of a uniform bolometer operating at a particular bath temperature will not increase with length. However, it will be greatly enhanced by decreasing the detector bias cross section. This is the fact that explains the superior results that have been obtained with the waveguide mounted InSb hot electron bolometer [Phillips and Jefferts 1973]. In this configuration the detector is an inductive post which can be made very thin.

Many free space coupled detector schemes have been built over the years but have not performed nearly as well, mostly because the bolometer is then made wide in one transverse dimension and has relatively poor responsivity.

## 2.7 Absorption Coefficient of InSb in the Submillimeter Region

Despite the widespread detector applications, there exist surprisingly little experimental data regarding the submillimeter wave absorption properties of InSb. From his measurements of direct detector response spectra, Putley [1963] concluded that the absorption was Drudian. Vystavkin et al. [1968] determined the absorption from the transmission coefficient through slabs and found it to be distinctly non-Drudian. They found the absorption to exceed the Drudian prediction and to decrease with frequency faster than  $\omega^{-2}$ . More recently, Aren-darchuk et al. [1973] found that in material with low carrier concentration and high compensation, the absorption is consistent with the presence of distinct donor pairs or, equivalently, singly ionized hydrogen molecules. They deduced this from several peaks in the absorption spectrum below 300 GHz.

In the present section, the absorption coefficient is determined from the transmission through thin slabs in the range 10-40  $\text{cm}^{-1}$ . The results have formed the basis of a publication [Brown 1985a]. The instrument used was the Fourier transform spectrometer described in Appendix 3.

### 2.7.1 Theory of Absorption and Transmission Coefficients

A general expression for the optical absorption coefficient is [Jackson 1975],

$$\alpha(\nu) = \frac{4\pi\nu}{c} \left[ \frac{\mu\epsilon_r}{2} \left( \sqrt{1 + (\epsilon_i/\epsilon_r)^2} - 1 \right) \right]^{1/2} \quad (2.18)$$

where  $\epsilon_r$  is the real part of the dielectric function,  $\epsilon_i$  is the imaginary part and  $\mu$  is the magnetic permeability, assumed equal to 1 henceforth. In practice, the absorption coefficient of a material is often obtained from the experimental transmission through thin slabs. A theoretical expression relating these two quantities is [Born and Wolf 1975],

$$\tau_p(\nu, \vartheta) = \frac{t_p^2 \exp(-2y\eta)}{1 + \beta \tau_p^2 \exp(-4y\eta) - (1+\beta)\tau_p \cos(2\varphi + 2x\eta) \exp(-2y\eta)} \quad (2.19)$$

$$x = \left\{ \frac{1}{2} \left[ \epsilon_r - \sin^2 \vartheta + \sqrt{(\epsilon_r - \sin^2 \vartheta)^2 + \epsilon_i^2} \right] \right\}^{\frac{1}{2}} \quad (2.20)$$

$$y = \left\{ \frac{1}{2} \left[ \sin^2 \vartheta - \epsilon_r + \sqrt{(\epsilon_r - \sin^2 \vartheta)^2 + \epsilon_i^2} \right] \right\}^{\frac{1}{2}} \quad (2.21)$$

$$\tan \varphi = \frac{2y \cos \vartheta}{x^2 + y^2 - \cos^2 \vartheta} \quad (2.22)$$

where  $\tau_p(\nu, \vartheta)$  is the transmission coefficient for a plane wave incident and outgoing in vacuum at angle  $\vartheta$  with respect to the normal and having polarization denoted by  $p$ . The quantities  $\tau_p$  and  $t_p$  are the interface reflection and transmission coefficients, and  $\eta = 2\pi s \nu / c$  where  $s$  is the sample thickness. The parameter  $\beta$  ( $=-1 \rightarrow 1$ ) represents the quality of the slab:  $\beta=1$  corresponds to perfectly parallel faces and  $\beta=-1$  corresponds to wedged faces. Eqn. 2.19 is generally valid for any material, including metals, provided that plane waves propagate through the slab with negligible diffraction. This occurs, of course, when the wavelength is much smaller than the transverse dimension of the slab. Under these conditions, the mean transmission coefficient of an incident beam at frequency  $\nu$  is,

$$\tau(\nu) = \frac{\sum_p \int \tau_p(\nu, \vartheta) W_p(\Omega) \cos(\vartheta) d\Omega}{\sum_p \int W_p(\Omega) \cos(\vartheta) d\Omega} \quad (2.23)$$

where the sum is over polarization parallel and perpendicular to the plane of incidence.  $W_p(\Omega)$  is the angular weighting function for the incident beam, equal to 1 for isotropic radiation and random polarizations.

Inspection of Eqn. 2.19 shows that under the conditions,  $\epsilon_r = \text{constant}$ ,  $\epsilon_r \gg 1$  and  $\epsilon_r \gg \epsilon_i$ , the separation between successive maxima or minima of the transmission spectrum will be  $\Delta\nu \approx c / (2s\sqrt{\epsilon_r})$ . This approximation will remain accurate even when  $\epsilon_r$  is not constant provided that it varies little over the period of the fringes. This fact will be used below to determine  $\epsilon_r(\nu)$  of InSb in the millimeter wavelength region.

We can make a simple application of the above theory using the AC Drude model of metals [Ashcroft and Mermin 1975],

$$\epsilon_r = \epsilon_0 - \frac{4\pi n e^2}{m^*(\omega^2 + \gamma^2)} \quad (2.24)$$

$$\epsilon_i = \frac{4\pi n e^2 \gamma}{\omega m^*(\omega^2 + \gamma^2)} \quad (2.25)$$

where  $\epsilon_0$  is the contribution of the background lattice,  $n$  is the carrier concentration and  $\gamma$  is the momentum relaxation frequency. This is not to say that the Drude theory necessarily applies to the present experiment. On the contrary, the present experimental conditions always satisfy  $h\nu > kT$  so that one might expect the absorption process to be quantum mechanical [Jensen 1975]. The simplest relevant quantum theory of absorption is based on the process of inverse Bremsstrahlung: i.e., the electron residing in a continuum state of an ionized impurity center is photo-excited into a higher energy continuum state. The expression found to be most appropriate for this experiment is [Meyer 1958, Visvanathan 1960],

$$\alpha(\nu) = \frac{16\pi n_i Z^2 e^6 [1 - \exp(-\beta)]}{3m^* h c \nu^3 \epsilon_0^{5/2} \sqrt{2\pi m^* kT}} \quad (2.26)$$

where  $n_i$  is the ionized impurity density,  $Z$  is its charge,  $h$  is Planck's constant,  $k$  is Boltzmann's constant,  $T$  is the temperature of the material and  $\beta = h\nu/kT$ . This expression was derived using a low electron energy approximation due to Elwert [Bethe and Salpeter 1957] and predicts a significantly higher value of absorption than similar formulae based on the Born approximation.

### 2.7.2 Experiment

Two different slabs of n-type InSb material were prepared and tested. Both samples were cut with a wire saw out of wafers purchased from Cominco Inc. The samples were then mechanically lapped and chemically etched down to a thickness slightly less than 0.04 cm. Low resistance contacts were soldered on two opposing ends using sulfur-doped indium. The DC conductivity of these samples was studied in Sec. 2.4 and the impurity concentrations were presented for the 4177 and 4002 materials in Sec. 2.3. Displayed in Table 2.5 are the properties of these samples that are relevant to this section.

The Fourier transform spectrometer used for this experiment is described at length in Appendix C. In the present experiment, the spectral resolution is  $\delta\nu/c = .61 \text{ cm}^{-1}$ . Transmission coefficients are obtained by the substitution procedure. First a background spectrum is taken with an InSb bolometer. Then the InSb slab is placed directly in front of the detector and a second spectrum is recorded and then divided by the background spectrum. This ratio is, in principle, the transmission coefficient of Eqn. 2.23 with  $W_p = 1$ . In practice several techniques were found necessary to make the substitution procedure accurate. First, the reflections off the background detector had to be minimized to avoid standing waves between it and the slab. To accomplish this, the background detector had a small cross section compared to the exit aperture of the cone and was backed by Eccosorb. Second, it was important to filter out the incident

Table 2.5		
Size and material properties of the two InSb slabs tested		
Parameter	4177 sample	4002 sample
Dimensions (cm)	0.27x0.28 x0.038	0.20x0.24 x0.035
DC conductivity ( $1/\Omega\text{-cm}$ )	0.19 @ 2.2K 0.36 @ 4.2K 0.77 @ 7.5K	0.095 @ 2.2K 0.20 @ 4.2K 0.52 @ 7.5K
Real part dielectric function @ $10\text{-}40\text{ cm}^{-1}$ , $\epsilon_r = a - b\lambda$	a=18.8 b=59.8 $\text{cm}^{-1}$	a=18.5 b=42.0 $\text{cm}^{-1}$
Fermi velocity (cm/s)	$1.1 \times 10^7$	$8.3 \times 10^6$
Inter-impurity length, $(1/n_i)^{1/3}$	138 nm	135 nm

near-infrared radiation well enough so that the addition of the InSb slab did not alter the responsivity of the background detector. A 0.010 inch thick sheet of black polyethylene placed across the exit aperture was sufficient for this purpose.

To determine the absorption coefficient from the transmission spectrum, the following procedure was used. First the real part of the dielectric function was obtained from the separation of adjacent peaks in the spectrum. Because



the true position of the peaks could not be determined very accurately, this technique gave a rather crude estimate of  $\epsilon_r$ . However, it did indicate that for each of the samples tested  $\epsilon_r$  was a monotonically increasing function of wavenumber in the region  $10\text{-}40\text{ cm}^{-1}$ . With this fact in mind,  $\epsilon_r$  was then set equal to  $a\text{-}b\lambda$ . The two free parameters,  $a$  and  $b$ , were determined by graphically fitting Eqn. 2.23 to the entire transmission spectrum. This technique yielded a better estimate of  $\epsilon_r$ , particularly at the shorter wavelengths.

The next step in determining the absorption was the suppression of the oscillation in the experimental spectrum. This was accomplished by constructing two piecewise linear curves, one through the maxima of the spectrum and one through the minima. The arithmetic mean of these two curves was then equated to the theoretical transmission assuming  $\beta=-1$  in Eqn. 2.19. Using the known values of  $\epsilon_r(\nu)$ , the imaginary part of the dielectric function was then solved for numerically by iteration and the absorption was calculated using Eqn. 2.18. The accuracy of this procedure was tested on theoretical transmission spectra generated using the AC Drude model with material parameters identical to those of our InSb slabs and assuming  $\epsilon_0=17.88$ ,  $m^*=0.0139m_0$ , where  $m_0$  is the free electron mass. The uncertainty in  $\alpha$  was found to be less than 5%. The procedure is least accurate when  $\epsilon_r$  changes rapidly over a wavenumber region comparable to the period of oscillation. We do not expect any sharp structure in  $\epsilon_r$  over the  $\sim 3.5\text{ cm}^{-1}$  period of our sample transmission spectra.

For the samples tested, the most reproducible values of the absorption coefficient were obtained when  $\alpha \gtrsim 3\text{ cm}^{-1}$ . Below this value, the change in the background detector signal due to the insertion of the slabs was comparable to the uncertainty of the detector signal. In addition, after an experiment with a dummy quartz slab, it was decided that the data were only accurate above roughly  $10\text{ cm}^{-1}$ . The problem below this wavenumber is caused either by

diffraction associated with the slab or the effect of the diminishing density of radiation modes at frequencies near the waveguide cutoff. In either case, it is doubtful that Eqn. 2.19 accurately describes the observed transmission coefficient. The condensing cone has an exit aperture of .25 cm diameter which corresponds to a cutoff frequency of 69 GHz ( $2.3 \text{ cm}^{-1}$ ) for the  $TE_{11}$  mode of circular waveguide.

### 2.7.3 Absorption Results

Entered in Table 2.5 are the expressions for the real part of the dielectric function obtained for our samples at 4.2K. In the  $10\text{-}40 \text{ cm}^{-1}$  range, the value of  $\epsilon_r$  for the 4177 sample is slightly greater than that for the 4002 sample. This is consistent with the Drude model considering that the 4177 sample has greater carrier concentration.

Shown in Fig. 2.6a are the experimental absorption spectra for the samples at 4.2K. There are two obvious features of these spectra that might be familiar to workers in the millimeter wave region. First, the absorption decreases monotonically with frequency, the rate of decrease being greatest at the lowest wavenumbers. Second, the absorption in the 4177 sample exceeds that in the 4002 sample by a nearly constant factor across the band. This can be explained qualitatively, as for the values of  $\epsilon_r$ , by the greater carrier concentration of the 4177 material. An unexpected feature in the 4177 spectrum is the step-like structure around  $26 \text{ cm}^{-1}$ .

To see the effect of elevated electron gas temperature, we plot in Fig. 2.6b the absorption spectra of the 4177 sample at  $T_e = 2.2\text{K}, 4.2\text{K}, 7.5\text{K},$  and  $17.9\text{K}$ . The last two temperatures were attained by heating the electron gas with a DC bias while keeping the bath at 4.2K. The value of  $T_e$  for a given bias point, (I,V,R), is equal to the bath temperature,  $T_b$ , at which the zero bias resistance

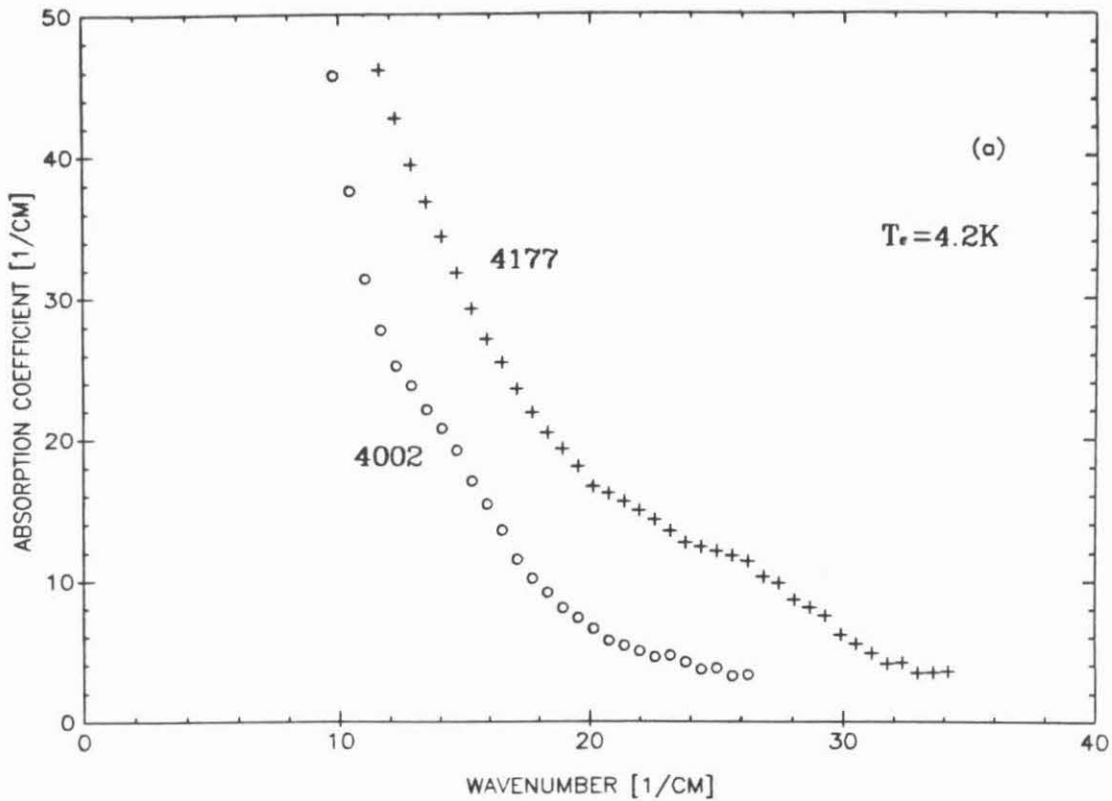


Fig. 2.6a: Experimental absorption spectrum at  $T_e = 4.2K$ : 4177 sample - +, 4002 sample - o.

has the value  $R$  [cf. Sec. 2.5]. We immediately see from Fig. 2.6b that the absorption coefficient at the lowest wavenumbers decreases with increasing  $T_e$  while the absorption at the high end is practically independent of temperature. The absorption spectrum of the 4002 sample was also measured at 2.2K. It was found to be almost exactly equal to the absorption at 4.2K and therefore is not shown here.

In Figures 2.7a and 2.7b we plot the predictions of the simple theories considered in this thesis. Using a value of  $\gamma$  obtained from the DC conductivity, the AC Drude theory gives rather poor agreement with the 2.2K data for the 4177

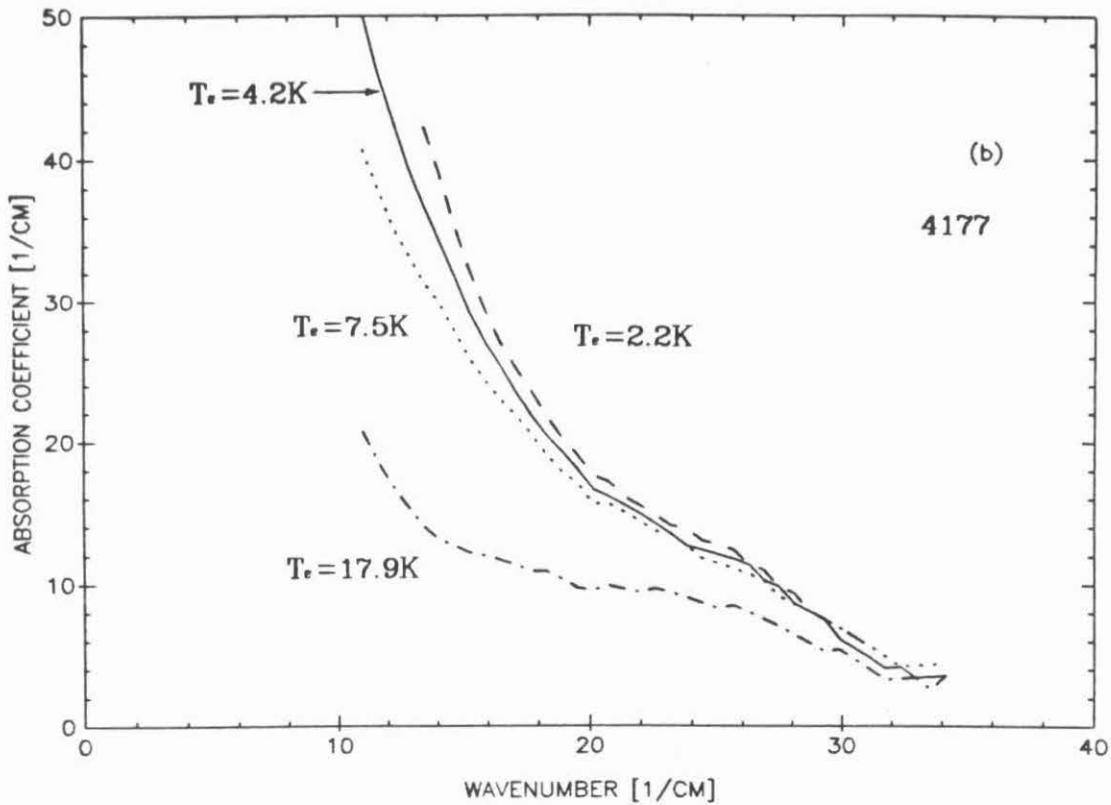


Figure 2.6b: Experimental absorption spectrum, 4177 sample:  $T_e = 2.2K$  - dashed,  $T_e = 4.2K$  - continuous,  $T_e = 7.5K$  - dotted,  $T_e = 17.9K$  -dash dotted.

sample and the 4.2K data of the 4002 sample. Specifically, it underestimates the absorption well below and overestimates it well above  $20 \text{ cm}^{-1}$ . In contrast, the quantum theory gives good agreement near the ends of the band but slightly underestimates the absorption in between.

In Figures 2.8a and 2.8b, the theoretical curves are compared to the experimental absorption of the 4177 sample at  $T_l = 4.2$  and biased to  $T_e = 7.5K$ . Notice that the prediction of the Drude theory improves greatly as the temperature is increased. At  $T_e = 7.5K$ , the Drude theory yields good agreement with experiment. In comparison, the prediction of the quantum theory gets slightly worse

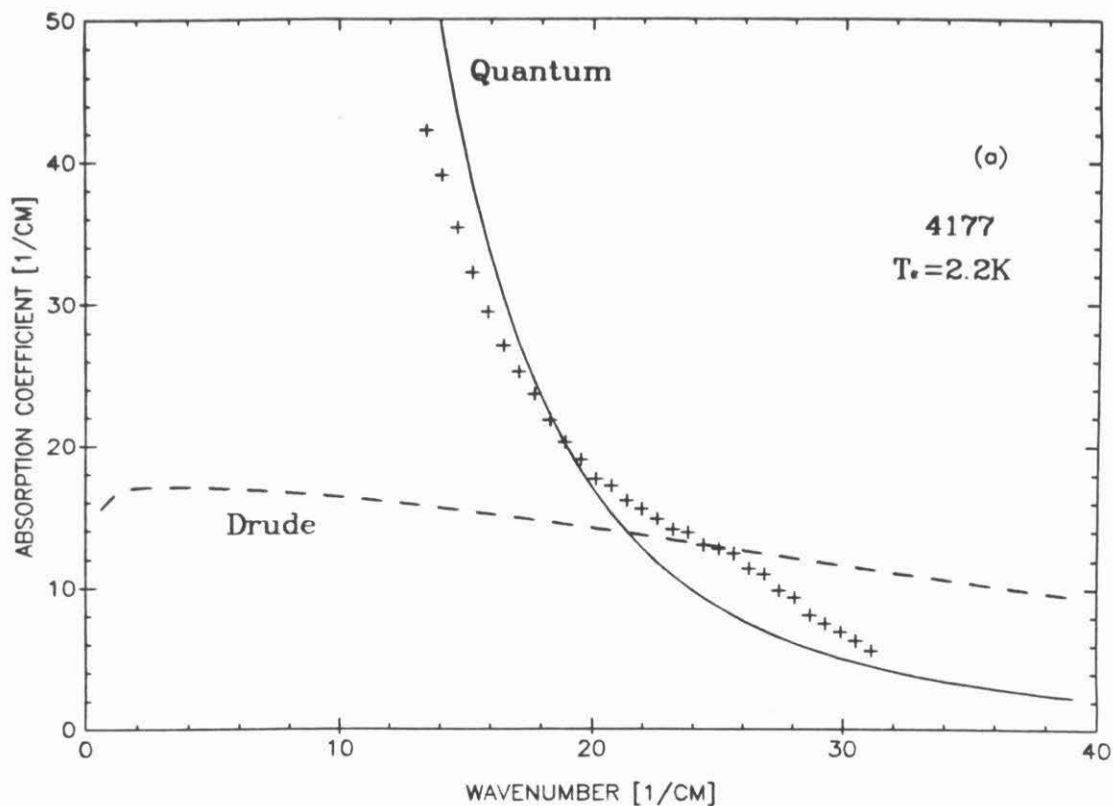


Fig. 2.7a: Absorption spectra for 4177 sample at 2.2K: experiment - +, AC Drude theory - dashed, quantum theory - continuous.

as the temperature increases. At  $T_e = 7.5K$ , it underestimates the absorption over most of the band.

#### 2.7.4 Discussion

The results presented in this paper help explain certain key aspects of the performance of InSb hot electron bolometers. In particular, it is now clear why the device performance improves so much as the bath temperature is decreased in the liquid helium range. Part of the reason is the non-Druidian absorption displayed by InSb. With a reduction in bath temperature, the DC

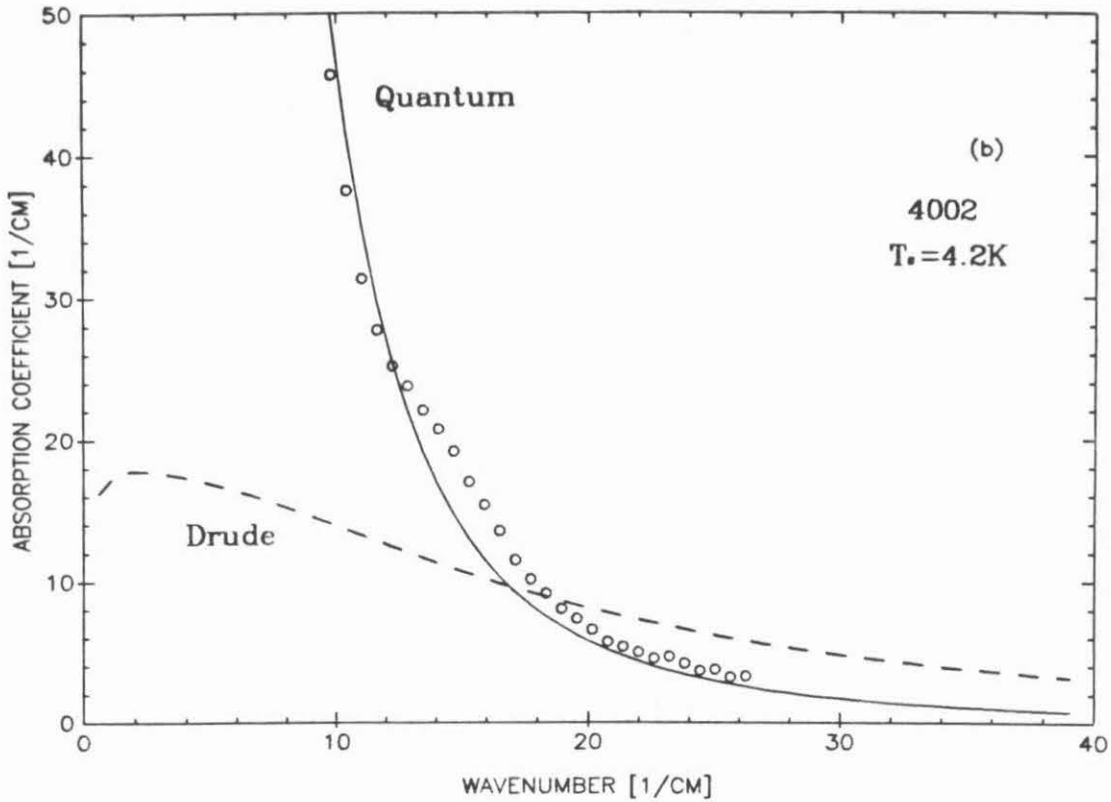


Fig. 2.7b: Absorption spectra for 4002 sample at 4.2K: experiment - o, AC Drude theory - dashed, quantum theory - continuous.

resistance and related responsivity both increase significantly while the submillimeter absorption changes very little. In fact, over most of the spectrum studied, the absorption actually increases with decreasing temperature. Notice by comparing Fig. 2.7a and 2.8a that if the absorption was Drudian then the value of  $\alpha$  at  $16 \text{ cm}^{-1}$  would decrease by a factor of about 1.5 between  $T_e = 4.2\text{K}$  and  $T_e = 2.2\text{K}$  (these are the approximate electron gas temperatures at the optimum bolometer bias with the bath at 3.3K and 1.2K, respectively). This would oppose the increase in responsivity and lead to little or no improvement of performance at the reduced temperature.

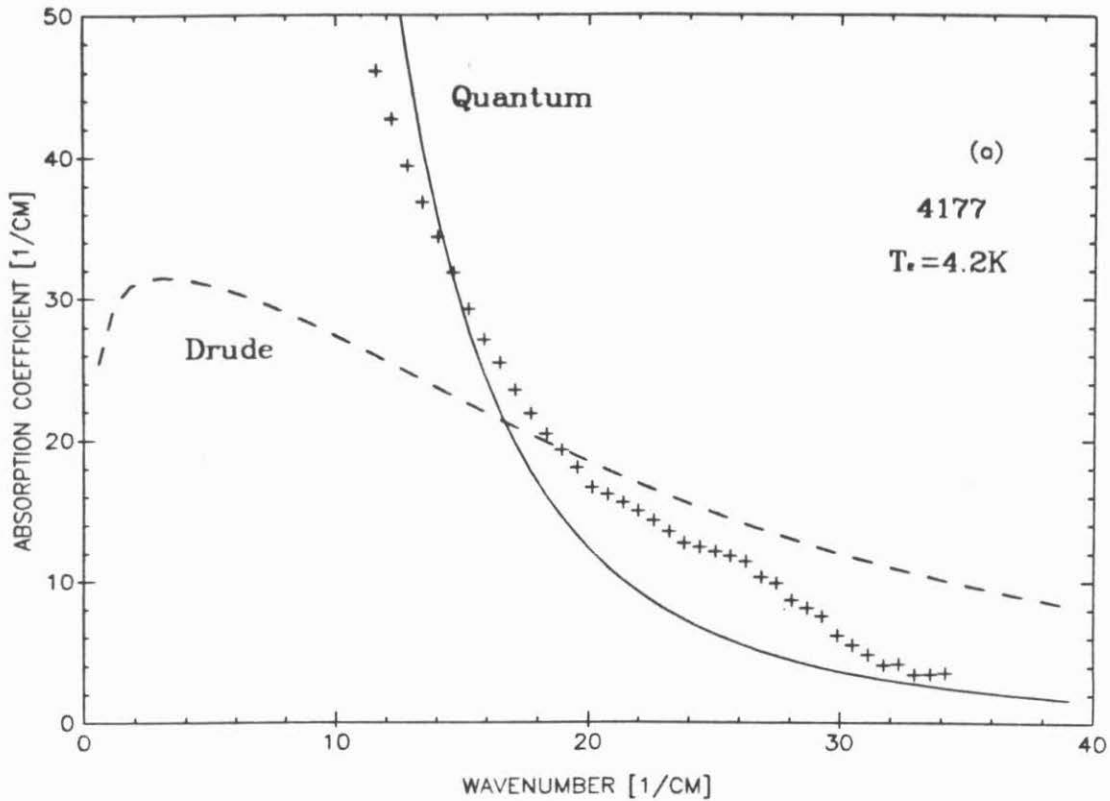


Fig. 2.8a: Absorption spectra of 4177 sample at  $T_e = 4.2K$ : experiment - +, Ac Drude theory - dashed, quantum theory - continuous.

A second aspect of bolometer performance that our results begin to explain is the dependence of absorption on material properties. In particular, the promising agreement between experiment and the quantum theory (Eqn. 2.26) suggests that the absorption coefficient may depend simply on the product of the carrier concentration and the the total ionized impurity concentration. From Table 2.1 we see that the two samples tested differ primarily in carrier concentration. Therefore, before any conclusions are drawn, it would be wise to test a third material with much different total impurity concentration and similar carrier concentration to our samples. Material with much higher carrier

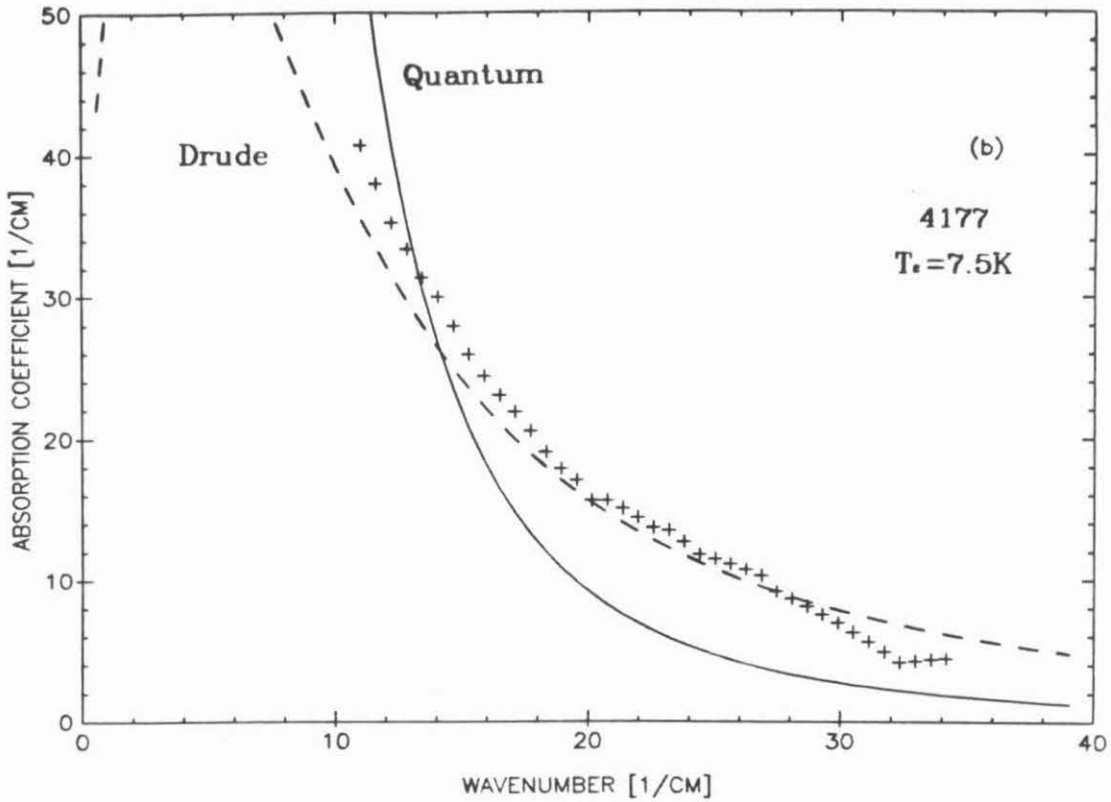


Fig. 2.8b: Absorption spectra of 4177 sample at  $T_e = 7.5K$ : experiment - +, AC Drude theory - dashed, quantum theory - continuous.

concentration would not be particularly interesting since it would be more metallic (i.e., DC resistivity less dependent on temperature) and more likely described well by Drude theory.

Finally, it should be mentioned that the quantum theory of absorption used in this paper is valid only for  $\omega\tau \gg 1$ , where  $\tau$  is the effective collision time. This condition is due, at least in part, to short time limitations on Fermi's golden rule of perturbation theory [Cohen-Tannoudji et al. 1977]. Although the value of  $\tau$  in our samples is uncertain and might depend on frequency in a complicated way, a rough approximation should be  $\tau \sim l/v_f$  where  $l$  is the mean inter-impurity



distance and  $v_f$  is the Fermi velocity. For the 4177 sample, this approximation yields  $\tau \approx 1.25 \times 10^{-12}$  s and thus  $1/\lambda \gg 4.2 \text{ cm}^{-1}$  is the applicable range of the quantum theory. Another potential limitation is that the Bremsstrahlung analysis is done only for electronic scattering from a Coulomb center of opposite charge. In other words, Eqn. 2.26 is correct only for ionized donors. The contribution to absorption should be somewhat less for acceptors than for donors because the electron is drawn closer to and hence scattered more from the positively charged donors.

### 3. Rollin Mode Detector Studies

#### 3.0 Introduction

For about the first half of my graduate studies, I spent a great deal of time working with the Rollin mode bolometer. The heterodyne detector geometry had already been optimized by Phillips and Jefferts [1973]. In addition, an optimum material had been found and a mixer made of this material was already gathering astronomical data up to about 500 GHz. It was my task to improve the detector performance by obtaining or producing, in some way, better material. Of particular concern was improving the detector bandwidth. Therefore, I purchased some new InSb wafers from Cominco Inc. and began learning to make and test waveguide mounted mixers. Some heterodyne tests were conducted above 600 GHz using a JPL carcinotron as a local oscillator. No conclusive results were obtained from these tests, primarily due to serious problems with the carcinotron. Lacking any other viable local oscillator scheme for the 600+ GHz region, I therefore elected to study InSb bolometers experimentally in direct detection. In a parallel effort, I investigated the theory of heterodyne performance.

In this chapter, I first present the results of the direct detection studies. Of particular interest is the comparison of different InSb materials. I then present the results of the experimental noise measurements. In the last section, I will present the results of the theoretical heterodyne study. This study was made possible by much of the experimental data acquired during the thesis work. I believe it supersedes any previous analysis of the heterodyne bolometer.

### 3.1 Experimental Absolute Response

In this section, I compare the spectral response of three different InSb hot electron bolometers. We saw in the previous chapter that the optimum hot electron bolometer geometry is that which minimizes the bias cross section. Therefore, the detectors made for the present study are all long thin bars. The dimensions of the detectors are nearly identical. The only difference between them is the material type. One of the detectors was made from the optimum 4002 material. The other two were made from the 4190 and 4177 wafers purchased especially for this research. The precise dimensions and other important properties are summarized in Table 3.1.

The absolute spectral response was measured with a Fourier transform spectrometer (FTS). The spectrometer consists of a RIIC 720 Michelson interferometer, a light pipe and condensing cone assembly to couple the radiation down into a liquid helium cryostat, signal processing electronics, a minicomputer, and a graphics terminal. The spectrometer design and signal processing technique are discussed at length in Appendix C. Detectors are mounted across the exit aperture of the condensing cone. Absolute calibration of detector response spectra was accomplished with the following procedure. First a spectrum was obtained from a Golay cell (Pye-Unicam) mounted at the bottom of the cone in the same position as the detectors of interest. This particular Golay cell has a wedged diamond window that makes its overall spectral response very flat in the far-infrared. I then obtained a low wavenumber spectrum using the 4002 slab sample as a detector. It was calibrated by separate measurement of its absorption, dielectric constant (cf. Sec. 2.7) and ideal responsivity (volts/watt *absorbed*). Using this data, the Golay spectrum was scaled to be the absolute power spectrum at the bottom of the cone. All of the test detector results were then divided by the correctly scaled Golay spectrum.

Shown in Fig. 3.1a are the absolute spectral responses for the three detectors. The response for all three rapidly rolls off to about  $25 \text{ cm}^{-1}$ . Above this wavenumber, the rolloff is much more gradual. Shown in Fig. 3.1b are the theoretical absolute responsivity spectra for the 4002 and 4177 detectors.

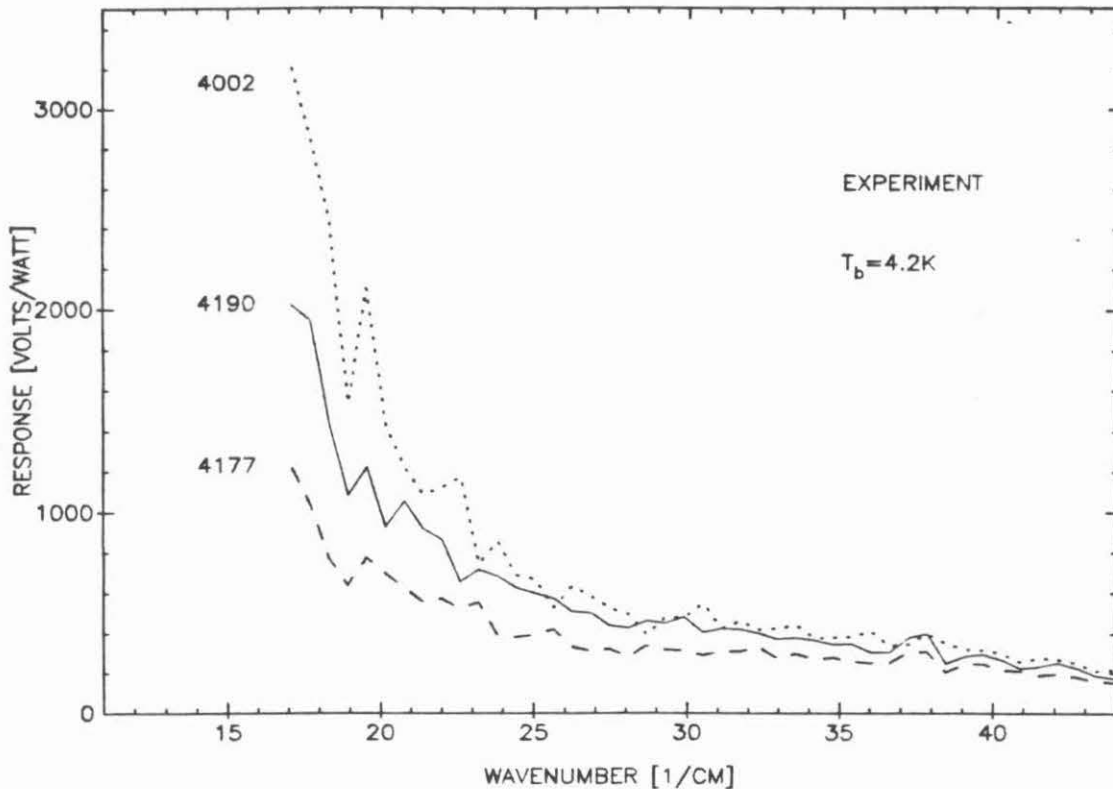


Fig. 3.1a: Experimental absolute response for three InSb detectors of identical geometry but different material.

Each theoretical spectrum is the product of the ideal bolometric responsivity and the coupling efficiency spectrum for the individual detector. The coupling efficiency at any wavenumber,  $\eta$ , is the fraction of incident power that is usefully absorbed. It is determined numerically using a special computer program. The only required information for the program is the experimental absorption

<b>Table 3.1</b>			
<b>Properties of the three detectors tested</b>			
Detector	1	2	3
Material	4002	4177	4190
Dimensions (cm)	.24x.036 x.036	.24x.033 x.033	.24x.038 x.038
Bias current ( $\mu A$ ), $I_B$	20 @ 4.2K 12 @ 2.2K	30	20
Resistance, R ( $K\Omega$ ), $I=I_B, B=0$ KG	1.05 @ 4.2K 2.42 @ 2.2K	0.64	1.12
Dynamic resistance, Z ( $K\Omega$ ), $I=I_B, B=0$ KG	.71 @ 4.2K 1.53 @ 2.2K	0.49	0.75
Ideal responsivity (KV/W) $r = \frac{R-Z}{2RI}, I=I_B$	8.1 @ 4.2K 15.3 @ 2.2K	3.9	8.3
Experimental response, (KV/Watt), $I=I_B, B=0$ KG, $\sigma = 17 \text{ cm}^{-1}$	3.2 @ 4.2K 3.8 @ 2.2K	1.2	2.1

coefficient spectrum given in Sec 2.7 and the dimensions of the detector. The fact that the experimental response is much less than the theoretical response,

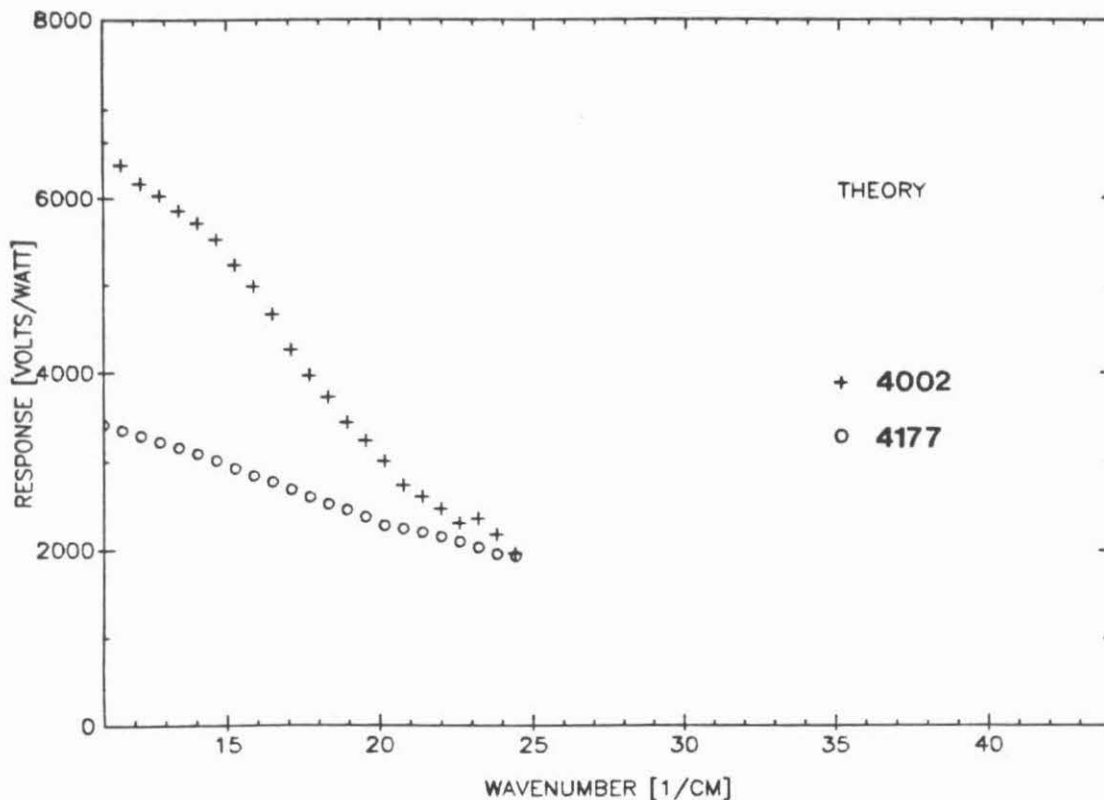


Fig. 3.1b: Theoretical responsivity for the 4002 and 4177 detectors.

even at the low frequency end, is explained by the small area of the detectors compared to the exit aperture of the condensing cone. Recall that the calibration detector was a slab sample that filled the exit aperture.

There are two aspects of the experimental response spectra that deserve further attention. First, notice that the response of the 4002 detector exceeds that of the other two at the low end of the band. This is concrete evidence that the 4177 and 4190 materials are inferior. Second, notice that the 4002 response appears to roll off much faster than the 4177 response. This is consistent with the fact that the absorption coefficient rolls off faster in the 4002 material than

it does in the 4177 material (cf. Sec 2.7).

Finally, notice that the response of all three detectors practically levels off above roughly  $30 \text{ cm}^{-1}$ . This implies that the absorption coefficient also levels off in that region and is consistent with the experimental performance observed by others [G. Blake private communication]. This behavior is contrary to the prediction of both the Drude and inverse-Bremsstrahlung theories of absorption and deserves further study. Recall that the samples that I studied in Sec. 2.7 were too thin to obtain good data at high wavenumbers.

### 3.2 Noise of the Hot Electron Bolometer

In this section I present the experimental noise spectra of a hot electron bolometer and compare them to theory. The results have formed the basis of a publication [Brown 1984]. Until very recently, the noise generated by non-ohmic InSb was never described very accurately. Most workers claimed that the observed noise in the absence of background radiation was some combination of phonon noise and Johnson noise [Kinch and Rollin 1963, Putley 1964]. The usual semiconductor g-r noise is insignificant in InSb at liquid helium temperatures because the conduction electrons have a negligible probability of recombining with holes and zero probability of recombining with ionized donors. In the bolometer sample studied here, shot noise is insignificant because the contacts are alloyed with sulfur doped indium and do not form p-n or Schottky barrier diodes.

### 3.2.1 Bolometer Noise Theory

High quality bolometers usually have two significant noise mechanisms. Phonon noise is fluctuations in the power flow between the bolometric medium and the bath due to phonon population fluctuations. In general, the phonons of concern are those in the bolometer, in the thermal link to the bath and in the bath itself. The general theory is fairly complicated and is presented by Mather [1982]. In this section, I will be concerned only with the hot electron bolometer. For this device, the bolometric medium is the electron gas, the bath is the lattice and the thermal link is the electron-phonon interactions. The approximate expression for the power spectral density is [Putley 1964],

$$S_p(f) = 4kT_b^2 K \quad (3.1)$$

where  $k$  is Boltzmann's constant and  $K$  is the dynamic thermal conductance (see Sec. 3.3 for definition). The relevant temperature here is  $T_b$  because the bath is the only source of phonons.

The second important source of noise in bolometers is Johnson or thermal noise. This is fluctuations in the local electric field (and thus the voltage across the entire sample) due to electron velocity or momentum fluctuations. Under conditions of zero bias, the Johnson noise spectral density is the familiar equilibrium result,

$$S_j(f) = 4kT_b R. \quad (3.2)$$

Under biased conditions, the Johnson noise in high-quality bolometers is not described correctly by most non-equilibrium theories. For example, the generalized Nyquist expression for spectral density,  $4kT \operatorname{Re} Z(\omega)$  is obviously wrong because the real part of the bolometer dynamic impedance can be negative. The non-equilibrium theory that has been used most often in the past is simply



the equilibrium Johnson noise expression with the temperature being that of the bolometric medium,

$$S_j(f) = 4kT_e R = \overline{e_j^2} / \Delta f. \quad (3.3)$$

Surprisingly, this expression overestimates the total observed noise in high-quality InSb hot electron bolometers by as much as a factor of 2.

In a recent paper concerning bolometer noise, Mather provided the first correct explanation of the non-equilibrium Johnson noise [Mather 1982]. To understand this effect, we must first realize that the power flow between the bias supply and the bolometer fluctuates due the thermal or "open-circuit" Johnson noise in the bolometer. As emphasized by Mather, the rms value of this power flow is detected by the bolometer like any other absorbed power. This generates a noise voltage across the bolometer that adds coherently to the open-circuit noise voltage. If the bolometer is a negative type (i.e.,  $dR/dP < 0$ ), the added voltage at low frequencies will be 180 degrees out of phase with the open-circuit voltage. To calculate the exact magnitude of this effect, let's assume that a measurement of the narrow band, rms noise voltage is made at a frequency which is much less than the bolometer bandwidth. The total noise voltage measured across the negative bolometer will then be,

$$V_j = e_j - r \cdot P_B \quad (3.4)$$

where  $r$  is the ideal bolometric responsivity given by Eqn. 2.14 and  $P_B$  is the instantaneous power flow between the bias supply and the electron gas caused by the "open-loop" Johnson noise voltage. Since the bolometric medium is self-thermalized, this open-circuit noise voltage is simply  $e_j$  in Eqn. 3.3. The instantaneous power flow is fully correlated with  $e_j$  so that if we assume constant current bias conditions,  $P_B = I \cdot e_j$ . Therefore,

$$V_j = e_j (1 - r \cdot I). \tag{3.5}$$

For a high-quality InSb hot electron bolometer,  $r$  can be a large fraction of  $1/I$  in magnitude. The measured noise will then be significantly less than the "open-loop" value.

### 3.2.2 Noise Experiment

To test the above theory with satisfactory precision, it is necessary to have a circuit model incorporating both the bolometer and amplifier noise mechanisms. This model, shown in Fig. 3.2, consists of the bolometer equivalent circuit of Jones [1953] with equilibrium Johnson noise source in series and the source,  $-e_j/2$ , placed in the signal generator position. The latter source represents the

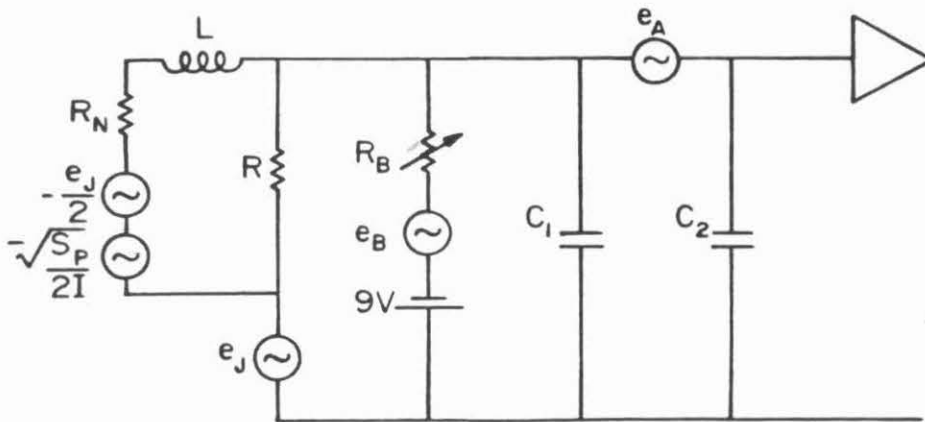


Figure 3.2: Noise equivalent circuit for InSb bolometer coupled to an FET preamp. This circuit includes generators for Johnson, phonon, amplifier and bias resistor noise contributions. Symbols are defined in the text.

fluctuations in the power flow between bias supply and electron gas. This power flow and the power due to phonon fluctuations are both detected by the bolometer as any signal would be.

The passive elements of the noise model are defined in terms of experimentally measurable quantities

$$R_N = \frac{RZ}{R - Z} \quad (3.6)$$

$$L = \frac{\tau}{2} R \left( \frac{R + Z}{R - Z} \right) \quad (3.7)$$

$$\tau = \tau_r \left( \frac{2R}{Z + R} \right) \left( \frac{Z + Z_L}{R + Z_L} \right) \quad (3.8)$$

The time constants  $\tau$  and  $\tau_r$  are discussed in Sec. 3.3. The quantity  $Z_L$  is the load impedance. Up to this point, the load impedance has been assumed to be infinite. The preamp used for the power spectrum measurements consists of two parallel 2N6550 Si JFETs in the common source configuration. It has an input impedance at the frequencies of interest (>200 kHz) represented by the capacitor,  $C_T$ . The load impedance is thus the parallel combination of  $C_T$  and the bias resistor,  $R_B$ . Since  $R_B$  is very large for constant current bias, the load impedance is almost purely capacitive. This complicates the analysis and is an unavoidable consequence of using a high-impedance, room temperature operated amplifier which generates less voltage noise than the InSb bolometer.

Other than the bolometer, the most significant source of noise is the preamp. A physical model of JFET noise includes a voltage generator for channel thermal noise, a shunt current generator representing gate noise, and a correlation between the two [Robinson 1974]. These generators are

placed after the amplifier input impedance. Note that the model in Fig. 3.2 has only the voltage generator. This generator alone dominates the total amplifier noise contribution for source resistances less than 5 kΩ and frequencies less than about 1 MHz: conditions always maintained in the present experiment. The voltage spectral density is

$$S_A(f) = 4k T_A R_A = \overline{e_A^2} / \Delta f \quad (3.9)$$

where  $R_A$  is the noise resistance and  $T_A$  is the ambient temperature. Also note that the model in Fig 3.2 has a shunt capacitance,  $C_2$  placed after  $e_A$ . This represents the effect of feedback on the channel thermal noise. The feedback occurs through the parasitic gate-drain capacitance and is more commonly known as the Miller effect.

The least significant source of noise is the bias circuit. The bias resistor contributes thermal noise,

$$S_B(f) = 4k T_A R_B \quad (3.10)$$

while the bias battery is assumed quiet. We can now write the total theoretical voltage spectral density at the preamp input as the incoherent sum of bolometer, amplifier and bias resistor components:


$$S_T(f) = \frac{\overset{\text{phonon noise}}{\downarrow} S_P R^2 / 4I^2 + \overset{\text{Johnson}}{\downarrow} S_j \left[ \left( \frac{R}{2} + R_N \right)^2 + (\omega L)^2 \right] + t_A + t_B}{(R + R_N - \omega^2 RLC_T)^2 + (\omega L + \omega R R_N C)^2} \quad (3.11)$$

$$t_A = S_A \left[ (R + R_N - \omega^2 RLC_1)^2 + (\omega L + \omega R R_N C_1)^2 \right] \quad (3.12)$$

$$\overset{\text{preamp noise}}{\uparrow} t_B = \frac{S_B}{R_B^2} \left[ (R R_N)^2 + (\omega R L)^2 \right] \quad (3.13)$$

where  $C_T = C_1 + C_2$  and it was assumed  $\omega R_B C_T \gg 1$  and  $R_B \gg R$ . Eqn. 3.11

describes a resonant circuit consisting of an inductive bolometer shunted by a capacitive amplifier. Part of the experimental work was to measure all the parameters in this equation so that an accurate calculation could be made of the non-equilibrium noise model.



The second portion of the experimental work involved measuring the sample noise spectrum directly. Two features of InSb made this task unusually straightforward compared to typical bolometer experiments. First, because of the relatively small time constant,  $\tau \sim 2 \times 10^{-7}$  sec., we could measure the noise over a wide bandwidth, but well above the  $1/f$  regime of the sample and all the electronics. Second, the resistance of our sample,  $R > 1k \Omega$ , is high enough that the Johnson noise dominates the noise of our preamp. In short, the InSb hot electron bolometer provides an excellent test of non-equilibrium Johnson noise theory.

The InSb bolometer used in this experiment was made out of the 4002 material. It has dimensions approximately .115 cm long  $\times$  .016 cm diameter and is mounted across a 1 mm diameter circular waveguide which is attached to the cold plate of a LHe cryostat (Fig. 3.3). The only coupling to outside radiation is through a feed horn of full angle  $7.6^\circ$ . This horn combined with two cooled black polyethylene filters limit the background radiation to a negligible amount in the millimeter region. The sample V-I characteristic under these conditions is shown in Fig. 3.4. The dynamic resistance was calculated directly from the V-I curve.

The elevated electron gas temperature at various bias currents was determined from the  $R$  vs  $T_e$  data using the same technique used in Sec 1.4. The observed time constant was determined with the bolometer connected to a broadband  $50\Omega$  amplifier. The output voltage of the amplifier was measured as a function of frequency of sinusoidally amplitude

modulated klystron power incident on the bolometer. This frequency dependence gives the bolometer time constant,  $\tau_T$ . The klystron power absorbed by the crystal was small enough to heat the electron gas insignificantly. The energy relaxation time was then calculated from Eqn. 3.8 and the values obtained, along with values of  $R$ ,  $Z$ ,  $T_e$ ,  $dR/dT_e$  and  $K$  are shown in Table 3.2.

**Table 3.2**  
**Parameters determined for non-equilibrium noise analysis**

$I(\mu A)$	$R(K\Omega)$	$Z(\Omega)$	$T_e(K)$	$\frac{dR}{dT_e}(\Omega/K)$	$K(\times 10^{-8}W/K)$	$\tau(\times 10^{-7}s)$
8	2.94	750	7.7	-740	8.0	2.5
16	1.69	350	10.6	-300	11.7	2.3
32	1.02	375	14.5	-100	22.1	1.2

△ Noise spectra are measured using the setup shown in Fig. 3.3. The bolometer noise power is first amplified and then down converted to an I.F. centered at zero with 40 kHz bandwidth. The noise is then square law detected, averaged with a time constant of .2 seconds and plotted against center frequency. Calibration is performed with by recording a spectrum with the bolometer shorted out. This spectrum is practically flat and is assigned the value of Eqn. 3.9 once  $R_A$  is determined.

The amplifier elements are determined as follows. The value of  $R_A$  is determined by a Y-factor method using a 50  $\Omega$  source resistor at 295 and 77K. By

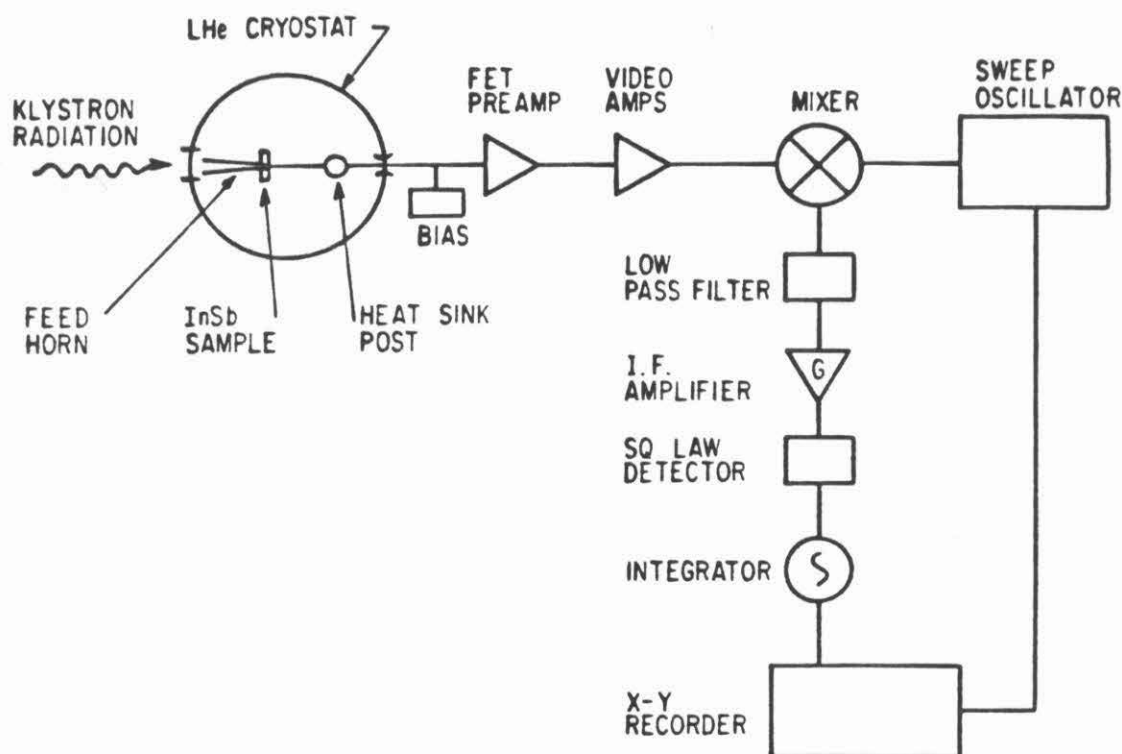


Figure 3.3: Block diagram of liquid helium cryostat, radiation coupling scheme and noise measurement electronics.

defining  $Y$  as the ratio of the 200 KHz spectral densities, we calculate  $R_A \approx 12\Omega$ . The total input capacitance is found by fitting the spectrum obtained with a room temperature  $1\text{ k}\Omega$  resistor at the input. Under this condition we can effectively ignore  $e_A$ , leading to  $C_T \approx 190\text{ pF}$ . Finally, the values of  $C_1$  and  $C_2$  are found using the amplifier noise model to fit the spectrum obtained with a  $4.2\text{K}$   $1.0\text{ k}\Omega$  resistor. We find  $C_1 \approx 120\text{ pF}$  and  $C_2 \approx 70\text{ pF}$ .

The experimental noise spectra for three bias currents are shown in Fig. 3.5. Also plotted are some theoretical values according to Eqn. 3.11. The peak in each spectrum reflects the resonant nature of the circuit. The agreement

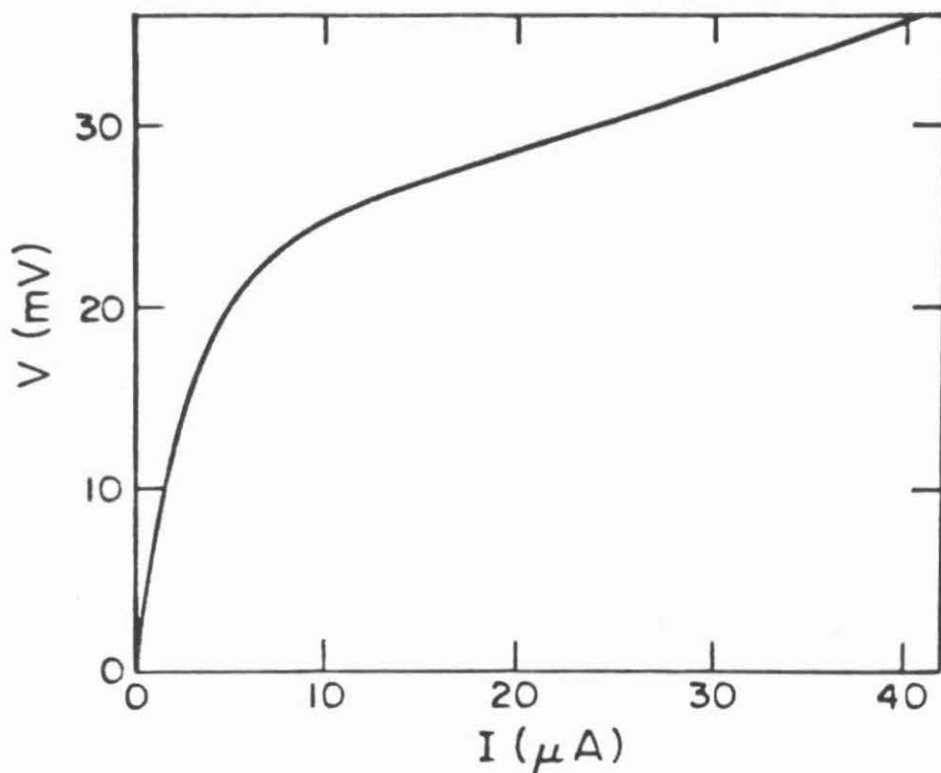


Figure 3.4: I-V characteristic of InSb bolometer at 4.2 K.

between theory and experiment is best at the lowest bias current,  $8 \mu\text{A}$ . In this case the difference is less than 6% across the band. At most points of the spectrum, the agreement is excellent. For  $16 \mu\text{A}$  bias, the agreement is not as good, a difference of about 10% occurring in the region of the peak. For  $32 \mu\text{A}$  bias, the theoretical prediction exceeds the experimental spectrum by nearly 12% at the peak frequency.

The theoretical prediction without the feedback effect of the bias supply is obtained by neglecting the generator  $-e_j/2$ . The results, shown in Fig. 3.5, overestimate the observed noise level by a large factor at most frequencies. The



difference between the two theories is greatest below the responsivity rolloff,  $f_c = 1/(2\pi\tau)$ . For  $f \gg f_c$ , the theories converge since the sample behaves like a normal resistor in both signal response and noise. Also the difference depends on the degree of nonlinearity at the bias point. For a sample biased to a point where  $Z=0$ , the low frequency Johnson noise power should be reduced by a factor of 4. As mentioned by Mather even greater reductions are possible for  $Z < 0$ , a condition found in certain InSb samples with bath temperatures  $T_1 < 2.0\text{K}$ .

To see the magnitude of theoretical phonon noise, values of Eqn. 3.11 excluding the generator  $-S_p/2I$  are also plotted in Fig. 3.5. The phonon noise contribution is obviously less than the Johnson noise at all frequencies and it decreases with bias current. For the largest current used,  $32 \mu\text{A}$ , the phonon noise is negligible and is not subtracted from  $S_T(f)$  in Fig. 3.5c.

The bias resistor component is the least significant of all. Like the other bolometer noise components, its spectrum displays a peak that shifts to higher frequencies and diminishes in magnitude with increasing bias current. The ratio of bias resistor noise to total noise is  $< 6\%$  in Fig. 3.5a,  $< 5\%$  in Fig. 3.5b and  $< 3\%$  in Fig. 3.5c.

In conclusion, the experimental noise spectrum of liquid helium cooled InSb is described quite accurately using a bolometric model that includes non-equilibrium Johnson noise and phonon noise. The model predicts a noise level less than equilibrium Johnson noise and explains, in part, the success of InSb as a highly sensitive millimeter wave detector. The same description should apply to the cryogenic Johnson noise of many other semiconductors. For example, certain high purity samples of Ge, GaAs, and HgCdTe display non-linearity due to hot carrier effects.

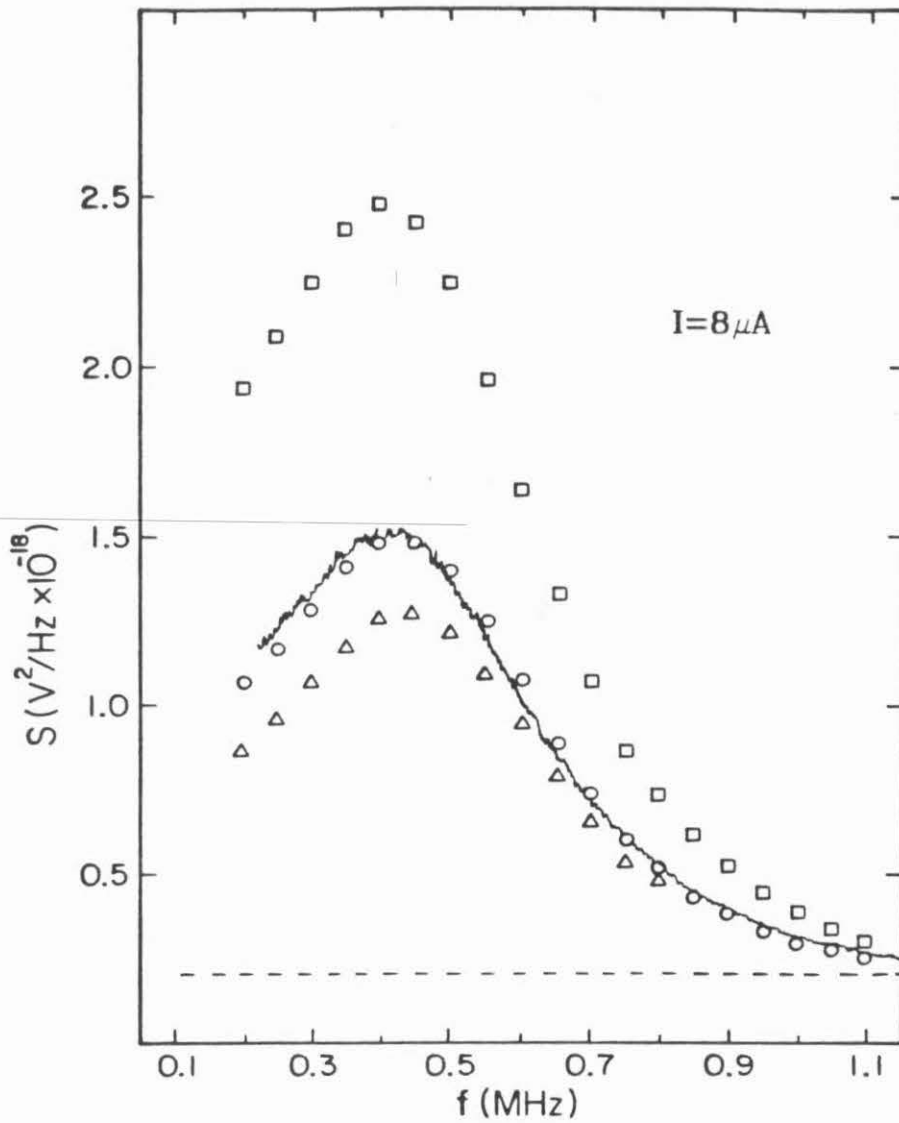


Figure 3.5a: Experimental and theoretical noise spectra for a bias current of  $I = 8 \mu A$ . Dashed curve is the preamp noise. Experimental spectra are continuous. Theoretical values are denoted as:  $\circ$ -total noise according to Eqn. 3.11,  $\square$ -total noise without correction for electrothermal feedback of Johnson noise,  $\triangle$ -total minus Phonon noise.

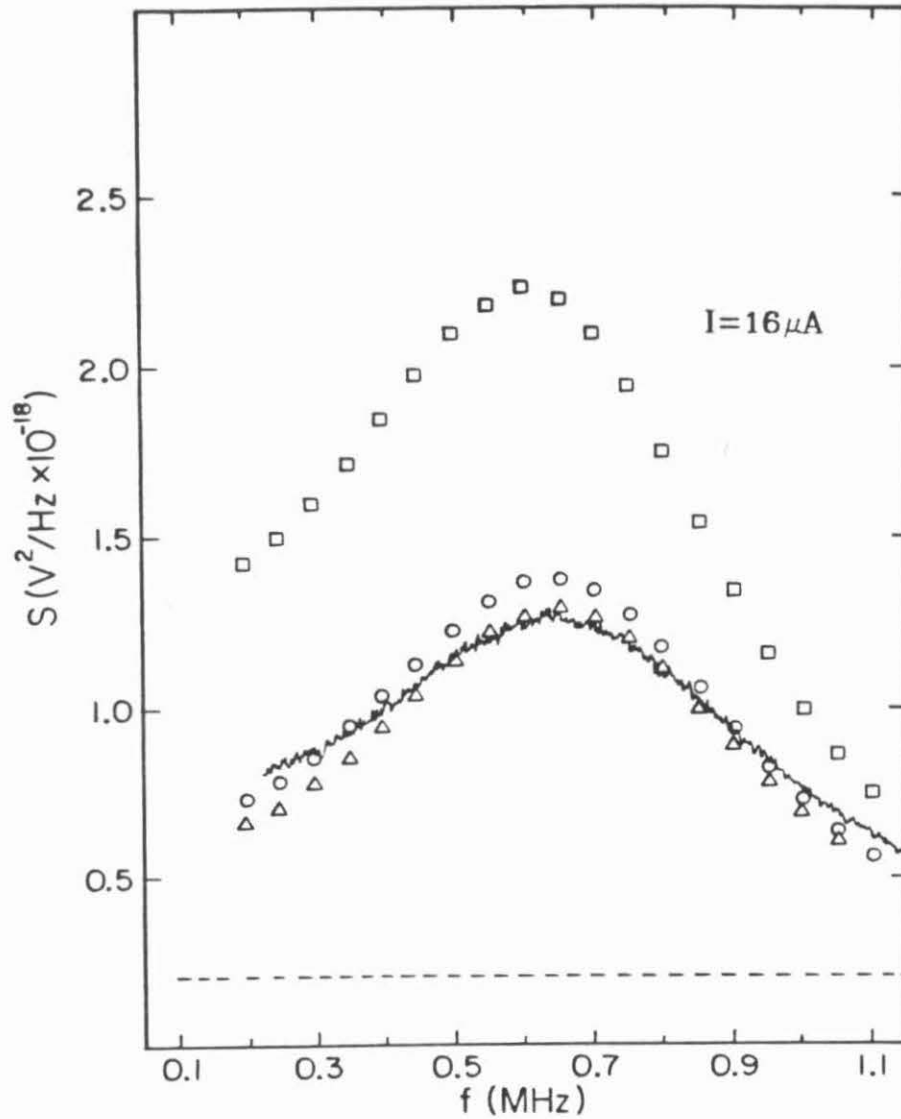


Figure 3.5b: Experimental and theoretical noise spectra for a bias current of  $I = 16 \mu\text{A}$ . Dashed curve is the preamp noise. Experimental spectra are continuous. Theoretical values are denoted as:  $\circ$ - total noise according to Eqn. 3.11,  $\square$ - total noise without correction for electrothermal feedback of Johnson noise,  $\triangle$  total minus Phonon noise.

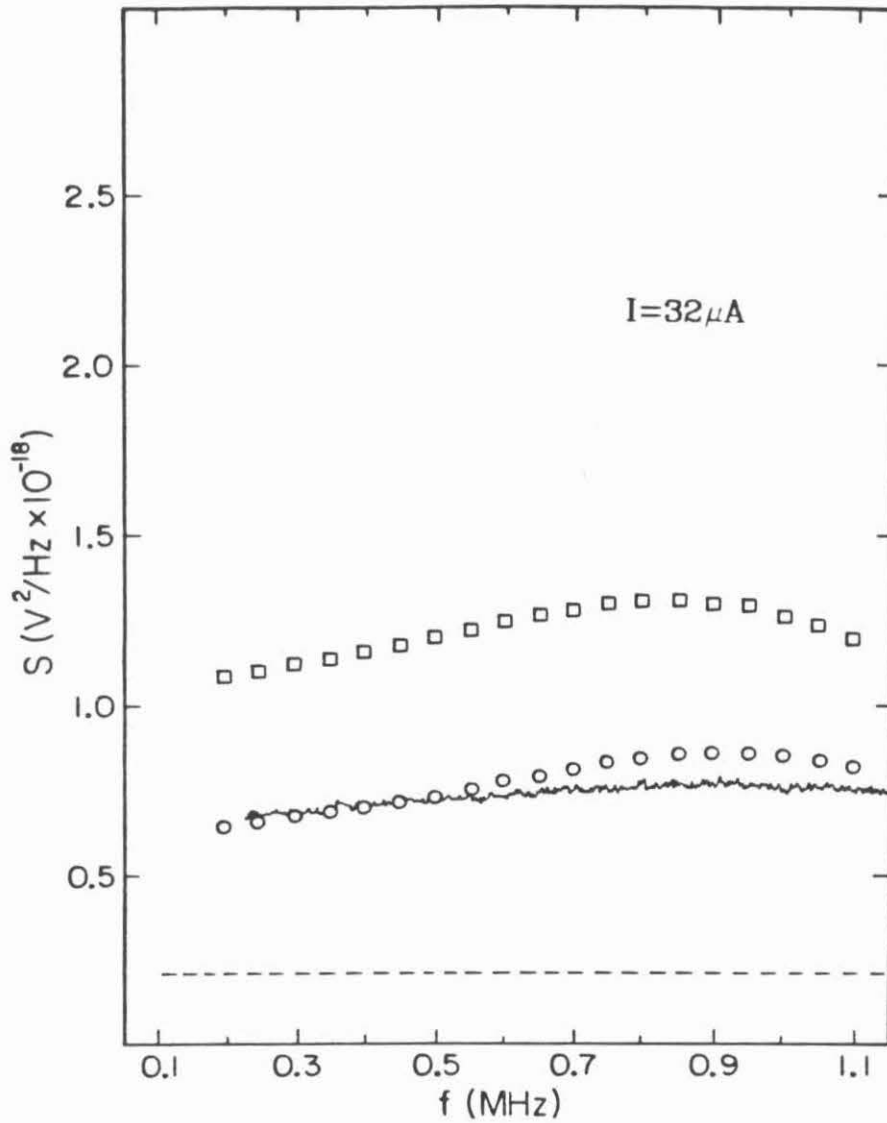


Figure 3.5c: Experimental and theoretical noise spectra for a bias current of  $I = 32 \mu A$ . Dashed curve is the preamp noise. Experimental spectra are continuous. Theoretical values are denoted as:  $\circ$  - total noise according to Eqn. 3.11,  $\square$  total noise without correction for electrothermal feedback of Johnson noise,  $\triangle$  total minus Phonon noise.

### 3.3 Rollin Mode Bandwidth

In this section, we first review the theory of bolometer response time. Then we briefly discuss experimental measurements made on the bandwidth of a high-quality Rollin mode detector.

#### 3.3.1 Bolometer Response Time Theory, Responsivity-Bandwidth Product

Assuming that the static energy balance is described exactly by Eqn. 2.12, one can define a unique bolometer response time. This is the observed relaxation time of the bolometer temperature to a step-function of incident radiation and is the solution to the dynamical power balance equation,

$$C \frac{d\delta T}{dt} + \delta P(t) - K\delta T = Q(t). \quad (3.14)$$

The quantities  $\delta P$  and  $\delta T$  are the changes of bias power and temperature due to the time varying radiation,  $Q(t)$ . The parameter  $C$  is the heat capacity and  $K$  is the dynamic thermal conductance,  $K=dP/dT_e$ , both evaluated at the bias point. In general,  $C$  is a function of  $T_e$  and  $K$  is a function of both  $T_e$  and  $T_b$ . Note that Eqn. 3.14 is valid only when the radiation power  $Q(t)$  is much smaller than the static bias power,  $P$ .

A bolometer having no electrical bias ( $P=0$ ) and negligible background radiation absorbed exchanges energy only with the bath. In this situation, the response time is

$$\tau = \frac{C}{K} \quad (3.15)$$

where  $C$  and  $K$  are evaluated at the bath temperature. Of greater concern is the response time,  $\tau_r$ , observed under biased conditions. Here, the bias network becomes another channel of energy exchange and has an important effect on

the response time. Assuming constant current bias,

$$\delta P(t) = I^2 \frac{dR}{dT_e} \delta T(t) \quad (3.16)$$

Solving the dynamical power balance equation now yields a response time [Jones 1953, Phillips and Jefferts 1973],

$$\tau_r = \frac{C}{K_r} = \frac{C}{K - I^2 dR/dT_e} \quad (3.17)$$

where  $K_r$  is the effective thermal conductance and all quantities are evaluated at the bias point. Now using the fact that  $dR/dP = (Z-R)/I^2(Z+R)$  [Jones 1953] and  $K = dP/dT_e$ , one can show

$$\tau_r = \frac{C(Z + R)}{2KR} \quad (3.18)$$

Notice that  $K_r$  is always greater than  $K$  for a negative bolometer, implying  $\tau_r < \tau$ .

An interesting exercise is to calculate the responsivity-bandwidth product. Roughly speaking, this is the quantity which is maximized in a given detector application. With a response time given by Eqn. 3.17, the frequency dependent responsivity is,

$$r(\omega) = \frac{r}{1 + j\omega\tau_r} \quad (3.19)$$

with  $r$  given by Eqn. 2.14. Therefore, the bolometer bandwidth is simply  $B = 1/(2\pi\tau_r)$ . Assuming again constant current bias, the responsivity-bandwidth product is,

$$r \cdot B = \frac{1}{2\pi} \frac{I}{C} \frac{dR}{dT_e} \quad (3.20)$$

Depending on the bolometer, this product can vary significantly with bias

current. In contrast, the analogous gain-bandwidth product for simple photoconductors is a constant under normal bias conditions.

### 3.3.2 Experimental Bandwidth

Shown in Fig. 3.6 is the bandwidth,  $1/(2\pi\tau_r)$ , for the 4002 sample tested in the previous section. The bandwidth was measured using the setup shown in Fig. 3.3. Notice that it increases gradually with bias current. The response time corresponding to the lowest bandwidth shown in Fig. 3.6 is very close to the often quoted value,  $\approx 2 \times 10^{-7}$  s [Putley 1977]. These other measurements were made with InSb samples much larger than the present 4002 detector. This illustrates an important, and unfortunate, feature of the InSb hot electron bolometer: the bandwidth is practically independent of the detector volume. This follows from the fact that both the heat capacity and the dynamic thermal conductance scale with the volume. It explains why the smaller cross section detectors display little or no improvement in the bandwidth, despite having much better responsivity than the bulkier devices.

Measurements were not made of the bandwidth as a function of material type or bath temperature. Experience has shown that reduction of the bath temperature below 4.2K actually decreases the bandwidth slightly [J. Keene, private communication]. On the other hand, increasing the bath temperature above 4.2K is known to enhance the bandwidth significantly [Putley 1977]. This prompted Putley to propose a liquid hydrogen (boiling pt. 20.4K at 1 atm.) cooled InSb detector, for which the bandwidth would be about 50 MHz [Putley 1978]. Unfortunately, the responsivity of InSb is at least an order of magnitude lower at 20K than at 4.2K. In addition, the phonon noise increases markedly and would probably dominate the Johnson noise at 20K. These problems would likely preclude a useful 20K detector in very small signal applications such as

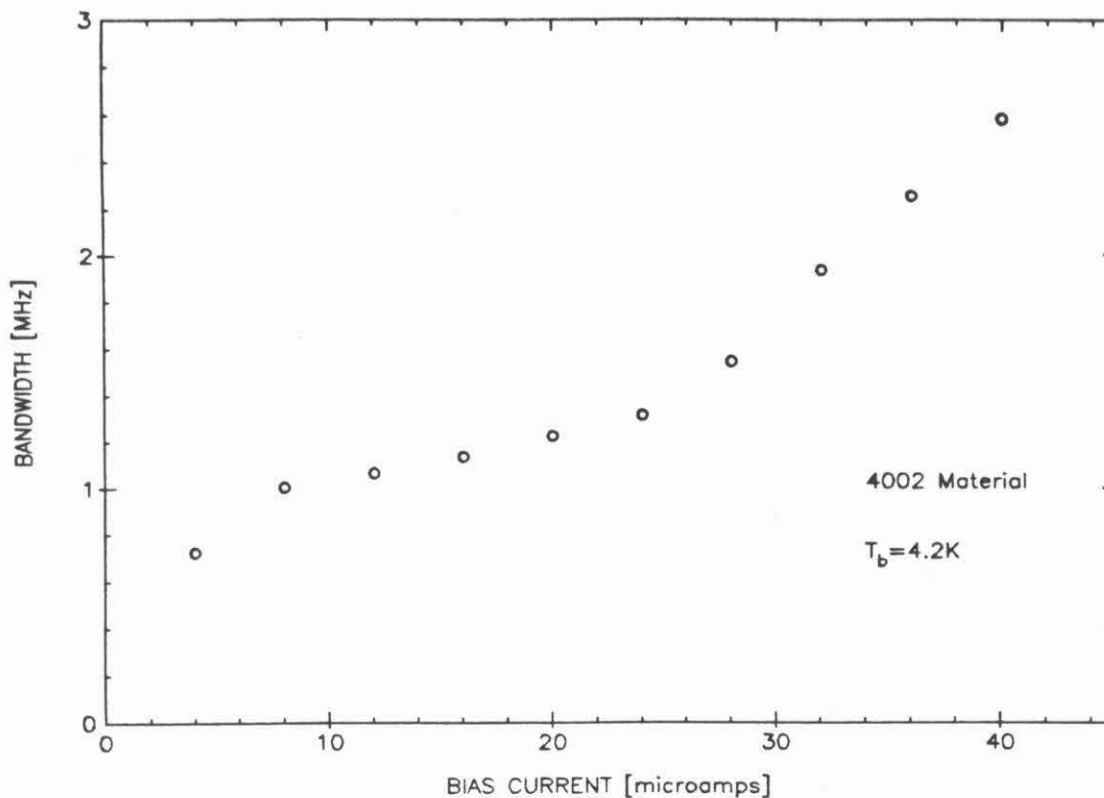


Fig. 3.6: Experimental bandwidth for a typical InSb bolometer

submillimeter astronomy.

### 3.4 Heterodyne Performance

The theory of heterodyne detection with the InSb bolometer has been worked out several times in the past but was presented most lucidly by Phillips and Jefferts [1973]. There are several results in this thesis that warrant a revision of their theory. In particular, we now know that the submillimeter absorption coefficient of InSb is practically uncorrelated with the DC conductivity and does not change with temperature. Phillips and Jefferts [1973] assumed that



the absorbed LO power varied with electron temperature in the same way as the absorbed bias power. In addition, we now understand the noise mechanisms much better than before. Consequently, a totally new theory of the heterodyne theory will now be developed. This new theory will enable us to predict the NEP at lower temperatures and for detector geometries not attempted before.

The most important step in the formulation of the theory is to find the small signal ideal responsivity in the presence of large absorbed local oscillator power ("large" means comparable to the DC bias power). Phillips and Jefferts found this by assuming that the net change of detector resistance under bias was small. This enabled a linear approximation that was valid only for  $\delta R/R < 1$ , where  $\delta R$  is the change of resistance due to the total absorbed electrical powers (bias + LO) and  $R$  is the resistance at the bath temperature. A much more accurate technique, and the one I will follow here, is an expansion of the detector resistance about the bias point. In principle, this is complicated by the fact that both the bias and LO powers display electrothermal feedback. In light of the absorption coefficient results in Sec. 2.7, I will assume that the absorbed LO power is constant. This is a tremendous simplification in that we can apply Eqn. 2.12 with  $T_e$  now the electron temperature in the presence of both bias and LO power. The value of  $T_e$  is found from the static power balance condition,

$$I^2 R + P_{lo} = G(T_e - T_b) \quad (3.21)$$

where  $R$  is the resistance at the bias point.

In formulating the system noise temperature, I will assume that the dominant source of detector noise is the non-equilibrium Johnson noise and that the amplifier is operated at ambient temperature,  $T_A$  and has noise resistance  $R_A$ . Following the theory presented in Sec. 1.3, we can now write the following expression for the double-sideband system noise temperature,

$$T_{sys} = \frac{4 [RT_e (1 - \tau)]^2 + R_A T_A] + 2h\nu\eta S^2 P_{lo} / k}{4\eta S^2 P_{lo}} \quad (3.22)$$

I now apply Eqn. 3.22 to a detector made of the 4002 material: the Phillips mixer used for airborne astronomy. In light of the results presented on the thermal conductance in Sec. 2.5, I will assume that  $G$  depends only on sample volume and not on the bath or electron gas temperature. This implies  $G=K=dP/dT_e$ . For the present detector,  $K=5.0 \times 10^{-8}$  W/K. The resistance of the detector was calculated using  $R(T_e)=R_b \sigma_b / \sigma(T_e)$ . The conductivity function was that found for the 4002 material in Sec. 2.4.

Shown in Fig. 3.7a is the LO power-dependent responsivity at  $T_b=1.8$ K. Notice how little absorbed LO power it takes to degrade the responsivity. When  $P_{lo} \sim P_{dc}$ , the responsivity is decreased by almost a factor of 2. Shown in Fig. 3.7b are the theoretical system noise temperatures vs. bias current for the LO powers considered in Fig. 3.7a and assuming  $\eta=1.0$  (i.e., ideal coupling). Notice that there is a distinct minimum for each  $T_{sys}$  curve. The minima occur at higher bias current with increasing LO power. The lowest minimum,  $T_{sys} \approx 40$ K, occurs for  $P_{lo} \approx 110$  nW. On comparison with Eqn. 1.9, we see that even this best theoretical  $T_{sys}$  is a factor of 3.5 above the quantum limited value  $T_{QL}$  at 500 GHz ( $\approx 12$ K). The performance is limited by the degradation of responsivity with LO power. This is a fundamental shortcoming of any bolometer mixer.

Given in Table 3.3 are the best experimental system noise temperatures achieved to date with the Phillips mixer in the Rollin mode. The best performance shown,  $T_{sys}=280$ K at 350 GHz, is about a factor of 7 above the theoretical detector noise limited performance for this mixer. The discrepancy is due, for the most part, to the non-ideal coupling efficiency of the real receiver. From Table 3.3, we see that the best values of  $T_{sys}$  increase rapidly between 350 and 576 GHz. This reflects the rolloff of the InSb absorption coefficient.

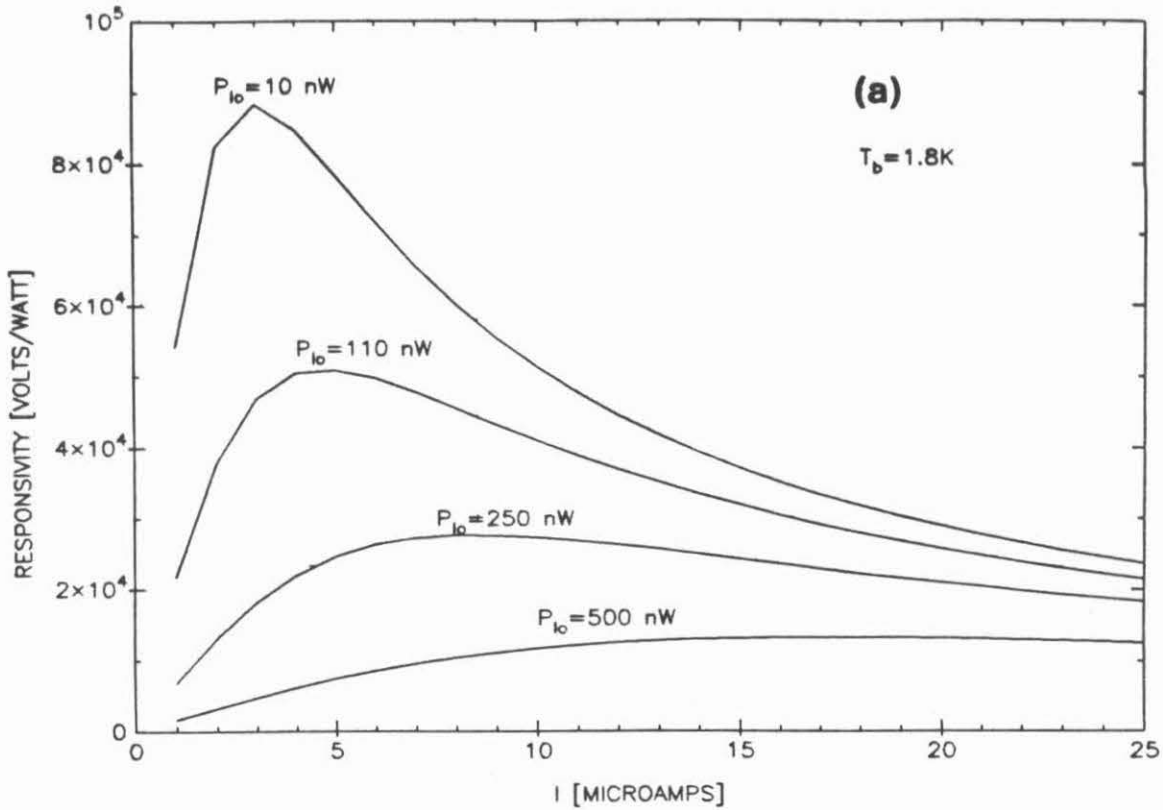


Figure 3.7a: Theoretical responsivity of the Phillips' mixer for various values of local oscillator power.

### 3.5 Conclusions

We are now in a position to summarize the InSb Rollin mode detector studies. First and foremost, we have shown that the 4002 material is superior to the other two materials investigated. This was evident from the absolute response spectra out to at least  $25 \text{ cm}^{-1}$ . Furthermore, there appears to be no simple way to increase the bandwidth of a hot electron bolometer without sacrificing responsivity. Because of these facts, I chose to abandon the high frequency Rollin mode mixer development and to investigate a new type of mixer which is based on the Putley mode effect.

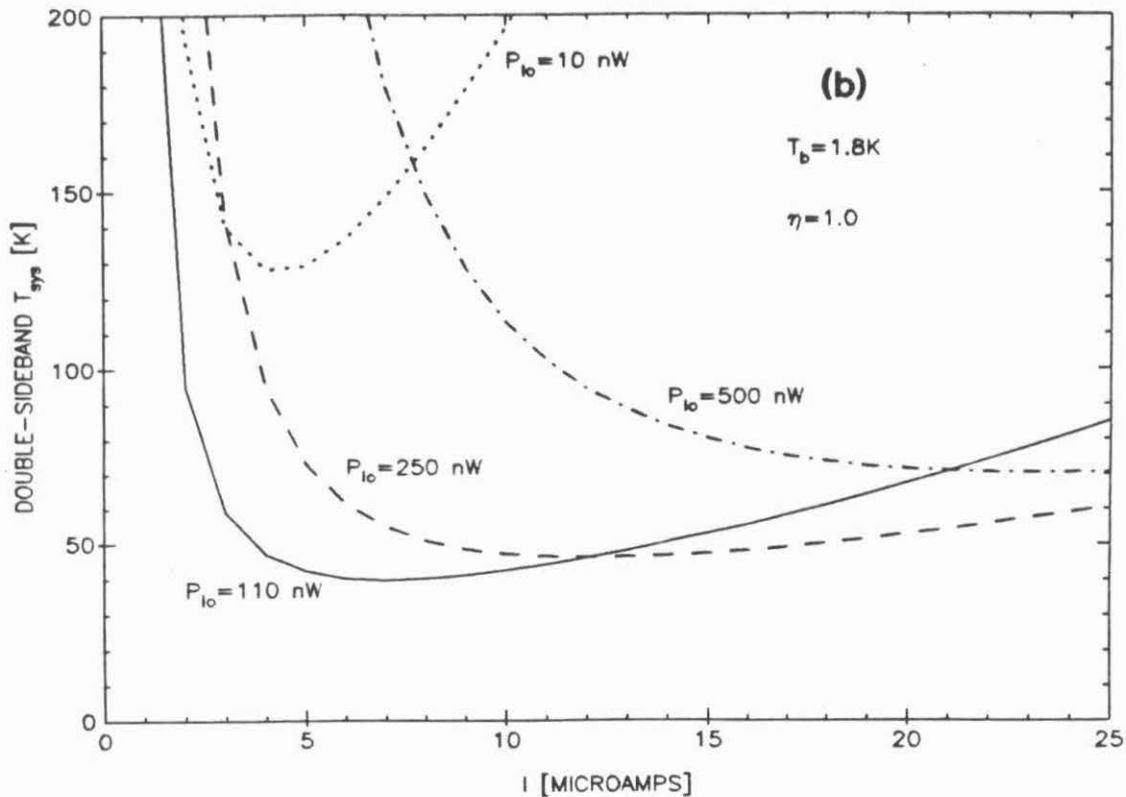


Figure 3.7b: Theoretical double-sideband system noise temperature of the Phillips' mixer for various values of local oscillator power.

The effort expended in arriving at these conclusions was not, however, in vain. A great deal was learned about the InSb hot electron bolometer. For example, we want to operate the bolometer at the lowest possible bath temperature and to construct it as thin as possible, independent of the material type. In practice, a detector cannot be made arbitrarily thin because of handling problems or because surface effects become dominant. Now assume that a minimum thickness has been determined. We then want the absorption coefficient to satisfy  $\alpha \sim 1/t$  where  $t$  is the detector thickness. Recall that the absorption coefficient was proportional, in the quantum limit, to the product of  $(n_d -$

<b>Table 3.3</b>		
<b>Performance of Phillips' receiver</b>		
$\nu$ (GHz)	$T_{sys}$ (K)	$T_{QL}/T_{sys}$
350	280	0.030
492	330	0.036
576	500	0.028

$n_a)(n_d+n_a)$ . The resistance and the maximum responsivity are, to first order, both inversely proportional to the free electron concentration,  $n_d-n_a$ . Therefore, *the best detector material will be that which has the minimum carrier concentration subject to the constraint  $\alpha \sim 1/t$ , where  $t$  is the minimum practical detector thickness*. In the past, it has been stated that the best InSb bolometer material is the most compensated [Vystavkin 1971]. I believe that the above criterion is more precise.

The above conclusions are important for optimizing a hot electron bolometer intended to operate a particular frequency. It is possible that with careful selection of material, some improvement of performance could be achieved. However, from the results of Sec. 2.7, it appears that the absorption coefficient of any detector grade InSb material will decrease very rapidly with frequency in the  $>600$  GHz region and at liquid helium temperatures. The reason for this is simply that under these conditions, the material is in the photon absorbing limit,  $\hbar\omega \gg kT_F$  and  $\omega\tau \gg 1$  where  $\tau$  is the momentum relaxation time. One can certainly imagine material that would not be in this limit. For example,

material with much higher carrier concentration or with much lower impurity concentration than 4002 would qualify. However, this would be inferior material in terms of responsivity and NEP. This is another reason to abandon the Rollin mode in favor of the Putley mode.

## 4. Putley Mode Detection

### 4.0 Introduction

When a magnetic field is applied to any solid containing free carriers, the carriers tend to rotate in the plane normal to the magnetic field due to the Lorentz force. If the motion is unimpeded by collisions, a carrier will revolve in a circular orbit with angular frequency  $\omega_c = eB / (m^*c)$  where  $B$  is the induction and  $m^*$  is the effective mass. In the present context, cyclotron resonance is the absorption of applied electromagnetic radiation that has frequency at or near  $\omega_c$ . In all practical situations, cyclotron resonance is damped by collisions of electrons with defects. The effect of the collisions is measured by the momentum relaxation time,  $\tau$ . The necessary condition for cyclotron resonance is simply  $\omega_c \tau \gg 1$ .

Since the 1950's, n-InSb has been one of the most important materials in which to study cyclotron resonance. The primary reason for this is that the electronic effective mass is very small,  $m^* \approx 0.0139 m_0$ . Therefore, the cyclotron resonance frequency varies rapidly with magnetic induction,  $f_c \approx 200 \text{ GHz/KG}$ . In addition, it is easy to grow material pure enough that the momentum relaxation time at liquid helium temperatures is relatively large. These facts imply that cyclotron resonance should be observable at relatively low magnetic inductions. For the material used in the present work  $\tau \sim 1 \times 10^{-12} \text{ s}$  at 4.2K and 0 KG. In this material the quantization condition,  $\omega_c \tau \gg 1$ , is equivalent to  $B \gg 0.8 \text{ KG}$ . For convenience, we will define the application of such values of induction to InSb as operation in the Putley mode.

In the previous two chapters, we saw that the performance of the InSb hot electron bolometer decays above  $\sim 500 \text{ GHz}$  because of the rolloff in the electronic inverse-Bremsstrahlung absorption (henceforth referred to as free

electron absorption). According to the argument given above, this is the frequency region in which cyclotron resonance should be observed. In this chapter, we will see if the quantizing magnetic field can enhance the detector performance in this region. We will start out by characterizing the direct-detection performance as the transition is made from free electron to cyclotron resonance absorption. Specifically, we will discuss the two most important indicators of this performance: the absolute responsivity and the NEP. Experimental measurements of these parameters were made in light of the following practical questions: (1) how does the detector performance at resonance compare with the hot electron bolometer performance? and (2) how does the performance depend on magnetic field, detector geometry, material and temperature? After discussing the direct detection performance, we will deal with the design and performance of the Putley mode heterodyne detector. The heterodyne results are the highlight of this thesis.

Before discussing the experimental results, it is important to have a feeling for just how big a difference the magnetic field should make on the absorption coefficient. The absorption coefficient data in zero magnetic field (Sec. 2.7.1) can be restated in terms of absorption cross section,  $\alpha/n$ , where  $n$  is the concentration of free electrons. For the 4002 material having  $n=3.4 \times 10^{18}$ , the cross section is  $\approx 9 \times 10^{-14} \text{cm}^2$  at  $30 \text{ cm}^{-1}$ . At the same wavenumber and in similar material, Murotani and Nisida [1972] measured a zero-bias absorption coefficient of about  $180 \text{ cm}^{-1}$  at the impurity cyclotron resonance (ICR) peak. This corresponds to an absorption cross section of  $\approx 7 \times 10^{-12} \text{cm}^2$ . To measure the absorption coefficient of the CCR transition, Gornik used a DC field to drive some fraction of the electrons bound to donor sites into the  $N=0$  Landau level [Gornik et al. 1978]. With sufficient DC field to transfer most of the electrons, the absorption coefficient for the CCR transition was found to be practically the



same as the ICR absorption with zero bias. This implies that the cross sections for the CCR and ICR processes are nearly equivalent.

From all of these absorption results, one can conclude that the cyclotron resonance cross sections are both much greater than the free electron value in relatively pure material at 4.2K and at wavelengths less than about 350 microns. Nevertheless, both processes will be active in most detector applications. This occurs because the cyclotron transitions react to only one polarization whereas the free electron process is polarization insensitive, at least in zero magnetic field. Thus photons with the wrong polarization for cyclotron absorption will likely be absorbed by the inverse Bremsstrahlung process in small fields or a similar process in high fields. If the thickness of the detector is such that a large fraction of the incident power is absorbed by these processes, then the free electron response may be comparable to or even exceed the cyclotron response. This may have been the reason for some of the early confusion regarding the effect of the magnetic field on the response of the Putley mode detector. In light of this problem the detectors studied in this chapter were intentionally made relatively thin.

#### **4.1 Absolute Responsivity of Putley Mode Detectors**

The absolute responsivity was measured with the FTS set-up described in Appendix C. The radiation coupling scheme and calibration procedure was identical to that used in Sec. 3.1. However, the Putley detectors were mounted in the bore of a superconducting solenoid that generated a uniform magnetic field directed parallel to the axis of the condensing cone.

Five detectors were made for this study. Three of these were the same bar geometry detectors studied in Sec. 3.1. The remaining two detectors were both processed from the 4002 wafer but had different geometries. The two

geometries were thin slab and needle (a very thin bar). All of these detectors were cut from the wafer using a diamond wire saw and then chemically etched to final dimensions. Sulfur-doped indium contacts were soldered onto each detector in a reducing atmosphere. The characteristics of all five detectors are summarized in Table 4.1.

The detector geometries used for this study were selected for special reasons. As in Sec. 3.1, the bar was chosen as the best geometry to compare different materials. Bars of the dimensions used here are very easy to make to a specific size without damage to the sensitive InSb crystal. The slab geometry was chosen for the purpose of calibration and because it is the simplest to use in very high frequency applications. The needle geometry is that of the waveguide mounted Rollin mode detectors such as that used in Sec. 3.2.

Each detector was DC biased with current flowing perpendicular to  $\mathbf{B}_0$  (transverse configuration). The slab detector was mounted with its plane  $\perp \mathbf{B}_0$ . The value of detector bias current was the intermediate value between the optimum for  $B=0$  and the optimum for  $B=10\text{KG}$ . Typically, the response at the intermediate bias was within 10% of the optimum response for all detectors and magnetic field values used.

One should bear in mind that all of these detectors are tested under the condition of Lambertian, randomly polarized illumination. Thus the polarization selection rules that apply to cyclotron resonance transitions should be satisfied by only about half of the incident photon flux. In addition, the detectors are backed by Eccosorb to eliminate all standing waves except those in the detector. The response results presented below are therefore considered to be conservative.

Shown in Fig. 4.1 are the voltage-current curves for detector 1. At 4.2K the detector displays a rapid increase of resistance with magnetic field and marked

**Table 4.1**  
**Properties of Five Detectors Tested**

Detector	1	2	3	4	5
Material	4002	4177	4190	4002	4002
Dimensions (cm)	.24x.036 x.036	.24x.033 x.033	.24x.038 x.038	.24x.20 x.035	.24x.018 x.018
Bias current ( $\mu$ A), $I_B$	20 @ 4.2K 12 @ 2.2K	30	20	160	10
Resistance, R (K $\Omega$ ), $I=I_B, B=0$ KG	1.05 @ 4.2K 2.42 @ 2.2K	0.64	1.12	.11	2.28
Ideal bolometric responsivity, S (KV/Watt), $S = \frac{R-Z}{2RI}, I=I_B, B=0$	8.1 @ 4.2K 15.3 @ 2.2K	3.9	8.3	0.86	19.5
Measured responsivity, (KV/Watt), $I=I_B, B=6$ KG, $\sigma=40$ cm <sup>-1</sup>	4.0 @ 4.2K 4.7 @ 2.2K	1.5	3.4	0.90	3.8

non-ohmic behavior due to hot electron effects. At 2.2K the detector shows the effect of impact ionization at a bias electric field  $E$  [V/cm]  $\approx .134B$  [KG],  $B > 5$ KG. The increase of critical electric field is consistent with the predicted increase of

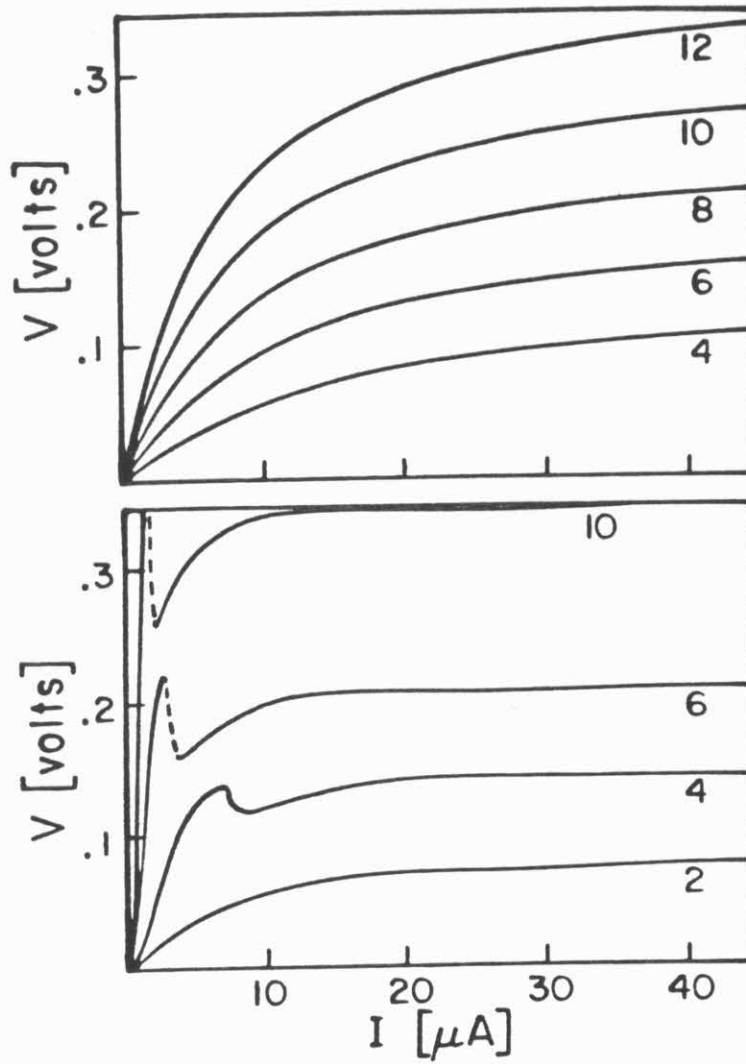


Figure 4.1: I-V curves of detector 1 at 4.2K (top) and 2.2K (bottom). The magnetic induction (KG) labels each curve.

donor binding energy with magnetic field in the hydrogenic model [Yafet et al. 1956]. In the dashed region of the V-I curve, instability was observed that depended largely on the impedance connected to the detector. Putley also observed this instability and attributed it to relaxation oscillations [Putley 1966].

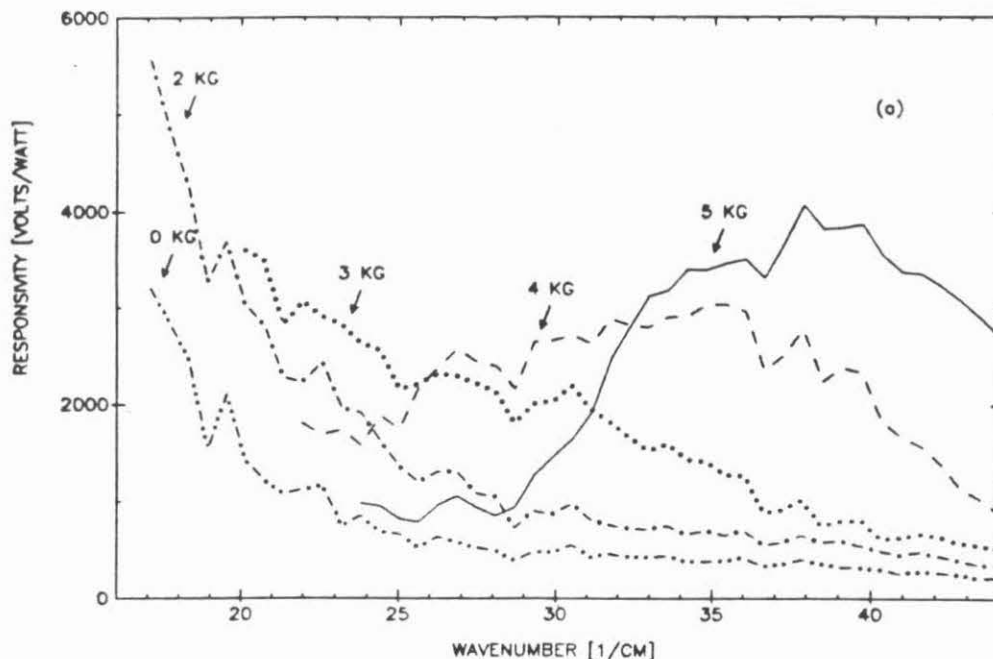


Figure 4.2a: Responsivity spectra for detector 1 at 4.2K and small magnetic fields.

The absolute responsivity of detector 1 at 4.2K and biased with 20  $\mu$ A is shown in Fig. 4.2. In Fig. 4.2a one can see in detail the behavior of the detector in the low-field region. The familiar hot electron bolometer response ( $B=0$ ) is characterized by the rapid roll-off with frequency. The structure in this curve is

caused by standing wave resonances in the detector. A field of 2 KG yields essentially the same spectral response shape as zero field but larger in magnitude due to the higher detector resistance. For B=3 KG there is a preliminary sign of cyclotron resonance: a slight bulge in the response spectrum that extends past  $30 \text{ cm}^{-1}$ . At B=4 KG one can see a small peak at about  $27 \text{ cm}^{-1}$ . This is probably caused by conduction electron cyclotron resonance since the peak frequency corresponds to  $\omega_c = eB/m^*c$  with  $m^* \approx .014m_0$  (the accepted value is  $m^* = .0139m_0$  @ B=0 [Johnson and Dickey 1970]). The response at larger wavenumbers is attributed to transitions of electrons residing in impurity states (ICR transitions).

The spectral responsivity of detector 1 at 4.2K and in the high field regime is shown in Fig 4.2b. There are two interesting features here. First, the peak response values of the B>4 KG spectra are nearly the same and are all greater than the Rollin mode response at  $17 \text{ cm}^{-1}$ . Second, the impurity response structure gradually shifts away from the CCR peak as the field increases. This is consistent with a theory of hydrogenic-donor states in quantizing magnetic fields (see below). Even at the largest fields, the impurity response remains relatively broad and is noticeably modulated.

The spectral responsivity of detector 1 at 2.2K and low magnetic fields is shown in Fig. 4.3a. In contrast to the 4.2K response, there is a high frequency bulge at 2 KG and obvious cyclotron resonance at only 3 KG. This is consistent with the greater degree of carrier freeze-out at the lower temperature. The associated high frequency response is seen in Fig. 4.3b. Here we see the dramatic effect of impact ionization. Between the magnetic fields of 4 and 6 KG, the impurity response completely disappears. Analysis of the cyclotron resonance peak that remains could yield useful information about the electronic transport in quantizing magnetic fields (see Sec. 4.4).

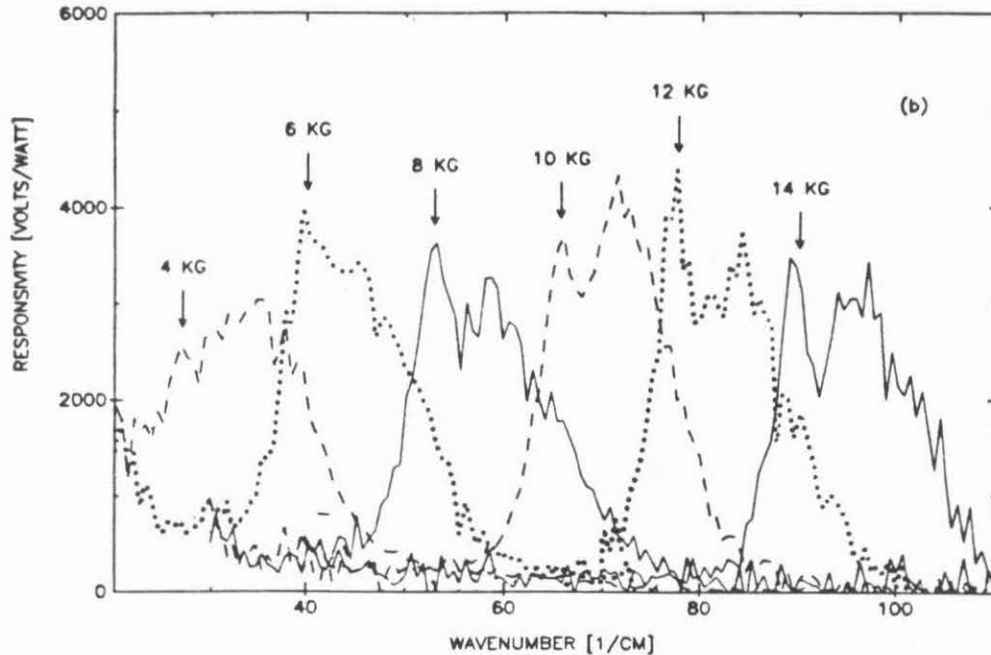


Figure 4.2b: Responsivity spectra for detector 1 at 4.2K in large magnetic fields. The vertical arrows are located at the CCR wavenumbers.

The absolute responsivity of detector 5 at 4.2K in the high field regime is shown in Fig 4.4. The CCR peaks are practically identical in shape and position as for detector 1; however, the impurity resonance shows almost none of the structure seen in Fig. 4.2b. The only difference between detectors 1 and 5, besides the thickness, is that detector 5 has enough taper to practically eliminate standing wave resonances. Therefore, the structure in Fig. 4.2b was probably caused by weak absorption of the inactive circular polarization (the opposite helicity of that absorbed by the impurity transitions) by free electron processes. The structure is always absent in the vicinity of the CCR frequency at

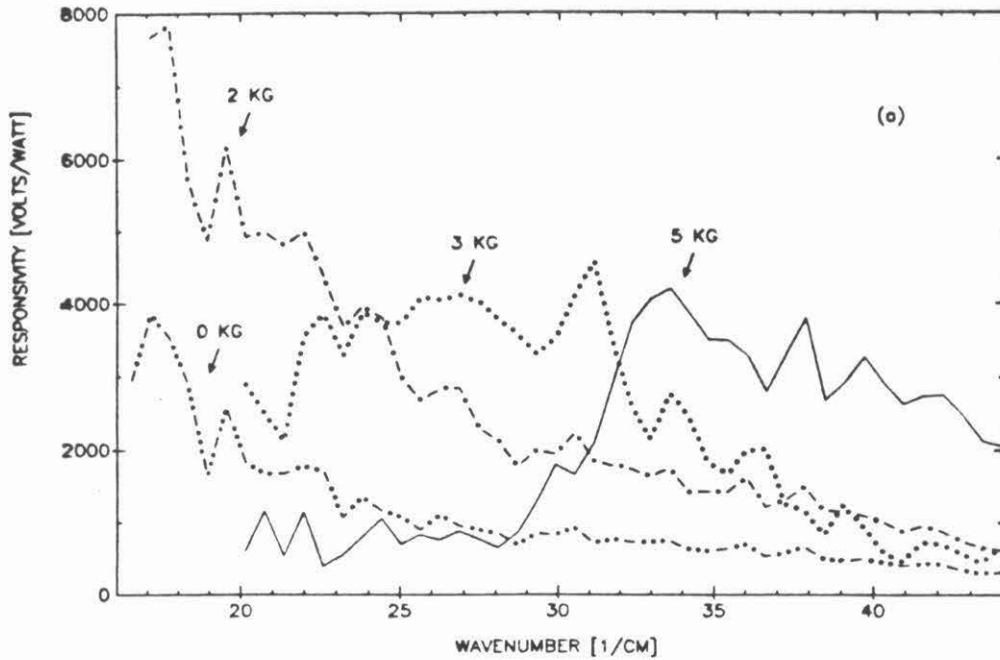


Figure 4.3a: Response spectra for detector 1 at 2.2K in small magnetic fields.

high magnetic fields because the absorption cross section for the CCR is much greater than the cross section for the free electron transition.

Shown in Fig. 4.5 are the values for the effective mass derived from the high field response curves of detector 5. The effective mass is calculated from  $m^* = eB/\omega c$  using field values determined from the magnet calibration tables supplied by the manufacturer (American Magnetics Inc.). The effective mass data points are then fit with the expression,  $m^* = m_0^* + m_0 \alpha B$ , where  $m_0$  is the free electron mass,  $m_0^*$  is the effective mass at the bottom of the conduction band in  $B=0$  and  $\alpha$  is the slope parameter. This expression predicts a linear



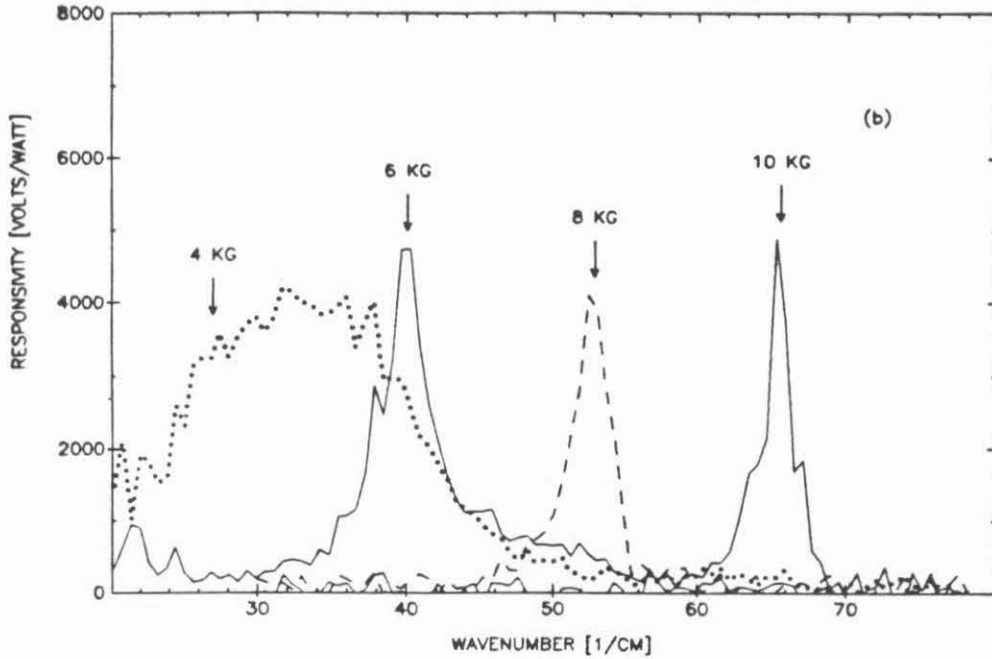


Figure 4.3b: Response spectra for detector 1 at 2.2K in large magnetic fields. The vertical arrows are located at the CCR wavenumbers.

variation of  $m^*$  with magnetic field and is an excellent approximation for fields less than about 20 KG and for low temperatures [Lax and Mavroides 1960]. Our data points yield  $m_0^* = .0139m_0$  and  $\alpha = 7.18 \times 10^{-5} \text{ [KG}^{-1}\text{]}$ . This value of  $m_0^*$  is exactly equal to the currently accepted value. Also shown in Fig. 4.5 are experimental values of cyclotron splitting,  $\Delta$ , defined as the difference between the the CCR frequency and the frequency at the peak of the impurity resonance. The data, shown in energy units, are compared to a theoretical prediction of Larsen [1968]. Larsen's curve resulted from a variational calculation of the (000) and (110) donor state energies using a hydrogenic model and the parabolic

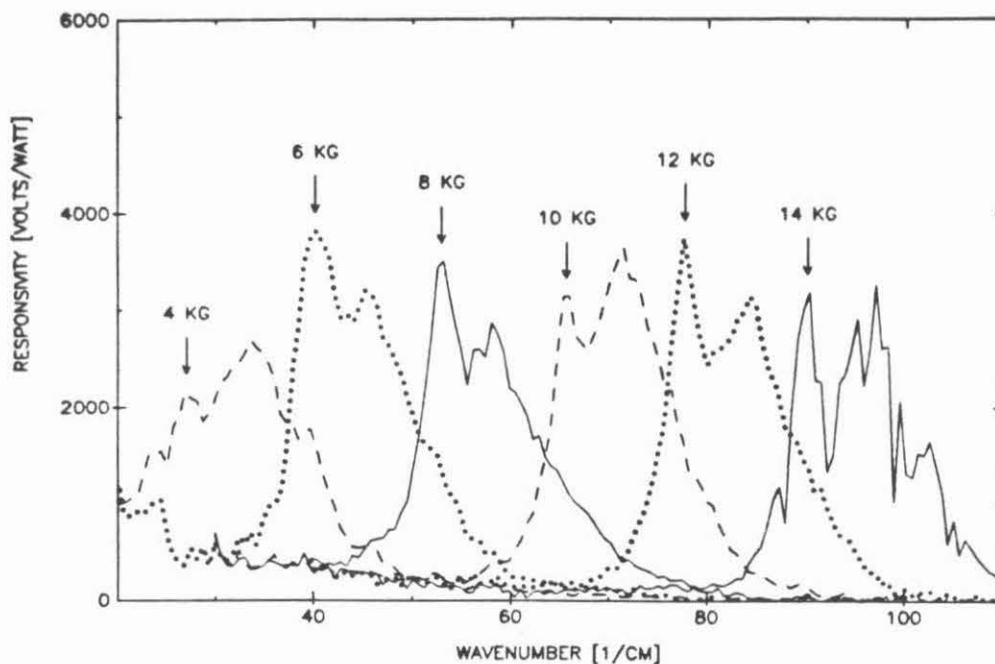


Figure 4.4: Response spectra for detector 5 at 4.2K in large magnetic fields. The vertical arrows are located at the CCR wavenumbers.

band approximation. For the range of magnetic fields shown here, a calculation based on realistic non-parabolic bands makes negligible difference in the cyclotron resonance splitting curve. Comparison of this curve with our experimental data shows a disagreement at the larger magnetic fields. The discrepancy is not understood at this time.

The V-I curves and spectral response of detectors 2 thru 4 are not shown here graphically for brevity; however, the important results for these detectors are summarized in Table 4.1. It is interesting to compare some of these results. For example, detectors 1 and 3 have practically the same resistance and

impedance at 4.2K although detector 1 has over 50% greater low frequency free electron response. This can be explained by the significant difference in the absorption coefficient of these two materials. It was suggested in Sec. 2.7.4 that the free electron absorption is proportional to the product of the total ionized impurity and electron concentrations. From Table 2.1, we see that this product is almost 90% greater in the 4002 material than in the 4190 material. On the other hand, the cyclotron resonance response at 6 KG is less than 20% different for the two detectors. It was found that the resistance and impedance of each detector, although increasing rapidly with B field, remained practically equal up to at least 10 KG.

Inspection of the results for detector 2 shows that it has by far the lowest response of the three bar detectors, independent of magnetic field. This is attributed primarily to its relatively low resistance. Recall from Table 2.1 that the 4177 material has the greatest carrier concentration and conductivity of the three materials at  $B=0$ . This was also true in larger fields. In fact, the magnetoresistance in a given magnetic field,  $M=(R(B)-R(0))/R(0)$ , is nearly the same for all three bar detectors. For example,  $M(10 \text{ KG})=10.1, 10.3$  and  $9.5$  for detectors 1, 2 and 3, respectively.

Upon comparison of the detectors 1 and 4, it is obvious that the bar detector has much more response than the slab for all values of field. This is explained by the fact that the bar has much greater resistance than the slab of equal thickness, and that the bar probably absorbs almost the same amount of incident power as the slab, despite filling only a small fraction of the condensing cone exit aperture. The bar absorbs both  $+1$  helicity circular polarized photons propagating  $\parallel \mathbf{B}_0$  and linear polarized photons that reflect off the condenser walls and strike the detector  $\perp \mathbf{B}_0$ . These are the familiar polarization rules for the  $1s \rightarrow 2p(m=+1)$  transition in the weak-field Zeeman split hydrogen atom: the

transition for which the  $(0,0,0,+)\rightarrow(1,\bar{1},0,+)$  ICR is the strong field analog.

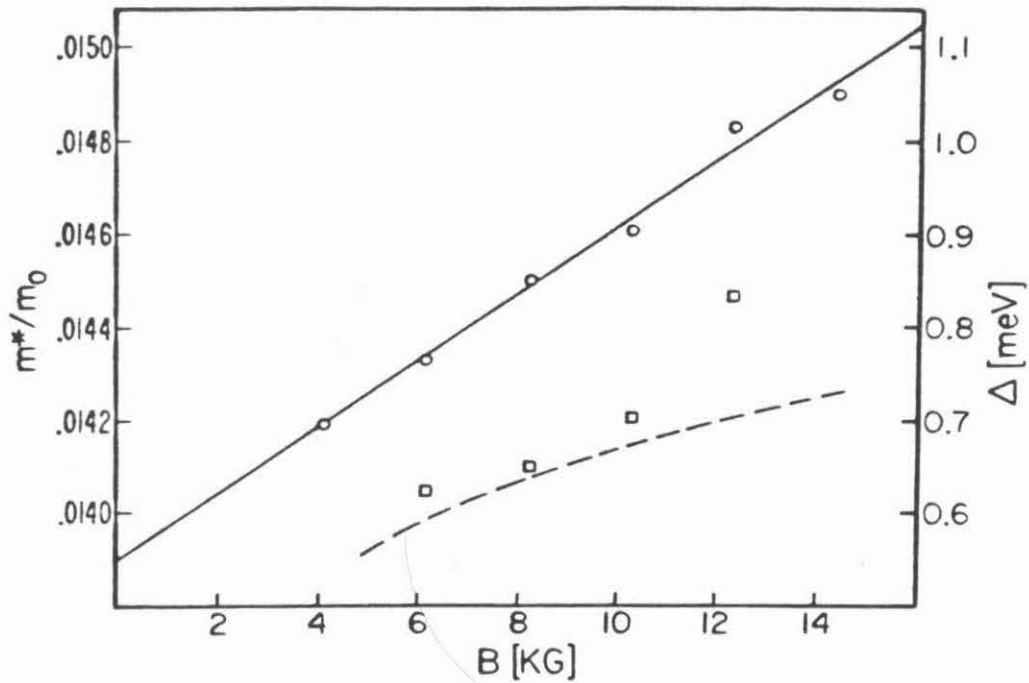


Figure 4.5: Cyclotron resonance characteristics:  $\circ$  - experimental effective mass for detector 5 at 4.2K (left scale), continuous line is the linear fit to the effective mass data points,  $\square$  - experimental value for the cyclotron resonance splitting in detector 5 (right scale), dashed line - theoretical splitting after Larsen [1968].

## 4.2 Noise and Direct Detection NEP of Putley Mode Detector

In this section I present the experimental measurements of the noise and direct detection NEP of the Putley mode detector. The measurements were carried out at 4.2K and in the transverse geometry on detectors 1 and 4 of Table 4.1.

### 4.2.1 Experimental Noise

The noise spectral density was measured at 200KHz using the amplifier described in Appendix D and the spectrum analyzer shown schematically in Fig. 3.4. This frequency is much less than the expected bandwidth of the InSb detector, which is about 0.8 MHz for  $B=0$  (Sec. 3.3) and increases with magnetic field (Sec. 4.4). Shown in Fig. 4.6 are the results for detector 1 with 20  $\mu$ A bias current applied. Notice how rapidly the noise increases with magnetic field.

Also shown in Fig 4.6 are several theoretical values of the equilibrium Johnson noise,  $S(f)=4kT_b R$ , where  $R$  is the resistance at the bias point. The experimental data points exceed this curve by very little at  $B=0$  but by about a factor of two at the highest magnetic field. From the separate Hall measurements, the 4002 material is known to begin freezing out carriers at about 2 KG with the bath at 4.2K. Therefore, we expect that there should also be a generation-recombination noise contribution as in all photoconductors [Bratt 1977]. In addition, the electron gas does display hot electron effects even in the presence of a quantizing magnetic field. This is obvious from the non-ohmic behavior of the I-V curves at 4.2K in Fig. 4.1. The physical mechanism behind the heating of the electron gas is much more complicated than in zero field and has been the subject of intense study recently [Otsuka 1980]. Because of this complication there exists no theory of the non-equilibrium Johnson noise as was the case with  $B=0$ . Therefore, I made no attempt to fit the data. However, it should be

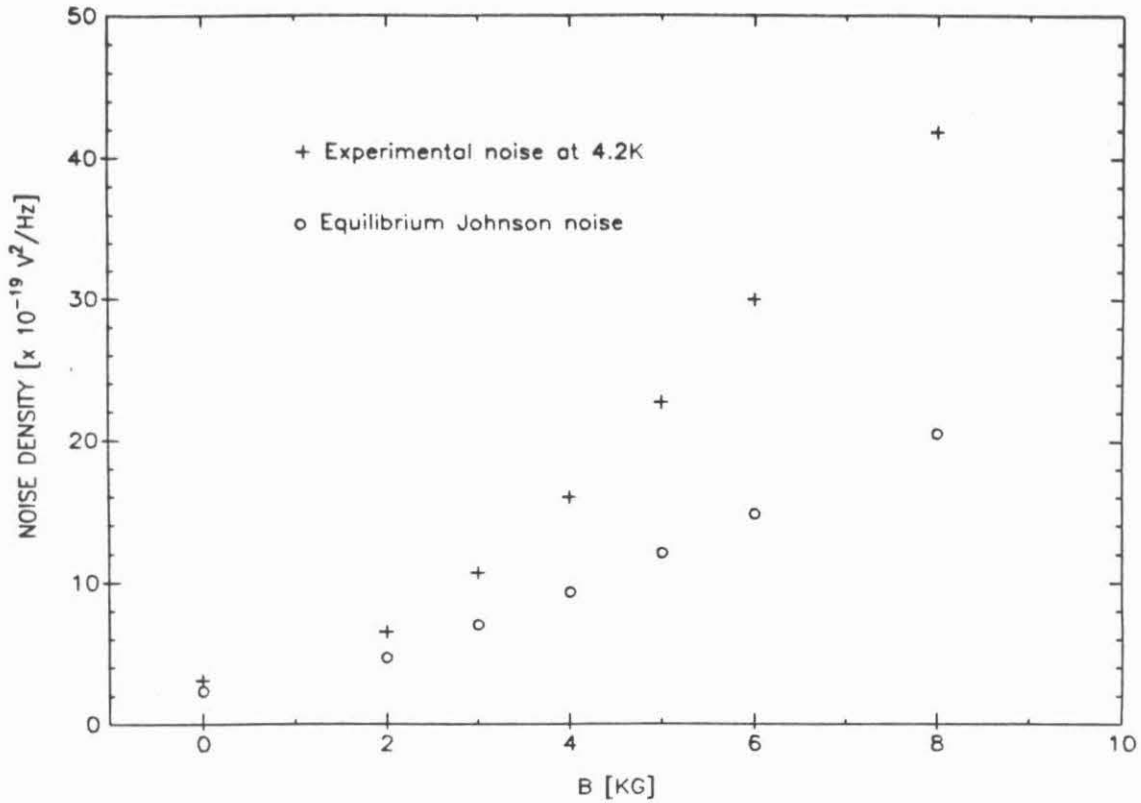


Figure 4.6: Noise of 4002 detector at 200 KHz and 4.2K.

mentioned that a reduction in the measured Johnson noise due to electro-thermal feedback (Mather's theory) is possible in the magnetic field.

#### 4.2.2 Direct Detection NEP

The direct NEP of the Putley mode detector was calculated as the ratio of the measured detector voltage noise density and the absolute voltage responsivity. Shown in Fig. 4.7 are some NEP values obtained for detector 1 at 4.2K. The line connecting the data points represents the approximate minimum NEP values obtainable at each wavenumber for the detector under the present

conditions. The rapid rise of the NEP between  $17 \text{ cm}^{-1}$  and  $20 \text{ cm}^{-1}$  is attributed primarily to the rolloff of free electron response and the relatively weak cyclotron response in this region. At slightly higher wavenumbers, the NEP levels off. This reflects the onset of strong, well-defined cyclotron resonance response. At still higher wavenumbers, the NEP rises again due to a fairly rapid increase of detector noise with magnetic field seen in Fig. 4.6. Note that the value  $4.5 \times 10^{-13} \text{ W/Hz}^{1/2}$  at 6 KG and  $40 \text{ cm}^{-1}$  is significantly less than Brown and Kimmit's [1963] commonly quoted result near the same wavenumber,  $\text{NEP} \sim 5 \times 10^{-11} \text{ W/Hz}^{1/2}$ .

Also given in Fig. 4.7 are several NEP data points for detector 4. As might be expected, they are higher than the values for detector 1. This is explained by the fact that detector 1 has about a factor of 4.5 more responsivity but only about a factor 2 more noise voltage than detector 4. These results are consistent with the following general characteristics of all the cyclotron resonance assisted detectors tested: (1) a large fraction of the noise in these detectors can be accounted for by the thermal expression,  $V_n^2 = 4kT_b R \Delta f$ , where  $T_b$  is the bath temperature,  $R$  is the resistance and  $\Delta f$  is the measurement bandwidth, and (2) the responsivity of a given detector at a cyclotron resonance peak is roughly proportional to the detectors resistance at the bias point. Therefore, the NEP at a given cyclotron resonance frequency is expected to vary with detector resistance roughly as  $R^{-1/2}$ , ignoring differences in radiation coupling efficiency. In other words, the more responsive a detector is at a particular wavenumber, the lower its NEP will be.

### 4.3 Direct Detection Discussion

We have demonstrated that the InSb hot electron bolometer can be transformed into a true cyclotron resonance detector with fairly small magnetic fields. For our best material, this occurs with about 4 KG at 4.2K and with about 3 KG at 2.2K. At all wavenumbers tested, the optimum NEP was always achieved with some applied magnetic field. The value of the optimum magnetic field depends on the wavenumber of interest but is always close to the conduction electron cyclotron resonance frequency,  $\omega_c = eB/m \cdot c$ .

Much like the case for hot electron bolometers, the response of the cyclotron resonance assisted detectors is quite sensitive to detector material. For the detector geometries studied here in the transverse configuration, the cyclotron response and the low frequency bolometric response are not, however, fully correlated. Whereas the bolometric response depends on the total impurity concentration and the fractional compensation, the cyclotron response simply reflects the detector resistance. This may be true because all the detectors used here were optically thick for the strong cyclotron transitions, CCR and ICR. Therefore, the best material to use for a cyclotron resonance assisted detector may not be the best hot electron bolometer material. Before any final conclusions are drawn, further experiments should be conducted with even thinner detectors than those used here.

We have also shown in Sec. 4.1 that when submillimeter radiation is collected with an integrating cone, the bar detector geometry is a much better choice than the slab of equal thickness. This follows because the bar detector has far greater resistance than the slab while it absorbs only slightly less power. With further optimization of the radiation coupling scheme, it should be possible to greatly improve the response and NEP results presented here. A very promising configuration would be the bar detector mounted across a waveguide with



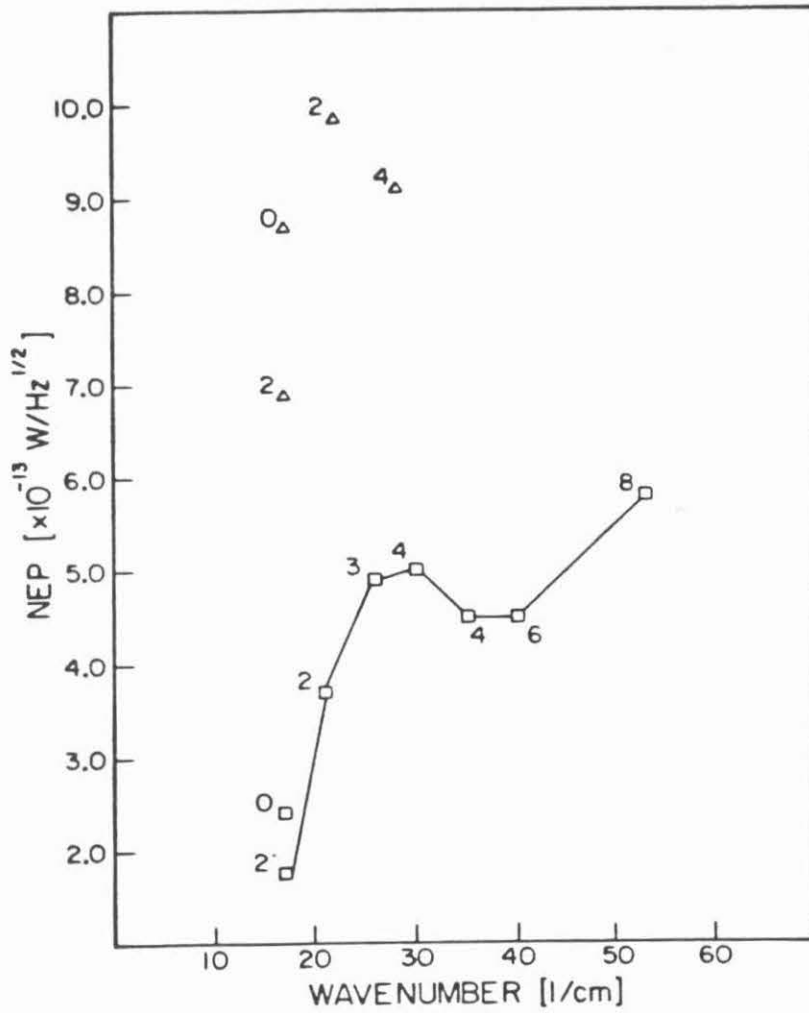


Figure 4.7: Experimental 4.2K NEP: detector 1 -  $\square$  , detector 4 -  $\triangle$  .  
The magnetic field values [KG] are written next to the data points.

magnetic field applied perpendicular to both the bar and the guide axis (Voigt configuration). From the polarization rules stated above, we would then get absorption of an electric field linearly polarized along the length of the bar. This is an easy requirement to satisfy in rectangular or circular waveguide.

#### **4.4 Cyclotron Resonance Photoresponse Mechanisms**

In this section, we discuss the photoresponse mechanisms of both the CCR and ICR transitions. This will help explain several of the features seen in the last section. In particular, we will be able to explain the constancy of peak responsivity with magnetic field and the apparent correlation of peak responsivity with detector resistance.

Of the two photoresponse mechanisms, the CCR is apparently the least understood. In particular, there exists sharp disagreement on the exact reason for the photoconductivity. From experiments conducted at liquid helium temperatures on GaAs, Bluysen et al. [1978] concluded that the mobility of an electron in the  $N=1$  and  $N=0$  levels is the same and that the change of sample conductivity with absorbed power is caused by a thermal equilibration from donor levels to the optically depleted  $N=0$  states. The responsivity spectra in Fig. 4.3b indicate that Bluysen's explanation does not apply to the 4002 InSb material. Specifically, these spectra show that under the condition of impact ionization the ICR response vanishes completely while the CCR response remains nearly constant. The disappearance of the ICR is expected since that transition will become optically thin when the donors are all ionized. Furthermore, if the CCR photoconductivity depended on a secondary equilibration of the donor levels, then it too would disappear under impact ionization. The fact that it didn't leads to the conclusion that the  $N=0$  to  $N=1$  transition alone must be photoconductive. In other words, the mobility of an electron in the  $N=0$  and  $N=1$  levels must be

different.

The mechanism of the ICR response has been determined as a rapid relaxation of the photo-excited electron from the bound (110) level to the conducting N=0 Landau level followed by a relatively slow relaxation back down to the (000) state [Muller 1978]. Therefore, we can think of the ICR detector as a simple photoconductor with the response time,  $\tau$ , equal to the relaxation time from the N=0 sub-band to the (000) donor state. The theoretical expression for the open-circuit responsivity of this non-linear photoconductor is [Putley 1964],

$$\tau = \frac{\eta \tau_l Z}{N h \nu} \quad (4.1)$$

where  $\eta$  is the radiation coupling efficiency,  $I$  is the bias current,  $Z$  is the dynamic resistance and  $N$  is the total number of electrons in the N=0 level. From the I-V curve of Fig. 4.1a, we measured the quantity  $Z$  at the bias point and found it to increase by  $\approx 2$  between 4 and 12 KG. Over the same range, the factor  $1/\nu$  evaluated at the ICR peak decreases by  $\approx 2.7$ . Hall measurements on the same material indicated that the factor  $1/N$  increases by  $\sim 3$  between 4 and 12 KG. This reflects the well-known magnetically induced carrier freeze-out. Finally, the relaxation time of the N=0  $\rightarrow$  (000+) transition was measured using an amplitude modulated signal derived from a frequency-multiplied klystron and was found to decrease by  $\sim 3$  over the range. All of these factors change in such a way that the peak responsivity remains roughly constant with magnetic field. The value of the theoretical responsivity was found to be about 4.3 KV/W at 6 KG. This is comparable to the experimental result and somewhat smaller than one might expect considering the fact that the experimental coupling efficiency for this detector is certainly less than 50% (its geometrical cross section is much smaller than the exit aperture area of the condensing cone). Note that this interpretation of our experimental results is made possible by the fact that the

detector is assumed to be optically thick at the ICR resonance peak for all the fields used. Without this condition, there would be changes in the absorbed power with magnetic field.

#### 4.5 Response Time of the Putley Mode Detector

Because the CCR and ICR mechanisms are basically unrelated, they should have different response times. The work of Muller et al. [1978] showed that the ICR response time is determined by the relatively slow recombination of electrons in the N=0 Landau level with the ionized donors. They experimentally determined the response time at 4.2K bath temperature using several different techniques, all of which gave the same result:  $\tau \approx 200$  ns in B=0 decreasing with magnetic field to about 50 ns at B=10 KG. The slight decrease with magnetic field is caused by the increase in the strength of the electron-phonon interaction with magnetic field [Kogan 1963]. They did not measure the response time at sub-4.2K temperatures.

In a related paper, Gornik et al. [1978] studied the response time of the CCR mechanism. They found that this time decreased rapidly when the concentration of electrons in the N=1 level increased past a certain value,  $\sim 1 \times 10^{10}$ /cc. The effect was consistent with electron-electron scattering being the dominant relaxation mechanism. It also explained the fact that a steady state population inversion could not be maintained and so continuous wave laser action was not possible. Their empirical expression for the lifetime time of N=1 electron was

$$\tau_1 \sim \frac{64B(\bar{E})^{3/2}}{n_1} \quad (4.2)$$

where  $n_1$  is the concentration in the N=1 level, E is the mean energy of an electron in the N=1 level measured in units of meV and B is the magnetic field measured in units of KG. They also found that when the electron concentration in the

N=1 level is near the thermal equilibrium value, then the electron-electron scattering becomes ineffective. In this situation, acoustical phonon interaction again determines the lifetime. The CCR detector response time is then comparable to that for the ICR detector.

Although Eqn. 4.2 seemingly precludes the attainment of continuous wave lasing action in bulk n-InSb, it offers hope that the bandwidth of the CCR detector can be significantly enhanced by operating with large radiation levels such as those present in the heterodyne mode. To test this idea, let's suppose that the CCR detector is being illuminated by enough local oscillator power,  $P_{lo}$ , that the population in the N=1 level is dominated by the photo-induced carriers. Assuming that simple photoconductor theory applies, one can write [Putley 1964]

$$n_1 = \frac{\tau p}{h\nu} \quad (4.3)$$

where p is the LO power absorbed per unit volume. This can be combined with Eqn. 4.2 to eliminate  $n_1$ , yielding

$$\tau_1 = \left( \frac{64B\sqrt{E}h\nu}{P} \right)^{\frac{1}{2}} \quad (4.4)$$

We now ask the practical question, what LO power absorbed per unit volume is required to achieve a time constant of, say, 20 nsec: a factor of 10 improvement over the Rollin mode detector! Assuming that  $B=4$  KG,  $\nu=eB/(m^*c)$  and  $E=3/2(\hbar\omega_c)$ , we find  $p \approx .76$  mW/cm<sup>3</sup>. The typical volume of the high quality Putley mode mixers discussed in Sec. 4.6 is about  $1 \times 10^{-6}$  cm<sup>3</sup>. Therefore, Eqn. 4.4 implies that a 20 ns time constant (or an 8 MHz bandwidth) can be achieved in the CCR mixer with only 9 nW of absorbed LO power. This prediction will be tested in Sec. 4.6.2.

During the course of the present studies, only one experiment was conducted to directly determine the response time of the Putley mode detector. It was performed by amplitude modulating a klystron with a sweep oscillator and measuring the response spectrum of a Putley mode detector placed in the immersion dewar of Fig. C.1. The klystron was frequency tripled so that the radiation absorbed by the detector was at 300 GHz. With the detector at 4.2K, the bandwidth was found to increase from about 1 MHz to 2 MHz with an increase in magnetic field from 0 to 10 KG. In fact, 300 GHz radiation is probably absorbed more efficiently by the free electron processes than by either the ICR or CCR transitions. Nevertheless, the increase in bandwidth observed should reflect an increase in the ICR bandwidth because both the free electron and ICR relaxation times are limited by interaction between  $N=0$  electrons and acoustical phonons. Because of the lack of a modulatable source at higher frequencies, no experiments were conducted to measure directly the response times of the CCR and ICR transition. In fact, the CCR response time has never been measured directly. Gornik et al. [1978] deduced it from a saturation measurement.

#### **4.6 Putley Mode Heterodyne Detection**

Like any other liquid helium cooled mixer for the submillimeter region, the Putley mode detector had to be mounted on the cold finger of a dewar. An immersion cryostat like that used in Sec 4.1 is generally unsatisfactory because of radiation losses down the long length of light pipe or waveguide. Initially, I thought that a superconducting magnet could be mounted on the cold plate of a standard liquid helium dewar. However, a brief amount of consultation with other people in the cryogenic field revealed that cold plate mounted magnets could not be made to deliver fields greater than  $\sim 1$  KG. The problem is that the heat leak through the necessary current leads cause the magnet to go normal.

Therefore, a dewar was designed with the solenoid placed in the bath. This particular dewar is discussed in Sec. 4.6.3 In a parallel effort, an existing dewar was configured to operate the Putley mode mixer in permanent magnets. This effort is discussed in Sec. 4.6.2.

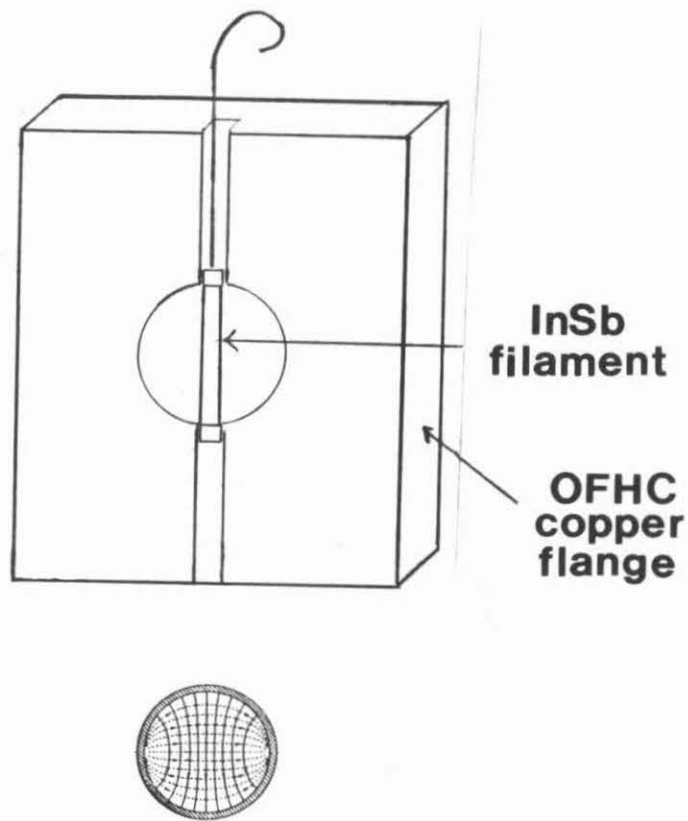


Figure 4.8: Putley mode mixer mounting structure. Also shown is the pattern for the fundamental TE<sub>11</sub> mode of circular waveguide. The electric field lines are continuous.

#### 4.6.1 Mixer Mounting Structure

Shown in Fig. 4.8 the Putley mode mixer mounting structure. The mixer is a filament of n-InSb mounted across a 0.028 inch diameter circular waveguide. This configuration has the virtue of combining high detector responsivity with good power coupling efficiency. It is the same configuration that was used for the hot electron bolometer mixer discussed in Sec. 3.4. The responsivity is high because the filament geometry yields low carrier concentration or, equivalently, high detector resistance. The power coupling efficiency is good because the filament occupies a region of the waveguide where the electric field of the fundamental  $TE_{11}$  mode is most concentrated. This is evident from the field pattern of the  $TE_{11}$  mode which is shown in the bottom part of Fig. 4.8. The detector itself is approximately 0.006 inch (0.015 cm) thick and has the usual low-resistance contacts made of sulfur-doped indium. This thickness is fairly close to the inverse absorption length measured in very similar material by Murotani and Nisida [1973],  $1/\alpha \sim 0.01$  cm.

#### 4.6.2 Voigt Configuration Experiments: Laser Heterodyne Results

Shown in Fig. 4.9 is the schematic diagram of the receiver front-end. The magnetic field is applied perpendicular to both the filament and to the waveguide axis. In this (Voigt) configuration, photons are absorbed that have polarization linear to the filament. The magnet is made of a rare-earth cobalt alloy and generates an induction of about 3.0 KG at the position of the mixer. This value was determined by replacing the mixer block with a calibrated InAs Hall probe operated at room temperature. Radiation is coupled into the waveguide with a conical feedhorn. Experience with this coupling technique has shown that with linearly polarized, near-Gaussian local oscillator illumination, only the  $TE_{11}$  mode of the circular waveguide is significantly excited. This is



expected since the higher order TE modes of the circular waveguide have very complex electric field patterns which, in some cases, have sinks in the central region. For the specific dimensions of the structure in Fig. 4.8, the cutoff frequency of the  $TE_{11}$  mode is about 247 GHz.

Shown in Fig. 4.10 are the I-V characteristics of the InSb mixer with and without magnetic field and at temperatures of 4.2 and 1.6K. Notice that at 4.2K, the detector resistance is enhanced greatly by the magnetic field. This is typical for the transverse bias geometry used here. When the bath temperature is reduced at a fixed magnetic field, the I-V curve again becomes highly non-ohmic. In contrast to the situation at 1.6K in zero-magnetic field, the sample now displays two regions of negative dynamic resistance. The second region is a precursor to impact ionization breakdown: a phenomenon which occurs because of magnetic field induced freeze-out of the electrons onto donor sites. Surprisingly, the noise of the detector did not increase very much when the bias was set at the point of negative dynamic resistance.

Shown in Fig. 4.11 is the set-up used to characterize the cyclotron resonance receiver at 812 GHz. The LO power at this frequency was obtained from a methanol waveguide laser pumped by the 9P16 line of a RF excited  $CO_2$  waveguide laser. Coupling into the receiver was accomplished with a 0.001 inch mylar sheet which is about 10% reflecting for the TE polarization. The receiver noise temperature was obtained by mixing alternatively with ambient and liquid nitrogen cooled Eccosorb loads. These are known to have close to unity emissivity in the far-infrared wavelength region.

Shown in Table 4.2 is the receiver performance obtained at 812 GHz and 1.6K bath temperature. Also shown are the best performances obtained by this Putley mode configuration at 492 and 625 GHz. The LO power at these frequencies was obtained from frequency-multiplied klystrons in a separate experiment.

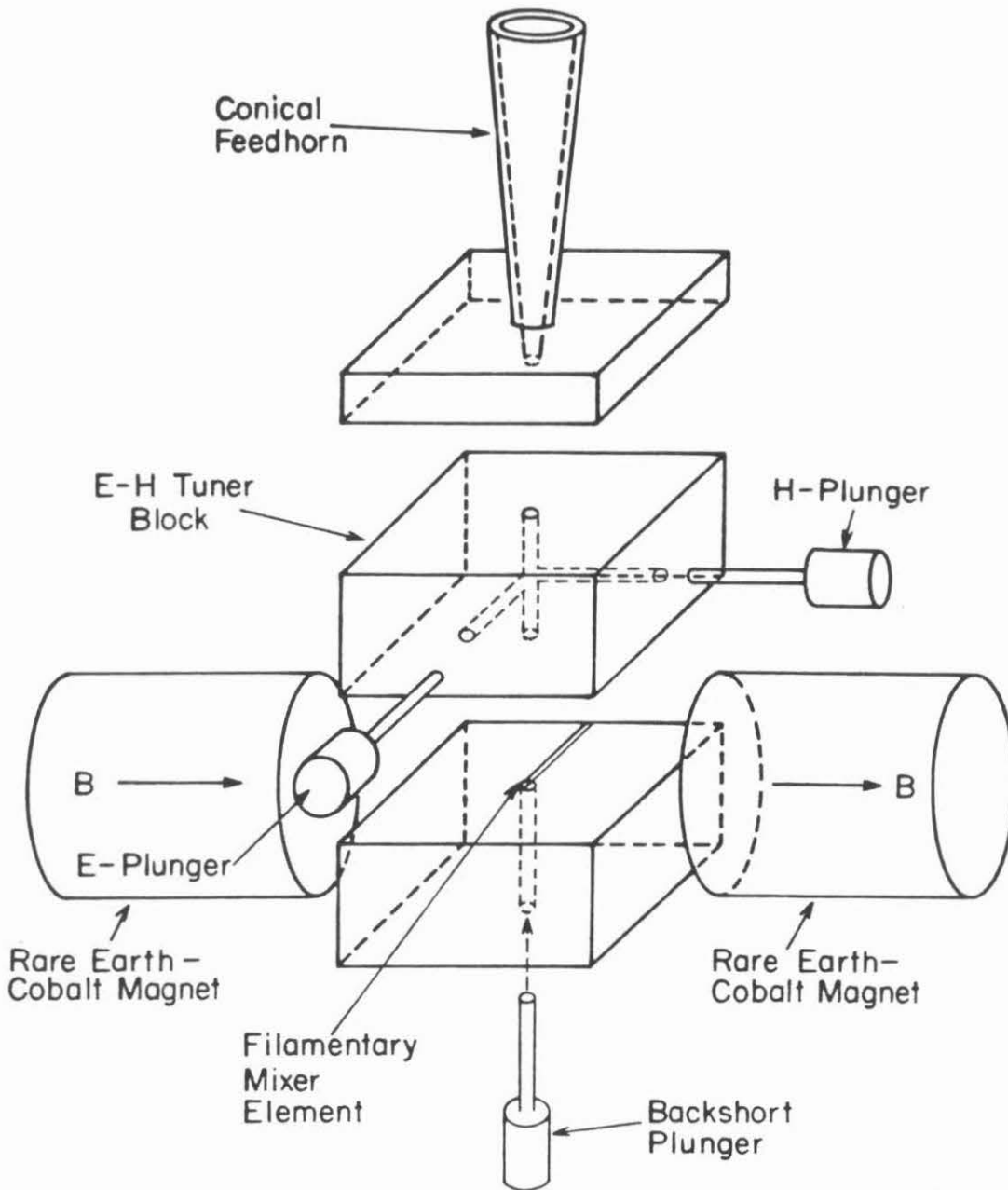


Figure 4.9: Block diagram of heterodyne receiver front-end with the mixer oriented in the Voigt configuration.

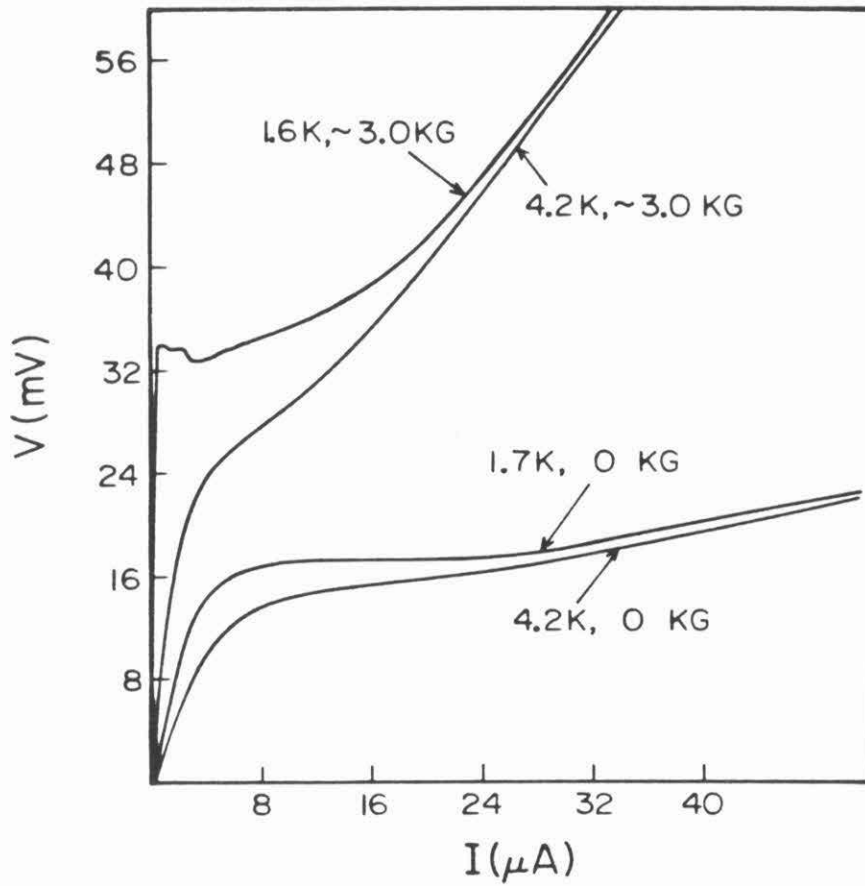


Figure 4.10: I-V characteristics of InSb mixer with and without magnetic field applied and at both temperatures of 4.2 and 1.6K.

FAR-INFRARED HETERODYNE EXPERIMENT

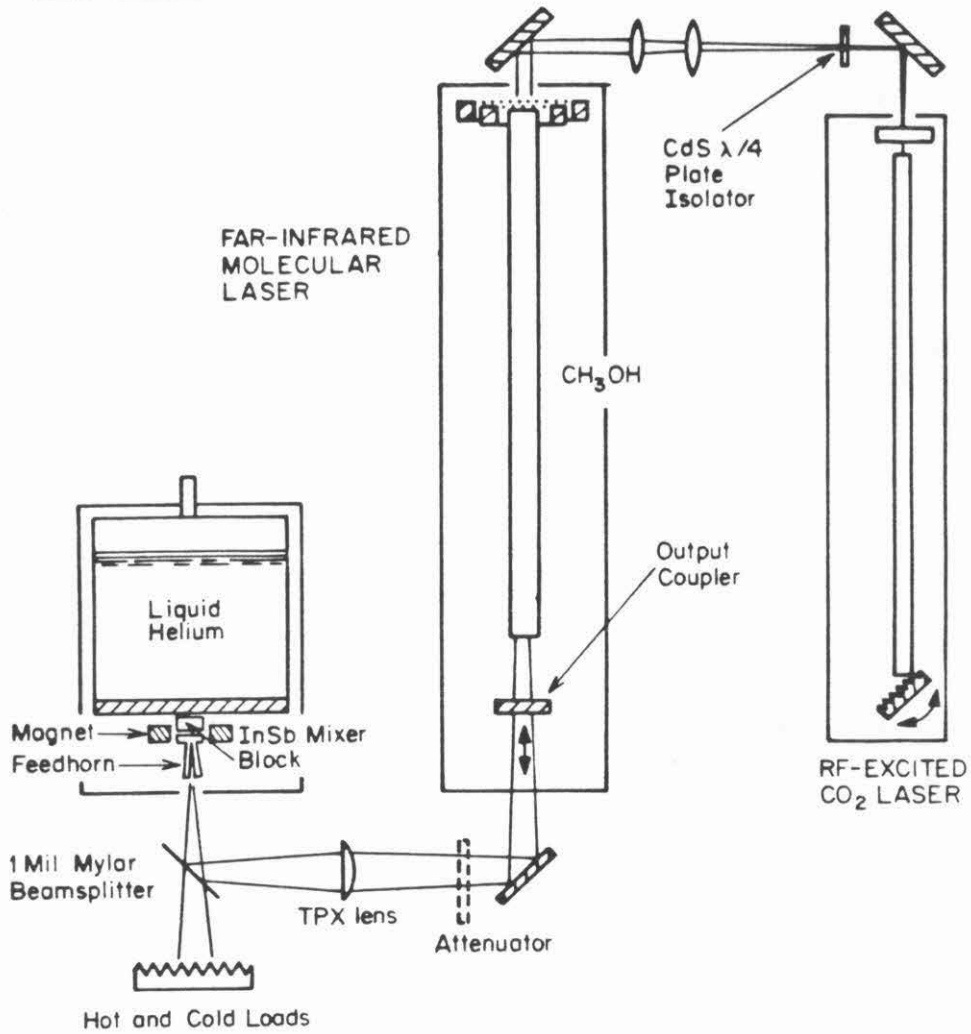


Figure 4.11: Schematic diagram of laser heterodyne experiment.

<b>Table 4.2</b> <b>Performance of Putley Mode Receiver</b> <b>in Voigt Configuration</b>		
$\nu$ (GHz)	$T_{sys}$ (K)	$T_{QL}/T_{sys}$
492	250	0.048
625	350	0.043
812	510	0.038

Shown in Fig. 4.12 is the I-V curve plotted with and without the 812 GHz LO power that yielded the minimum system temperature. Notice that the LO power reduces the mixer resistance and causes the region of negative dynamic resistance due to freeze-out to disappear completely.

Operation with the laser LO also afforded an estimation of the IF bandwidth of the Putley mode detector. To determine the bandwidth, we measured the spot noise temperature as a function of intermediate frequency using the spectrum analyzer shown schematically in Fig. 3.3. The value of  $T_{sys}$  was found to increase by about a factor of 2 between 100 KHz and 0.75 MHz. Although this is thought to represent some improvement over the bandwidth in zero magnetic field at the same temperature, it is certainly not what we had hoped from Eqn. 4.4. The reason cannot be too little local oscillator power: conservative estimates imply that the detector was absorbing at least 100 nW. More likely, in the above experiment we were seeing dominant ICR rather than CCR absorption or,

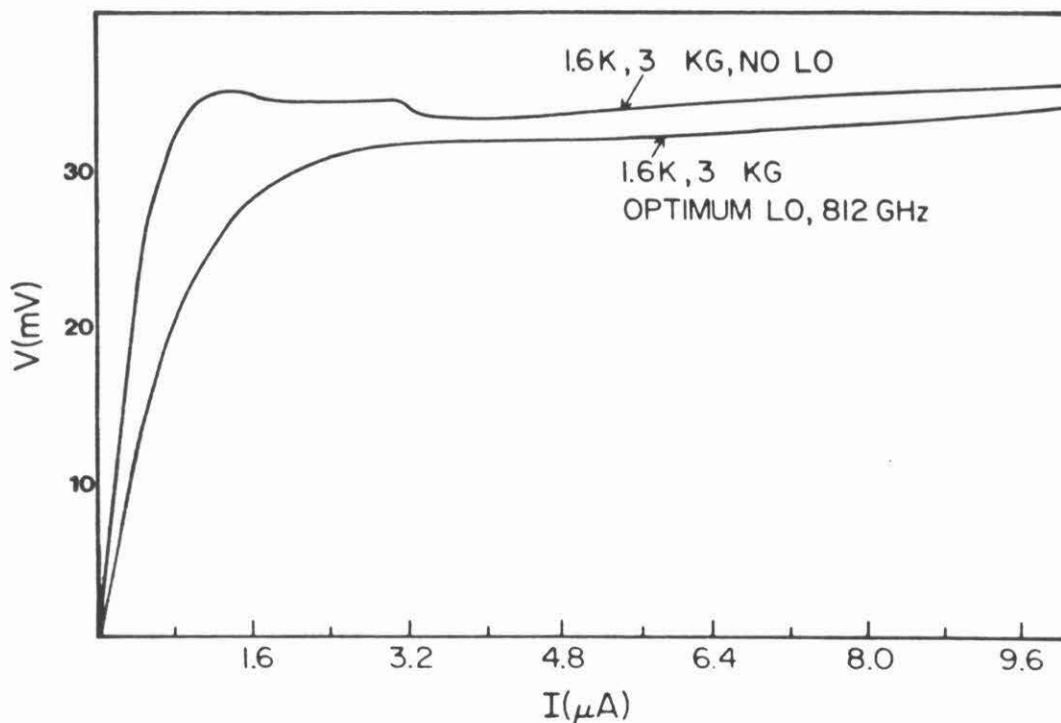


Figure 4.12: I-V curve of Voigt configuration mixer at 1.6K bath temperature, with and without the optimum 812 GHz LO power applied.

perhaps, the expression does not apply to small magnetic fields (it was derived from data taken in fields between 10 and 14 KG). Of course, it is possible that Eqn. 4.2 is wrong, considering that it was deduced from saturation rather than direct measurements. Regardless of the problem, it will be very interesting to repeat the heterodyne measurements with a modulatable laser sideband generator so that the system noise temperature and bandwidth can be obtained in the same experiment.

#### 4.6.3 Faraday Configuration Receiver

Shown in Fig 4.13 is a schematic diagram of the cryostat used to conduct Putley Mode heterodyne experiments in the Faraday configuration. The magnetic field is generated by a solenoid situated in the liquid helium bath. The cryostat has an indented cold plate that allows the detector to be mounted exactly in the center bore of the solenoid. Also shown in Fig. 4.13 is the receiver front-end. The InSb mixer is mounted across a 0.020 inch diameter circular waveguide. Since the axis of the waveguide is normal to  $\mathbf{B}$ , the mixer is in the Faraday configuration. The incoming radiation is coupled into the mixer with a conical feedhorn. The coupling can be optimized for any operating frequency with the adjustable backshort. The backshort is controlled with a novel cryogenic mechanism that was necessary because of the remote location of the mixer assembly. The near-infrared radiation is attenuated with a black polyethylene / quartz filter mounted on the liquid nitrogen cooled shield.

A preliminary test of this Putley-mode receiver was conducted at 625 GHz. Using a frequency multiplied klystron, a double-sideband system noise temperature of  $\sim 2000\text{K}$  was obtained at 4.2K and 4 KG. This result is considered preliminary since the local oscillator power was less than optimum. Much better results should be achievable using the laser LO. However, this test did afford an opportunity to demonstrate that the mixer response is greatly enhanced by cyclotron resonance absorption. To do this, a plot was made of the direct detection response to 625 GHz LO power versus magnetic field. This plot, shown in Fig. 4.14, displays two maxima. The maximum at the lowest value of magnetic induction is due to the ICR transitions, while the one at the higher induction is due to the CCR transition. This demonstrates that the magnetic field may have even more effect on these thin, waveguide mounted mixers than it had on the thicker direct detectors of Sec. 4.1.

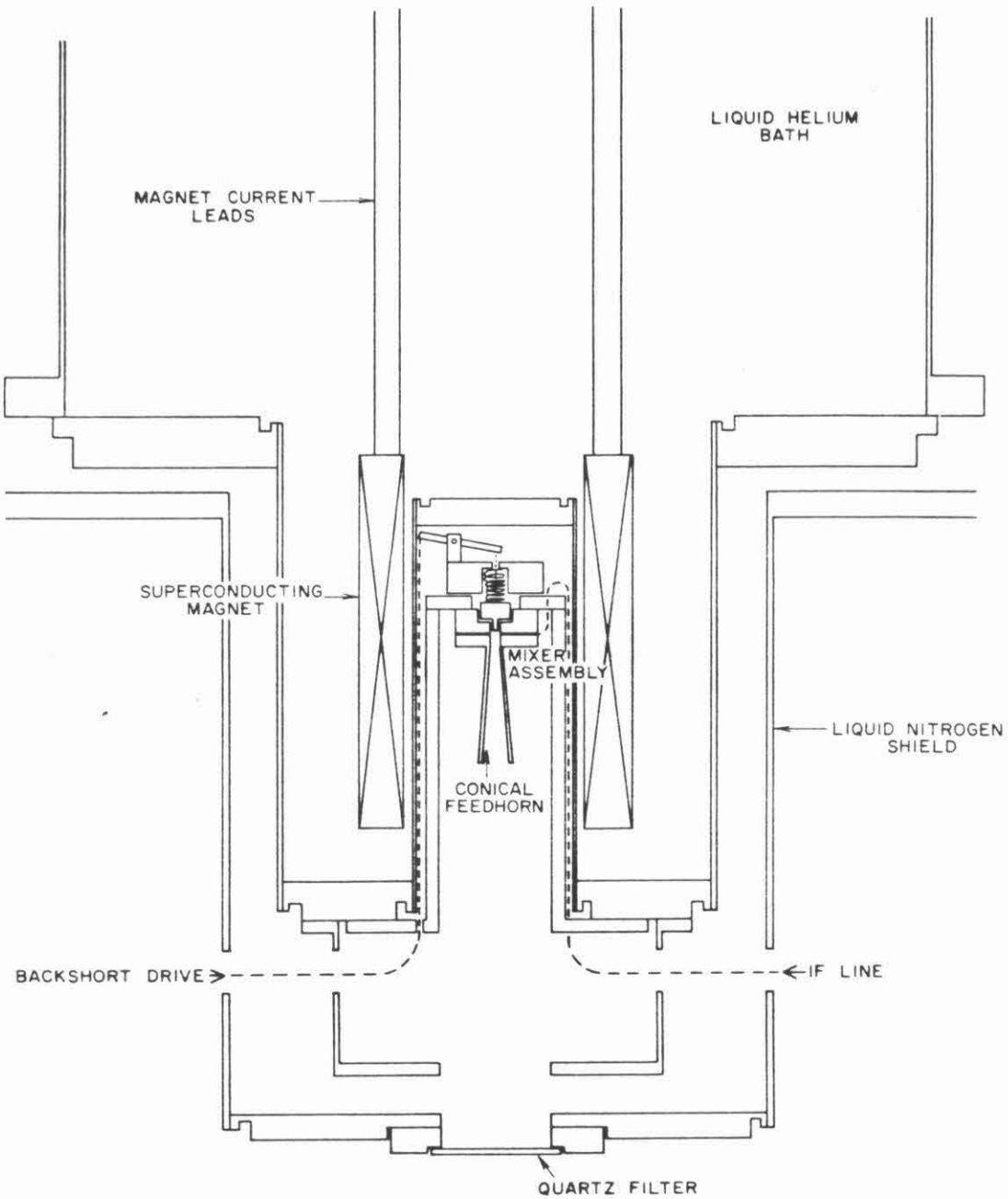


Figure 4.13: Schematic diagram of Putley mode heterodyne receiver with the InSb mixer in the Faraday configuration.



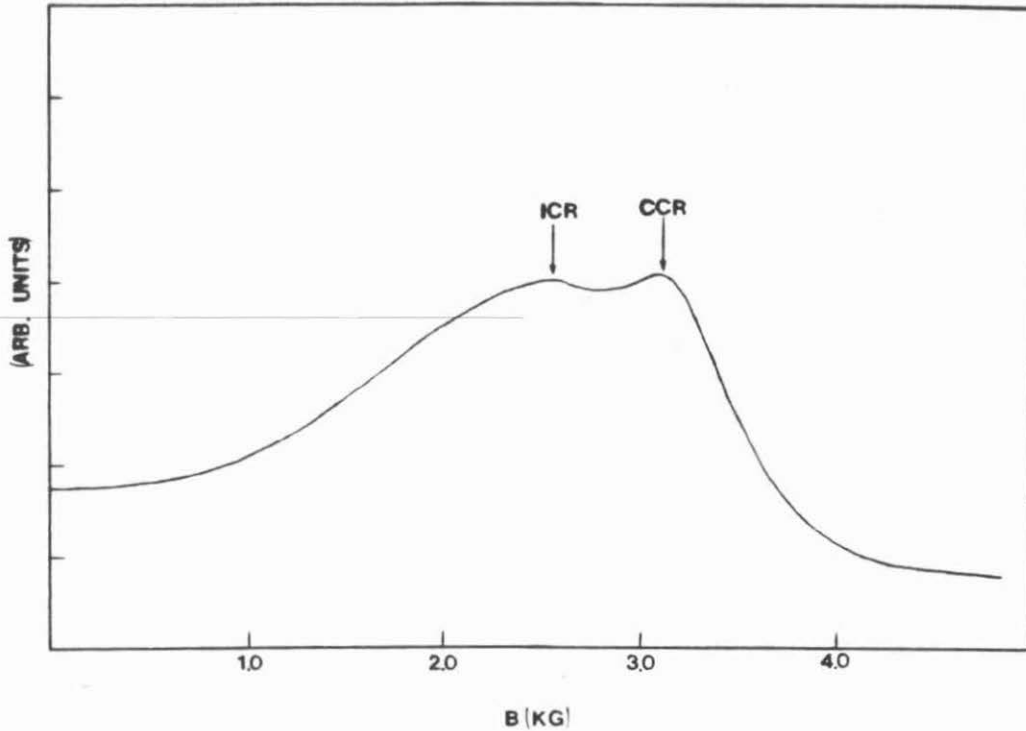


Figure 4.14: Response of InSb mixer at 4.2K and in the Faraday configuration to 625 GHz local oscillator power.

#### 4.6.4 The Future of the Putley Mode Mixer

The above results clearly demonstrate that the cyclotron resonance photoresponse in InSb can be used as the basis for a very sensitive heterodyne receiver in the submillimeter wavelength region between  $370 \mu\text{m}$  and  $600 \mu\text{m}$ . Judging from the excellent performance, it seems safe to say that this receiver should be extremely useful in the near future for tasks requiring high sensitivity but only modest IF bandwidth. Certainly an ideal application of this receiver is the identification of the fundamental rotation lines of the diatomic hydrides in dark-cloud regions of the interstellar medium.

Judging from the direct detection results of Sec. 4.1, the excellent performance obtained above in the Voigt configuration should be attainable up to frequencies of at least 1200 GHz. Therefore, the next experiment that should be conducted is a laser heterodyne test near this frequency. It so happens that there are several strong far-infrared laser lines in this region. Certainly a good candidate is the  $237 \mu\text{m}$  line of difluoromethane. With careful design, it should be possible to get magnetic fields on the mixer near the saturation value of the rare earth cobalt material,  $\sim 8.5 \text{ KG}$ . This corresponds to a CCR frequency of about 1700 GHz.

Once the maximum field attainable with the permanent magnets is determined, the Faraday configuration receiver can be incorporated to test the Putley mode mixer at higher fields. The solenoid shown in Fig. 4.12 can yield a maximum field of 20 KG. This corresponds to a CCR wavelength of  $75 \mu\text{m}$ . Suffice it to say that there is a lot of interesting work to be done on the Putley mode mixer. The pioneering demonstration presented here is only the beginning.

## Appendix A: Obtaining Impurity Concentrations from Hall Data

### A.1 Theory

The simplest way to find the impurity concentrations in semiconductor samples is by statistical analysis of Hall data. The basic procedure is to measure the carrier concentration as a function of temperature and to fit these data with an equation that relates all of the relevant concentrations in thermal equilibrium. There are several conditions that greatly facilitate this procedure. The temperature in the Hall experiment should be low enough that the sample is extrinsic; i.e., the vast majority of carriers is contributed by the impurity levels rather than bands. In addition, the impurities should be isolated (i.e., no overlap of adjacent impurity wavefunctions) and shallow (i.e., ionization energy much less than the band gap), and the impurity state structure and degeneracy should be known *a priori*. The binding energies remain as unknowns to be found in the analysis.

As an example of the procedure, consider an n-type sample containing shallow impurities and cooled to low enough temperatures to be extrinsic. Under these conditions, one can assume that all of the acceptors are ionized and that the following equation applies to the distribution of electrons amongst available states,

$$N_d - N_a = n_c + n_d = \Delta N \quad (\text{A.1})$$

where  $N_d$  and  $N_a$  are the total donor and acceptor concentrations, respectively,  $n_c$  is the concentration of electrons in the conduction band,  $n_d$  is the concentration of electrons bound to donors and  $\Delta N$  is the excess donor concentration. By assuming that the donor levels are only singly occupied and that the degeneracy is two for spin, it can be shown [Ashcroft and Mermin 1976],

$$n_d = \frac{N_d}{1 + 1 / [p_i \sum_i \exp(-\beta(E_i - \mu))]} \quad (\text{A.2})$$

where  $E_i$  is the binding energy of the  $i$ th state,  $\mu$  is the chemical potential,  $\beta = 1/kT$  and  $p_i$  is the degeneracy of the  $i$ th level. A great simplification of this expression occurs when the ground state lies well below all excited states, as is true in hydrogenic impurities. One can then re-write Eqn. A.2 as,

$$n_d = \frac{N_d}{1 + 1/2 \exp[\beta(E_1 - \mu)]} \quad (\text{A.3})$$

where  $E_1$  is the ground-state energy. The final relation we need is one for the conduction-band electron concentration. Assuming sufficiently low doping concentration and/or temperature that the conduction electrons are described adequately by classical statistics [Ashcroft and Mermin 1976],

$$n_c = N_c \exp(\mu / kT) \quad (\text{A.4})$$

where  $N_c = 2(2\pi m^* kT)^{3/2} / h^3$ . Combining Eqns. A.1, A.3 and A.4 and eliminating  $\mu$ , one obtains

$$N_d = (\Delta N - n_c) \left[ 1 + 1/2 \frac{N_c}{n_c} \exp(E_1 / kT) \right]. \quad (\text{A.5})$$

This is the transcendental equation that is used to find  $N_d$  once  $\Delta N$  and  $n_c(T)$  are determined by Hall analysis at different temperatures.

Unfortunately, none of the InSb samples studied in this thesis were directly amenable to the above procedure because the donors were not isolated. This was evident in the near independence of the Hall constant with temperature down to 4.2K. As discussed in Sec. 2.3 the donor wavefunction overlap responsible for this behavior is greatly reduced in the presence of quantizing magnetic fields. If we apply a field large enough to induce complete donor isolation, then

a simple impurity analysis is again possible. However, the magneto-band structure of Fig. 2.1 indicates that the (0,0,0,+) ground state does not lie well below all of the excited states associated with the  $N=0^+$  Landau level. Furthermore, this state is now non-degenerate due to spin splitting. Therefore, an accurate analysis should include more than one level in the sum of Eqn. A.2., but can assume  $p_i = 1$  provided that  $g^* \mu_B \gg kT$ . In addition, the analysis must apply the Landau effective density of states [Putley 1966],  $N_B = \sqrt{2\pi m^* kT e B} / (\hbar^2 c)$ , instead of  $N_c$  in Eqn. A.4. This expression for  $N_B$  assumes that  $\hbar\omega_c \gg kT$  (extreme quantum limit) and  $g^* \mu_B \gg kT$  so that only the  $N=0^+$  Landau sub-band is appreciably occupied. With all of these changes and the assumption of classical statistics in the  $N=0$  Landau level, one can write the high magnetic field analog of Eqn. A.5,

$$N_d = (\Delta N - n_c) \left[ 1 + \frac{N_B}{n_c \sum_i \exp(-E_i / kT)} \right] \quad (A.6)$$

Finding  $N_d$  now requires solving coupled transcendental equations, one for each impurity level included in the sum.

In the past, most workers have applied Eqn. A.6 with only the ground state considered. For example, Putley made this approximation and justified it by showing that the resulting impurity concentration,  $N_d + N_a$  was close to that found by an analysis of the 20K experimental conductivity using the Brooks-Herring formula. Initially I adopted the same approximation but found that it yielded impurity concentrations much different than those found with the ~20K conductivity analysis. This was particularly true for our coveted 4002 material. Therefore, I introduced an approximation that included the first excited state (viz. (0,1,0,+)) but assumed it, for simplicity, to be equal in energy to the ground state. This leads to,

$$N_d = (\Delta N - n_c) [1 + \frac{1}{2} N_B \exp(E_1/kT)]. \quad (A.7)$$

This expression gave much better agreement with the conductivity results. It is also a much more reasonable approximation than Putley's considering the close proximity of the  $(0,0,0,+)$  and  $(0,\bar{1},0,+)$  levels.

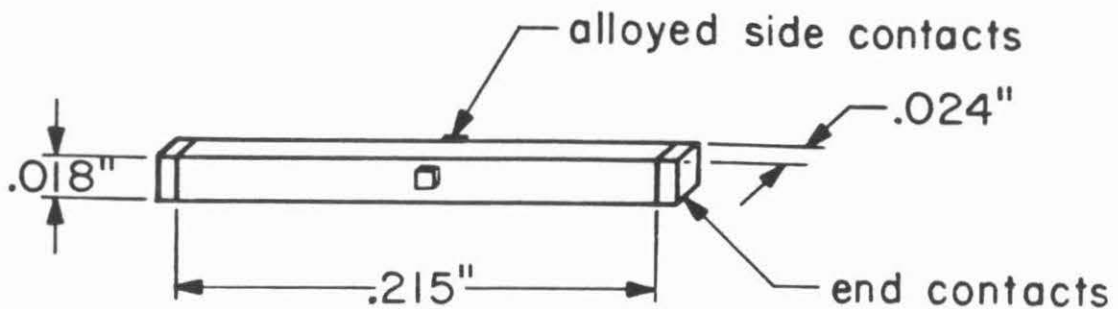


Figure A.1: InSb Hall sample.

## A.2 Hall Experiment

The cryogenic setup used for the Hall experiment is that shown in Fig. C.1. Special Hall bars were made for the 4002, 4177 and 4190 materials. The geometry of these samples is shown in Fig. A.1. Current was applied through the large end contacts and the Hall voltage,  $V_H$  was measured at the much smaller side contacts. The relationship between the parameters is [Putley 1960],

$$R_H = \frac{V_H}{I B h} \quad (A.8)$$

where  $B$  is the magnitude of the magnetic field and  $h$  is the thickness of the bar along  $B$ . For crystalline materials in which the the Fermi surface is closed and in which the carriers contributing to electrical current occupy only one band, the Hall coefficient  $R_H$ , is simply related to the carrier concentration,  $n_c$ , through the well-known relation [Ashcroft and Mermin 1976],

$$R_H = \frac{\gamma}{n_c e c} \quad (\text{A.9})$$

where  $\gamma$  is a parameter that depends on the scattering mechanism, the magnetic field strength and the electron statistics. For example, non-degenerate statistics and magnetic fields satisfying  $\omega_c \tau \ll 1$  ( $\tau$  is the momentum relaxation time) lead to  $\gamma=3\pi/8$  for acoustical electron scattering and  $\gamma=315\pi/512$  for ionized impurity scattering [Putley 1960]. For magnetic fields satisfying  $\omega_c \tau > 1$  but  $\hbar\omega_c < kT$ , the parameter  $\gamma$  goes to unity, independent of scattering and statistics.

The first quantity obtained from the Hall measurements was the excess donor concentration,  $\Delta N$ . The Hall measurements were made at about 60K and in magnetic fields of about 2 KG. Under these conditions,  $\gamma \approx 1.0$ , but  $\hbar\omega_c \ll kT$ . Therefore, we can write  $\Delta N = n_c = 1/(R_H e c)$ . The results for the three InSb materials are given in Table 2.1.

Knowing  $\Delta N$ , Eqn. A.7 was solved using the results of Hall measurements made under magnetic freeze-out conditions. For example, the 4002 Hall sample was subjected to temperatures of  $T=4.6\text{K}$  and  $T=3.2\text{K}$  and to a field of 4 KG. For any combination of these conditions,  $\gamma \approx 1.0$ . The resulting values of  $n_c$  were then substituted into Eqn. A.8 and the later was plotted against binding energy (recall that the binding energy does not vary with temperature). The graphical solution is demonstrated in Fig. A.2. Also shown in Fig. A.2 is the result of the same procedure for  $B=3$  KG. Notice that the binding energy changes but that the solution for  $N_d$  is practically the same as obtained for  $B=4$  KG. The

corresponding solutions for the 4177 and 4190 materials are given in Table 2.1.

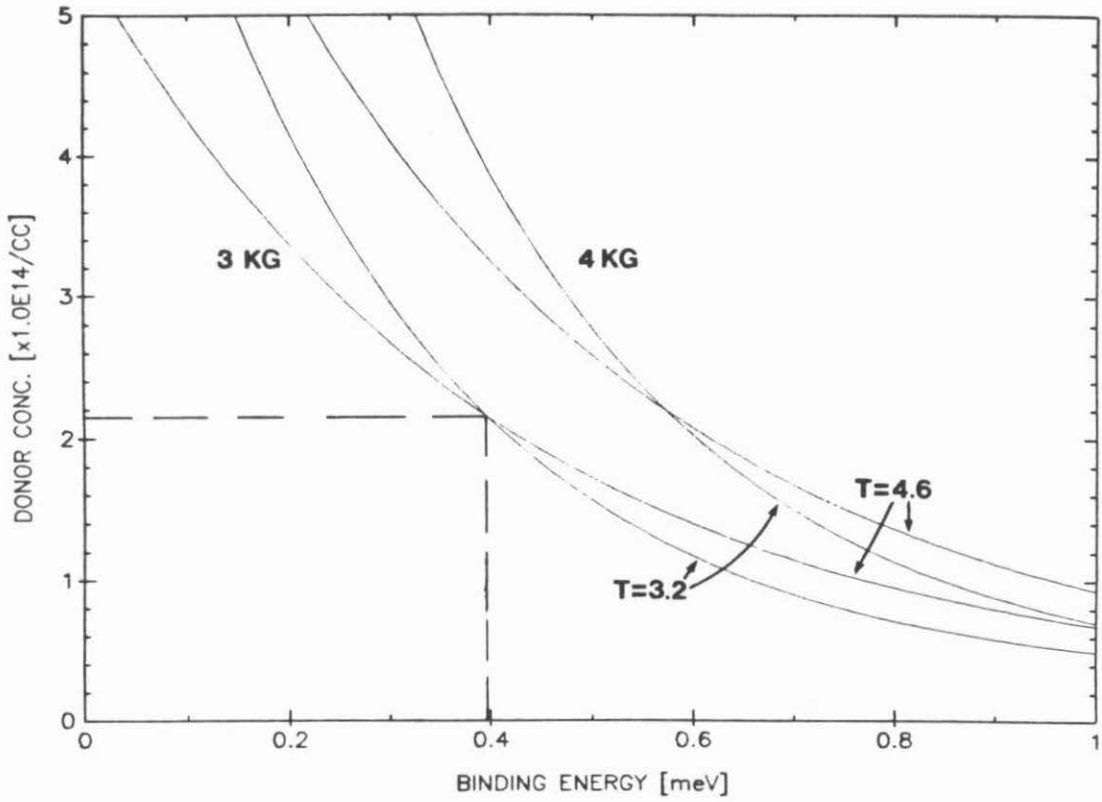


Figure A.2: Graphical solution of the donor concentration and binding energy for the 4002 Hall sample in two different magnetic fields.



## Appendix B: Dynamic Resistance Measurement Technique

On many occasions in this thesis work, it was necessary to measure the dynamic resistance,  $Z = dV/dI$ , at a particular bias point  $(I_0, V_0)$ . The technique described here is very useful for obtaining  $Z$  for highly non-ohmic samples like the liquid helium cooled InSb, SIS junctions etc. The technique involves applying the required DC term,  $I_0$ , plus a much smaller sinusoid probe,  $i \sin \omega t$ , both from a very high impedance source. Under these conditions, the voltage across the sample is,

$$V(t) = V_0 + \left( \frac{dV}{dI} \right)_{I_0} i \sin \omega t + \frac{1}{2} \left( \frac{d^2V}{dI^2} \right)_{I_0} i^2 \sin^2 \omega t + \dots \quad (\text{B.1})$$

Now  $\sin^2 \omega t = \frac{1}{2} - \frac{1}{2} \cos 2\omega t$ . Therefore, assuming that  $i$  is sufficiently small,  $dV/dI$  can be determined quite accurately by measuring the voltage component that is in-phase with the probe current. This is accomplished with the setup shown schematically in Fig B.1. The bandpass filter shown must be centered at  $\omega$  and must have  $Q \gg 1$  to filter out all higher harmonics. This follows from the fact that the lock-in amplifier multiplies the input with a synchronous square-wave. The measurement is calibrated by replacing the sample with a 1% tolerance resistor of resistance comparable to  $dV/dI$ .

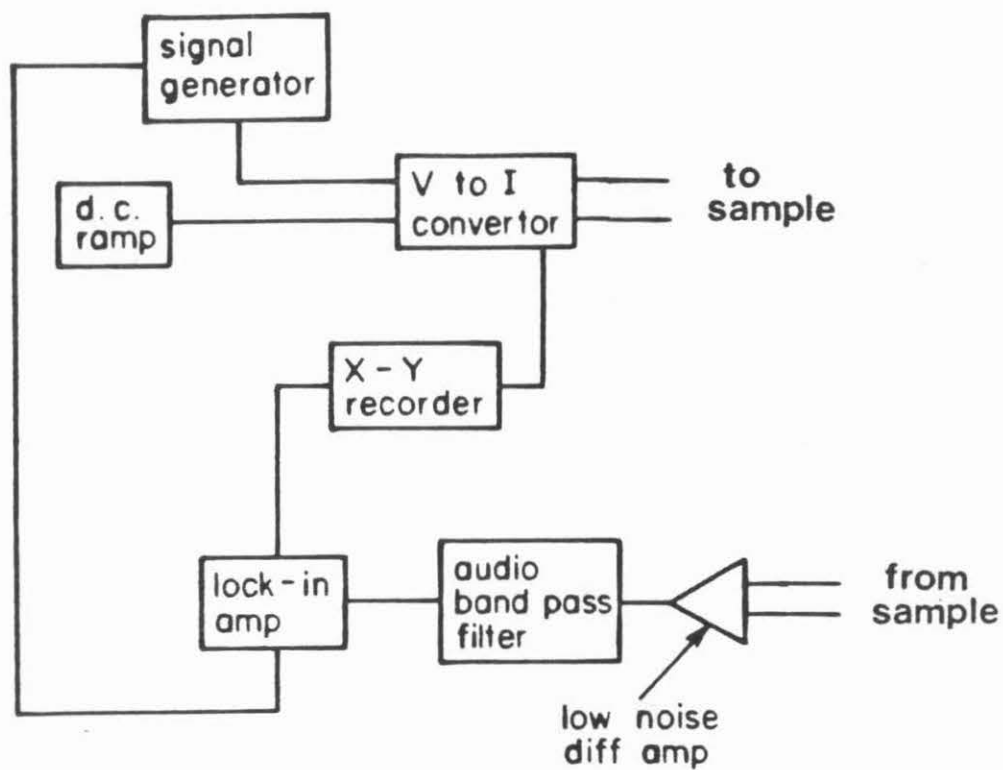


Figure B.1: Block diagram of electronics to measure dynamic resistance

### Appendix C: Fourier Transform Spectrometer

All of the absorption and response spectra presented in this thesis were obtained with the Fourier transform spectrometer set-up shown in Fig. C.1a and C.1b. The spectrometer consists of a RIIC 720 Michelson interferometer, a light pipe and condensing cone assembly to couple the radiation down into a liquid helium immersion cryostat, signal processing electronics, a minicomputer, and a video terminal with graphics capability. The interferometer is a symmetric design (both arms optically equivalent) with continuous mirror scan, off-axis collimating mirror for the source and stretched mylar beamsplitter. It is discussed in more detail by Bell [1972].

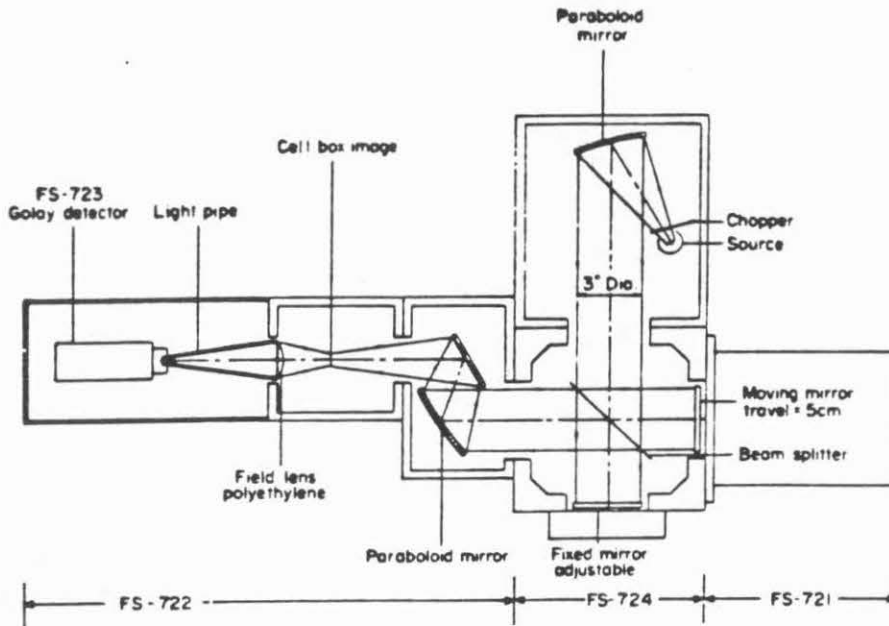


Fig. C.1a: The RIIC FS-720 Michelson interferometer, after Bell [1972].

Detectors are mounted across the exit aperture of a gold-plated copper condensing cone.\* They are situated in the center of a superconducting solenoid that generates a uniform magnetic field parallel to the axis of the cone. The cone is coupled to the interferometer with a light pipe made of thin-walled stainless steel to minimize heat flow. The entire assembly is isolated from the liquid helium bath by a coaxial, hermetic stainless steel tube. Before insertion into the dewar, this tube is evacuated and then back-filled with helium exchange gas that cools the detector and the cone. After a little practice, I determined an amount of gas ( $\sim 100$  mm Hg) that cooled the detectors very close to the bath temperature but caused little extra boil-off of the liquid helium.

Because of the slow scan speeds of the RIIIC 720 and the low maximum wavenumbers of interest, the interferogram signal spectrum determined by the mirror modulation is below 5Hz. Since the  $1/f$  noise from the detectors and  $1/f$  noise from the preamp are both large in this range, it was decided to chop between two different sources at a much higher frequency and later down-convert the signal after much amplification. The two sources were extended Eccosorb sheets, one at ambient temperature and the other cooled by liquid nitrogen inside a polyethylene wash bottle placed at the focus of the collimating mirror.

After demodulation of the chopped signal using a lock-in amplifier, the interferogram spectrum is processed by a 6-pole low-pass Butterworth filter with cutoff somewhat below the Nyquist frequency ( $1/2 \times$  chopping frequency). The post-filtered signal is digitized in real time at points determined by the fringes of a Moire grating that rides with the traveling mirror. At the end of each scan, the sampled interferograms are numerically processed by the minicomputer.

---

\* manufactured nicely by Gamma-f Corp. of Torrance, Calif.

This processing includes DC subtraction, rearrangement, fast Fourier transformation, and phase correction for asymmetric sampling about zero path difference. The resulting cosine transform is the detector response spectra multiplied by the electronic gain. Successive spectra are co-added to enhance the signal to noise ratio.

This spectrometer is designed for low resolution material and detector studies. The extended sources are made large enough to over-illuminate the condensing cone acceptance pattern. This causes the radiation at the exit aperture to be Lambertian over the whole hemisphere. The energy throughput,  $A\Omega$ , is thus maximum within the limits imposed by the cone. This is not true in grating spectrometers and would not be true in this instrument if the source was the standard high pressure mercury discharge lamp because the size of the FIR emitting region in these lamps is relatively small. Therefore, a given detector will generate a larger signal in this instrument than in the others. For detectors that are not background radiation noise limited, this means the signal-to-noise ratio will be better and fewer spectra will have to be added to achieve a particular accuracy.

The penalty for maximizing the throughput is a reduction in the ultimate resolution. Specifically, the measured spectrum becomes the convolution of the true spectrum with both a sinc function due to the finite travel of the mirror and a rectangle function due to the extended source [Bell 1972]. The width of this rectangle is proportional to the solid angle subtended at the collimator by the effective area of the source. I measured this angle in the geometrical optics limit using a visible source at the bottom of the cone and back-projecting the light through all the interferometer optics. Knowing this information, I always conducted the experiments so that the resolution was limited by the finite travel of the mirror. Of course, in the far-infrared (e.g.,  $\sigma < 20 \text{ cm}^{-1}$ ) the antenna

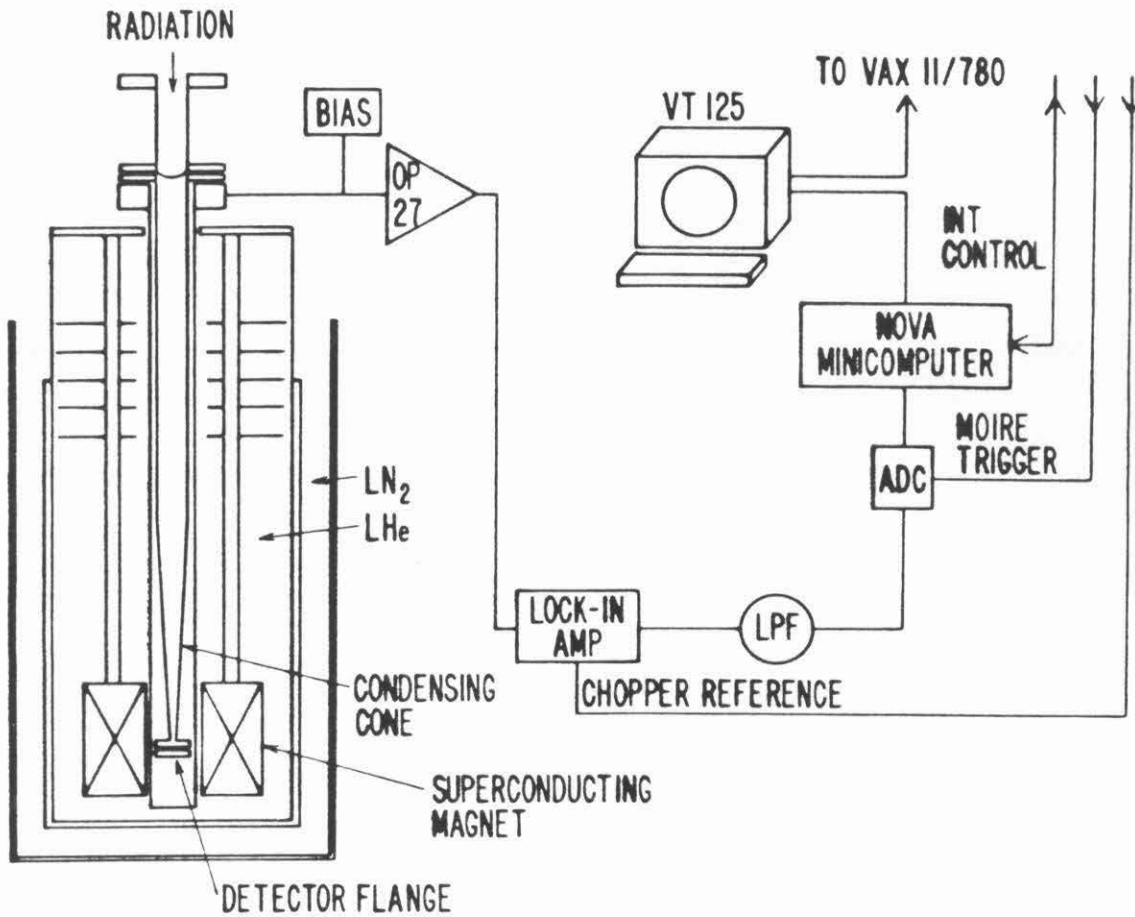


Figure C.1b: Block diagram of liquid helium cryostat and signal processing electronics of the Fourier transform spectrometer designed by the author.

pattern of the cone will develop diffraction sidelobes and the characterization of the spectrometer would be much more complicated [Woody 1975].

## Appendix D: Ultra-low Noise Preamp for the Putley-mode Detector

### D.1 Introduction

We have seen that the properly designed Putley mode detector can have a dynamic resistance of about 1 K $\Omega$  and a bandwidth of 5 MHz or more. These characteristics make it particularly difficult to design a preamplifier that causes negligible degradation of the detector signal to noise ratio over the entire detector bandwidth. This appendix presents a relatively simple room-temperature preamp design that satisfies both the low-noise and wideband requirements.

Low-noise preamplification of high impedance detectors is usually accomplished with field effect transistors. Silicon JFETs are preferential for frequencies below about 10 MHz because they display much less 1/f noise in this region than the alternative devices: Si MOSFETs or GaAs MESFETs. The desirable feature of FETs, in general, is the low equivalent-input rms current noise,  $I_n$ , compared to bipolar devices [Motchenbacher and Fitchen 1973]. This leads to a phenomenally small noise factor when the source dynamic resistance satisfies,  $R_s \sim R_{opt} = E_n / I_n$ , where  $E_n$  is the equivalent-input rms noise voltage. For JFETs with relatively small  $E_n$ , typical values of  $R_{opt}$  are between 100 K $\Omega$  and 1 M $\Omega$ . When the source impedance is below this range, one can still get close to optimum noise factor by connecting many FETs in parallel. This technique is used in the present design.

In addition to the noise factor, the other important consideration in coupling cryogenic sources to JFETs is the total input capacitance,  $C_i$ . Ideally this capacitance should be small enough that the frequency response is limited by the detector bandwidth, not by the  $R_s C_i$  time constant. With this in mind, one usually designs for a gate-drain bias voltage somewhat below the "breakpoint" value [Siliconix AN74-4 app. note]. The breakpoint voltage is a compromise,



above which the gate leakage-current shot noise increases significantly and below which the gate-drain capacitance,  $C_{gd}$ , increases roughly as  $V_{gd}^{-1/2}$ . Similarly, the gate-source voltage ( $V_{gs}$ ) is usually set so that the drain current is slightly greater than  $0.1 \times I_{DSS}$ . Well above this value of drain current, the gate-source capacitance,  $C_{gs}$ , rises sharply and the device begins to degrade due to overheating effects. Well below this value, the transconductance is relatively small and the noise factor is much greater than the optimum.

With these bias conditions, the gate-source capacitance is typically much greater than the gate-drain capacitance. Despite this fact, most low noise preamp designs configure the JFETs in the common source configuration. One successful design, the "mismatched pair" [Robinson 1974], has a second stage common emitter with negative feedback to decrease the load resistance of the FET, thereby decreasing the gain and the concomitant Miller effect. Another well-known design, the "cascode" [ibid], uses a common base or gate as the second stage to, again, reduce the Miller effect at the FET. Both designs present the full value of  $C_{gs}$  and at least one unit of  $C_{gd}$  to the input.

## D.2 Preamp Design

This section presents the design that has much less input capacitance than mismatched pair or cascode amplifiers of comparable noise. The trick is to use the input JFET in the common drain (source follower) configuration and use a superior quality bipolar transistor for the second stage. With the bipolar connected common emitter and with as large as possible source bias impedance, it is not hard to achieve close to unity voltage gain with the FET and thereby bootstrap out most of  $C_{gs}$ . The only difficulty is in finding a bipolar that has a very low noise figure when coupled to the small output dynamic resistance of the follower,  $Z \sim 1/g_m$ , where  $g_m$  is the FET transconductance.

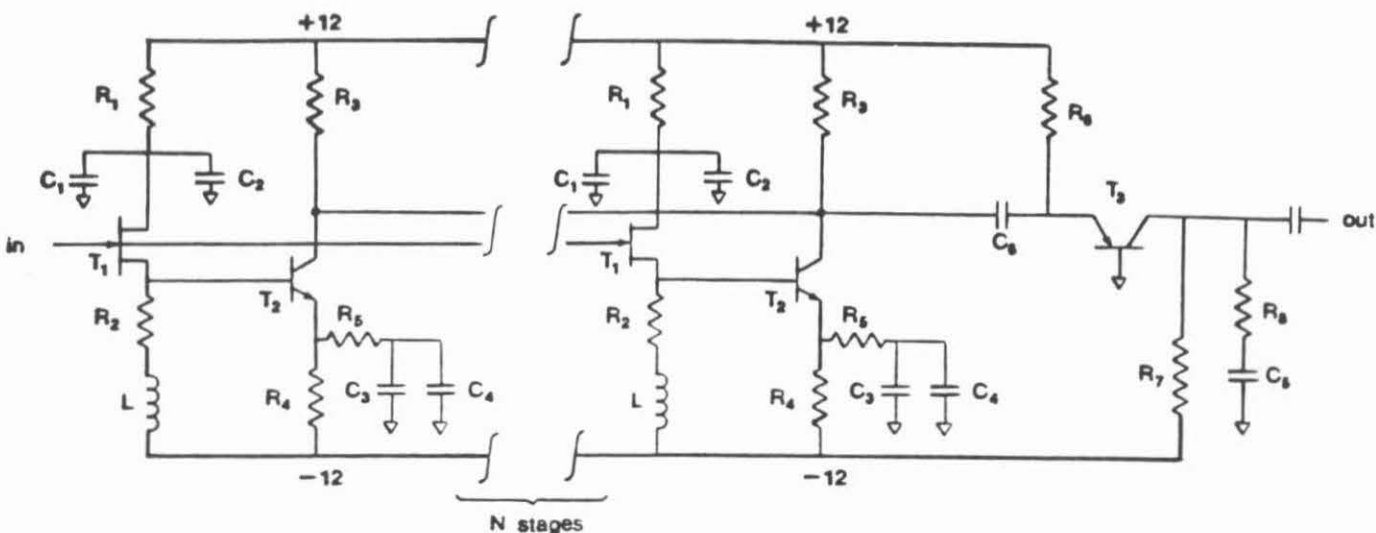


Figure D.1: Schematic diagram of room temperature, ultra-low noise, high-impedance preamp for the Putley-mode detector

The schematic diagram of the circuit design is shown in Fig. D.1. It consists of  $N$  parallel FET-bipolar pair stages where  $N$  is chosen to make the noise factor suitably small. Note that  $T_2$  has a small degree of emitter degeneration. This enhances the bandwidth and also improves the performance of the FET source follower. The signal currents from the  $N$  parallel stages are summed at the emitter of a common-base third stage and the output voltage is generated across the load resistor,  $R_8$ . Neglecting the noise from bias resistors and stages after  $T_2$ , the theoretical input rms noise generators at midband frequencies are found to be [Motchenbacher and Fitchen 1973],

$$E_n \approx N^{-1/2} \left[ E_1^2 + 4kT(R_b + R_5) + \frac{2eI_c}{\beta g_m^2} + \frac{2(kT)^2}{eI_c} \right]^{1/2} \quad (D.1)$$

$$I_n \approx \left[ N \cdot 2eI_g \right]^{1/2} \quad (D.2)$$

$$C_i \approx N C_{gd} \quad (D.3)$$

where  $k$  is Boltzmann's constant,  $T$  is the transistor operating temperature,  $E_1$  is the FET rms noise voltage,  $I_g$  is the FET gate leakage current, and  $R_b$ ,  $I_c$  and  $\beta$  are the bipolar transistor base parasitic resistance, collector current and DC current gain, respectively. In deriving Eqn. D.1 it has been assumed that the voltage gain of the first stage is unity. The first term of Eqn. D.1 represents the FET channel thermal noise, and can be approximated by the well-known expression  $\overline{E_1^2} \approx 2/3(4kT/g_m)$  [van der Ziel 1962]. The last two terms represent the base-emitter junction shot noise and the base-collector junction shot noise respectively. It is simple to show that the contribution of these two terms is minimized for a collector current  $I_c = kTg_m\beta^{3/2}/e$ . The resulting equivalent input noise voltage is

$$E_n \approx N^{1/2} \left[ \frac{2}{3} \frac{4kT}{g_m} + 4kT(R_b + R_5) + \frac{4kT}{g_m\beta^{3/2}} \right]^{1/2} \quad (D.4)$$

This expression shows clearly that if  $R_b + R_5 \ll 1/g_m$  and  $\beta \gg 1$ , then the total noise is degraded little by the second stage.

### D.3 Preamp Performance

An eight stage version of this circuit was constructed using the Siliconix J309 for the first stage. Under the given operating conditions, this device has the following characteristics:  $g_m \approx .014$  mho,  $C_{gd} \approx 2.5$  pF,  $C_{gs} \approx 6$  pF,  $E_1 \approx 1.1$  nV/Hz<sup>1/2</sup> and  $I_1 \approx 1.0$  fA/Hz<sup>1/2</sup>. The second stage bipolar transistor is a Rohm 2SD786 which has the following characteristics:  $R_b \approx 4$   $\Omega$ ,  $\beta \approx 200$  and  $f_T \approx 60$  MHz at  $I_c = 5$  mA. The other circuit elements are as follows:  $T_3$  is a 2SB737,  $R_1 = 750$   $\Omega$ ,  $R_2 = 1.3$  K $\Omega$ ,  $R_3 = 1.2$  K $\Omega$ ,  $R_4 = 2.4$  K $\Omega$ ,  $R_5 = 15$   $\Omega$ ,  $R_6 = 1.2$  K $\Omega$ ,  $R_7 = 750$   $\Omega$ ,  $R_8 = 150$   $\Omega$ ,  $C_1 = C_3 = 1$   $\mu$ F,  $C_2 = C_4 = .01$   $\mu$ F ( $C_2$  is preferably a chip capacitor),  $C_5 = 0.1$   $\mu$ F,  $C_6 = 1$   $\mu$ F,  $L = 33$  mH. The overall

amplifier performance is  $E_n \approx .42 \text{ nV/Hz}^{1/2}$ ,  $I_n \approx 2.8 \text{ fA/Hz}^{1/2}$ ,  $C_i \approx 28 \text{ pF}$ . This voltage noise is only about 10% higher than that expected from the FETs alone. When operating into a reasonably high input impedance ( $\gtrsim 1 \text{ K}\Omega$ ) video amp, the mid-band voltage gain of this preamp is 46. The lower 3 dB rolloff frequency is 100 KHz. For source impedances  $\lesssim 400 \Omega$ , the upper 3 dB rolloff frequency is 15 MHz. This rolloff is caused by the rather large emitter diffusion capacitance of the 2SD786s.

This design can be easily adapted to suit other difficult preamp applications. One adaptation would be a one-stage version for very high-impedance cryogenic sources like liquid helium cooled germanium. If the detector were coupled to such a preamp with triax cable, the cable capacitance could then be bootstrapped out by connecting the center shield to the source lead of  $T_1$ . This design is potentially a lot simpler than a liquid helium cooled FET preamp. However, one would probably want to use both an FET with a much larger room-temperature  $g_m/C_{gd}$  ratio than the J309 and a second stage with a higher  $f_T$  than the 2SD786.

### References

- B.L. Altshuler and A.G. Aronov, *Solid State Comm.*, **30**, 115 (1979).
- F. Arams, C. Allen, B. Peyton and E. Sard, *Proc. IEEE*, **54**, 612 (1966).
- V.V. Arendarchuk, E.M. Gershenzon and L.B. Litvak-Gorskaya, *Sov. Phys. Semicond.*, **7**, 89 (1973).
- N.W. Ashcroft and N.D. Mermin, *Solid State Physics* (Saunders College, Philadelphia, 1976), p. 16.
- R.J. Bell, *Introductory Fourier Transform Spectroscopy* (Academic, New York, 1972), Chap. 19.
- H.A. Bethe and E.E. Salpeter, in *Handbuch der Physik*, edited by S. Flugge (Springer, Berlin, 1957), Vol. 35, p. 418.
- G.A. Blake, J. Keene and T.G. Phillips, *Astrophys. J.*, in press (1985).
- G.A. Blake, Caltech, private communication (1984).
- F.J. Blatt, *J. Phys. Chem. Solids*, **1**, 262 (1957).
- H.J.A. Bluysen, J.C. Maan, L.J. van Ruyven, F. Williams and P. Wyder, *Solid State Comm.*, **25**, 895 (1978).
- Max Born and Emil Wolf, *Principles of Optics* (Pergamon, New York, 1975), p. 628.
- R. Bowers and Y. Yafet, *Phys. Rev.*, **115**, 1165 (1959).
- P.R. Bratt, in *Semiconductors and Semimetals*, edited by R.K. Willardson and A.C. Beer (New York, Academic, 1977), Vol. 12, p. 39.
- Peter Bratt, Santa Barbara Research Center, private communication (1983).
- H. Brooks, in *Advances in Electronics and Electron Physics*, Vol. 7, ed. by L. Marton (Academic, New York, 1955), p. 85.
- E.R. Brown, *J. Appl. Phys.*, **55**, 213 (1984).
- E.R. Brown, *J. Appl. Phys.*, **57**, 2361 (1985).
- M.A.C.S. Brown and M.F. Kimmitt, *Brit. Comm. and Elect.*, **10**, 608 (1963).

- M.A.C.S. Brown and M.F. Kimmitt, *Infrared Phys.*, **5**, 93 (1965).
- C. Cohen-Tannoudji, B. Diu and F. Laloe, *Quantum Mechanics* (Wiley, New York, 1977), Vol. 2, p. 1295.
- E. M. Conwell, *Solid State Physics* (edited by F. Seitz et al.), Supplement 9, Academic Press, New York (1967).
- G. Dresselhaus, A.F. Kip and C. Kittel, *Phys. Rev.*, **98**, 556 (1955).
- R.C. Dynes, T.H. Geballe, G.W. Hull Jr. and J.P. Garno, *Phys. Rev. B*, **27**, 5188 (1983).
- Bob Dynes, Bell Labs, private communication (1983).
- J.W. Fleming, in *Modern Aspects of Microwave Spectroscopy*, edited by G.W. Chantry (Academic Press, London, 1979), p. 257.
- H. Frohlich and B.V. Paranjape, *Proc. Phys. Soc. B*, **69**, 21 (1956).
- E. Gornik, T.Y. Chang, T.J. Bridges, V.T. Nguyen, J.D. McGee and W. Muller, *Phys. Rev. Lett.*, **40**, 1151 (1978).
- M. Hass and B.W. Henvis, *J. Phys. Chem. Solids*, **23**, 1099 (1962).
- F. Herman, C.D. Kuglin, K.F. Cuff and R.L. Kortum, *Phys. Rev. Lett.*, **11**, 541 (1963).
- J.D. Jackson, *Classical Electrodynamics* (Wiley, New York, 1975), p. 296.
- B. Jensen, *Ann. Phys.*, **95**, 229 (1975).
- E.J. Johnson and D.H. Dickey, *Phys. Rev. B*, **1**, 2676 (1970).
- R.C. Jones, *J. Opt. Soc. Am.*, **43**, 1 (1953).
- H. Kahlert and G. Bauer, *Phys. Rev. B*, **7**, 2670 (1973).
- E.O. Kane, *J. Phys. Chem. Solids*, **1**, 249 (1957).
- R. Kaplan, *J. Appl. Opt.*, **6**, 685 (1967).
- R. Kaplan, *Phys. Rev.*, **181**, 1154 (1969).
- Jocelyn Keene, Caltech, private communication (1984).
- M.A. Kinch and B. V. Rollin, *Brit. J. Appl. Phys.*, **14**, 672 (1963).

- M.A. Kinch, Brit. J. Appl. Phys., **17**, 1257 (1966).
- M.A. Kinch, App. Phys. Lett., **12**, 78 (1968).
- R.H. Kingston, *Detection of Optical and Infrared Radiation*  
(Springer-Verlag, Berlin, 1978), Sec. 7.5.
- Sh.M. Kogan, Sov. Phys.-Solid State, **4**, 1813 (1963).
- J.D Kraus, *Radio Astronomy* (McGraw-Hill, New York, 1966), Chap. 7.
- F. Kuchar, E. Fantner and G. Bauer, J. Phys. C: Solid State Phys., **10**,  
3577 (1977).
- D.M. Larsen, J. Phys. Chem. Solids, **29**, 272 (1968).
- B. Lax and J.G. Mavroides, in *Solid State Physics*, **11**, 261 (1960).
- F. Low, J. Opt. Soc. Am., **51**, 1300 (1961).
- N.C. Luhmann Jr., in *Infrared and Millimeter Waves*, edited by K.J.  
Button (Academic, New York, 1982), Vol. 2.
- O. Madelung, *Introduction to Solid-State Theory* (Springer-Verlag,  
Berlin, 1978), Sec. 2.2.12.
- D. Marcuse, *Principles of Quantum Electronics* (Academic Press, New York,  
1980), Sec. 6.3.
- J. C. Mather, Appl. Opt., **21**, 1125 (1982).
- H.J.G. Meyer, Phys. Rev., **112**, 298 (1958).
- J.R. Meyer and F.J. Bartoli, Phys. Rev. B, **23**, 5413 (1981).
- Bill Micklethwaite, Cominco American Inc., private communication (1984).
- S. Morita, Y. Isawa, T. Fukase, S. Ishida, Y. Koike, Y. Takeuti and  
N. Mikoshiba, Phys. Rev. B (Rapid Comm.), **25**, 5570 (1982).
- C.D. Motchenbacher and F.C. Fitchen, *Low-noise electronic design*  
(Wiley, New York, 1973), pp. 219-221.
- W. Muller, E. Gornik, T.J. Bridges and T.Y. Chang, Solid State  
Elect., **21**, 1455 (1978).

- T. Murotani and Y. Nisida, *J. Phys. Soc. Jap.*, **32**, 986 (1972).
- T. Ohyama and E. Otsuka, in *Infrared and Millimeter Waves*, edited by K.J. Button (Academic, New York, 1983), Vol. B.
- E. Otsuka, in *Infrared and Millimeter Waves*, edited by K.J. Button (Academic, New York, 1980), Vol. 3, p. 347.
- R. Peierls, *Quantum Theory of Solids* (Oxford Univ. Press, Oxford, England, 1955).
- T.G. Phillips and K.B. Jefferts, *Rev. Sci. Inst.*, **44**, 1009 (1973).
- T.G. Phillips and D.P. Woody, *Annu. Rev. Astron. Astrophys.*, **20**, 285 (1982).
- T.G. Phillips and D.M. Watson, "The Large Deployable Reflector: Instruments and Technology," report by the NASA LDR Science Coordination Subcommittee, 1984.
- D. Pines, *Elementary Excitations in Solids* (Benjamin, New York, 1963), Chap. 3.
- E.H. Putley, *The Hall Effect and Related Phenomena* (Butterworths, London, 1960), Sec. 4.9.
- E.H. Putley, *J. Phys. Chem. Solids*, **22**, 241 (1961).
- E.H. Putley, *Proc. IEEE*, **51**, 1412 (1963).
- E. H. Putley, *Infrared Physics*, **4**, 1 (1964).
- E.H. Putley, in *Semiconductors and Semimetals*, edited by R.K. Willardson and A.C. Beer (Academic, New York, 1966), Vol. 2, Chap. 9.
- E.H. Putley, in *Semiconductors and Semimetals*, edited by R.K. Willardson and A.C. Beer (Academic, New York, 1977), Vol. 12, Chap. 3.
- E.H. Putley, *Infrared Phys.*, **18**, 371 (1978).
- V. Roberts and J.E. Quarrington, *J. Electronics*, **1**, 152 (1955).
- F.N.H. Robinson, *Noise and Fluctuations in Electronic Devices and*



*Circuits* (Clarendon Press, Oxford, 1974), Chap. 11.

- H.P. Roeser, R. Wattenbach and P. van der Wal, " A 150 micron to 500 micron heterodyne spectrometer for airborne astronomy," Airborne Astronomy Symposium, NASA Conference Publication 2353 (1984).
- B.V. Rollin, Proc. Phys. Soc. (London), **77**, 1102 (1961).
- K. Seeger, *Semiconductor Physics* (Springer-Verlag, Berlin, 1982) Sec. 4.13
- R. Serber and C.H. Townes, Proc. of the First Inter. Conf. on Quantum Electronics, ed. by C.H. Townes (Columbia Univ. Press, N.Y., 1960).
- R.J. Sladek, Phys. Rev., **120**, 1589 (1960).
- A. van der Ziel, Proc. IEEE, **50**, 1808 (1962).
- S. Visvanathan, Phys. Rev., **120**, 379 (1960).
- A.N. Vystavkin, Yu.S. Gal'pern and V.N. Gubankov, Sov. Phys. Semicond., **1**, 1439 (1968).
- A.N. Vystavkin, V.N. Gubankov, V.N. Listvin and V.V. Migulin, Proc. Polytech. Inst. Brooklyn Conf. Submillimeter Waves (Polytechnic Press, New York, 1971), vol. 20, p. 321.
- R.F. Wallis and H.J. Bowlden, J. Phys. Chem. Solids, **7**, 78 (1958).
- A.K. Walton and J.C. Dutt, J. Phys. C : Sol. State Phys., **10**, L29 (1977).
- J.J. Whalen and C.R. Westgate, IEEE Trans. Electron Devices, **ED-17**, 310 (1970).
- G.K. White, *Experimental Techniques in Low-Temperature Physics* (Clarendon Press, Oxford, 1979), p. 307.
- M.J. Wengler, D.P. Woody, R.E. Miller and T.G. Phillips, Intl. J. MM and IR, **6**, in press (1985).
- D.P. Woody, Ph.D. thesis, University of California, Berkeley, 1975.
- Y. Yafet, R.W. Keyes and E.N. Adams, J. Phys. Chem. Solids, **1**, 137 (1956).
- S. Zwerdling, R.A. Smith and J.P. Theriault, Infrared Phys., **8**, 271 (1968).